DISS. ETH NO. 27835

Precessional Dynamics in Magnetic Trilayers and Two Dimensional Structures

A thesis submitted to attain the degree of
DOCTOR OF SCIENCES of ETH ZURICH
(Dr. sc. ETH Zurich)

presented by

Jingyuan Zhou

MSc ETH Physics, ETH Zürich

born February 24, 1993,

citizen of China

Accepted on the recommendation of

Prof. Dr. Laura Heyderman
Prof. Dr. Pietro Gambardella
Prof. Dr. Dirk Grundler

2021

Declaration of Originality

I hereby declare that the following submitted thesis is original work which I alone have authored and which is written in my own words.

Title: Precessional Dynamics in Magnetic Trilayers and Two Dimensional Structures
Author: Zhou, Jingyuan
Supervisor: Prof. Dr. Laura Heyderman

With my signature I declare that I have been informed regarding normal academic citation rules and that I have read and understood the information on “Citation etiquette”. The citation conventions usual to the discipline in question here have been respected.

Furthermore, I declare that I have truthfully documented all methods, data, and operational procedures and not manipulated any data. All persons who have substantially supported me in my work are identified in the acknowledgements.

The above work may be tested electronically for plagiarism.

Zürich, 18 10, 2021

Abstract

Magnonics is an emerging research field in magnetism in which spin waves are used to transmit and process information. Unlike traditional electronics, the propagation of spin waves does not necessarily involve an electric current, and hence no Joule heating is generated, which makes magnonic devices promising candidates for the new generation of low energy dissipation devices. One important aspect in magnonics is to achieve the capability to manipulate the precessional dynamics of the magnetization in different magnetic systems in order to implement controllable functionalities in magnonic devices. In this thesis, we focus on two promising systems based on ferromagnetic thin films, namely the magnetic trilayers and two dimensional structures. By characterizing the precessional dynamics in these systems, we aim at determining the key elements to tune the precessional dynamics.

For the first system, where two ferromagnetic layers are coupled antiferromagnetically to form a magnetic trilayer, we systematically characterized the precessional dynamics with the layer magnetization going from nearly antiparallel to parallel alignment in a magnetic field. Experimentally, the time-resolved precession of the magnetization was measured using an all-optical pump-probe technique based on the magneto-optical Kerr effect. In addition to the acoustic and optical modes, a transient mode was observed that resulted from the laser-induced decoupling of the two ferromagnetic layers. With the help of theoretical calculations, we revealed that the coupled dynamics is determined by the interplay of the Zeeman energy and the interlayer exchange coupling. Accordingly, the precessional dynamics could be divided into three field regions, whose definitions depended on the angle between the two layer magnetizations.

For the second system, based on two dimensional magnetic structures, our aim was to determine the relationship between the precessional dynamics and the symmetry of the different synthetic structures. In particular, we have investigated a crystal structure with translation symmetry and a fractal structure with dilation symmetry. We first characterized the dynamics in the synthetic crystal structure, where groups of horizontally and vertically orientated nanomagnets were coupled magnetostatically to form a so-called trident artificial spin ice. From the measured time-resolved precession, we found that the spin-wave spectra were significantly modified by the applied magnetic field. Moreover, the simulated spatial profile of the spin-wave modes revealed the mode evolution from simple building block structures to complex arrays. In particular, the eigenmodes in the magnetic unit cell exhibited similar spatial distributions as the dominating modes of the complex arrays, which was consistent with the translational symmetry of the crystal. In addition, two extra modes were found whose behaviors depended on the size of the array, and which were related to the collective dynamics of the whole array.

Finally, we characterized the precessional dynamics in a magnetic fractal structure. To ascertain how the fractal geometry influenced the mode formation, the precessional dynamics was measured in samples developing from a simple geometric structure towards a fractal-like structure. The experimentally observed evolution of the precessional motion was found to be related to the different geometric structures via the demagnetizing field. Furthermore, we found that the mode formation in fractals followed the dilation symmetry, i.e., the mode was inclined to form a scaled spatial distribution following the geometric scaling. Based on this, we determined the two necessary conditions for such a mode formation to occur. One condition was that the associated magnetic boundaries must be present, and the other condition was that the mode must not coincide with the regions of the edge modes.

To conclude, in this thesis, we demonstrate that the precessional dynamics in coupled magnetic trilayers and magnetic two dimensional structures is determined by the competition between the associated energies and the unique symmetries related to the geometric structures. In this way, guiding principles for using these magnetic systems to develop functional magnonic devices are provided.

Zusammenfassung

Die Magnonik ist ein aufstrebendes Forschungsgebiet im Bereich des Magnetismus, in dem Spinwellen zur Übertragung und Verarbeitung von Informationen genutzt werden. Im Gegensatz zu traditioneller Elektronik ist die Ausbreitung von Spinwellen nicht notwendigerweise mit Ladungsstrom verbunden, und daher wird keine Joule-Wärme erzeugt, was magnonische Bauelemente zu vielversprechenden Kandidaten für die neue Generation von Geräten mit geringem Energieverlust macht. Ein wichtiger Aspekt in der Magnonik-Forschung ist, die Fähigkeit zu erlangen, die Präzessionsdynamik der Magnetisierung in verschiedenen magnetischen Systemen zu beeinflussen, um steuerbare Funktionalitäten in den magnonischen Bauelementen zu implementieren. In dieser Arbeit konzentrieren wir uns auf zwei vielversprechende magnetische Systeme, die auf ferromagnetischen Dünnschichten basieren, nämlich magnetische Dreifachschichten und magnetische zweidimensionale Strukturen. Durch die Charakterisierung der Präzessionsdynamik in diesen Systemen beabsichtigen wir, die Schlüsselelemente zu bestimmen, um die Präzessionsdynamik einzustellen.

Für das erste System, bei dem zwei ferromagnetische Schichten antiferromagnetisch zu einer magnetischen Dreifachschicht gekoppelt sind, haben wir die Präzessionsdynamik systematisch charakterisiert, wobei die Schichtmagnetisierung in einem Magnetfeld von nahezu antiparalleler zu paralleler Ausrichtung übergeht. Experimentell wurde die zeitaufgelöste Präzession der Magnetisierung mit einer volloptischen Anregungs-Abfrage-Technik gemessen, die auf dem magneto-optischen Kerr-Effekt basiert. Zusätzlich zu den akustischen und optischen Moden wurde eine transiente Mode beobachtet, die ein Ergebnis der laserinduzierten Entkopplung der beiden ferromagnetischen Schichten ist. Mit Hilfe von theoretischen Berechnungen konnten wir zeigen, dass die gekoppelte Dynamik durch die relativen Beiträge der Zeeman-Energie und der mit der Zwischenschicht-Austauschkopplung verbundenen Energie bestimmt wird. Dementsprechend konnte die Präzessionsdynamik in drei Feldregionen unterteilt werden, deren Definitionen vom Winkel zwischen den beiden Schichtmagnetisierungen abhingen.

Für das zweite System, basierend auf magnetischen zweidimensionalen Strukturen, war unser Ziel, die Beziehung zwischen der Präzessionsdynamik und den zugehörigen Symmetrien für die verschiedenen geometrischen Strukturen zu bestimmen. Insbesondere haben wir zwei Strukturen untersucht, und zwar eine Kristallstruktur mit Translationssymmetrie, und eine fraktale Struktur mit Dilatationssymmetrie.

Zunächst haben wir die Dynamik in einer Kristallstruktur charakterisiert, in der Gruppen von horizontal und vertikal orientierten Nanomagneten magnetostatisch gekoppelt wurden, um ein sogenanntes dreizackiges künstliches Spin-Eis zu bilden. Aus der gemessenen zeitaufgelösten Präzession fanden wir heraus, dass das Spinwellen-Spektrum durch das angelegte Magnetfeld signifikant modifiziert wurde. Ausserdem zeigten die simulierten Modenprofile die Modenentwicklung von einfachen Bausteinstrukturen zu komplexen Anordnungen. Insbesondere zeigten die Eigenmoden in der magnetischen Einheitszelle ähnliche räumliche Verteilungen wie die dominierenden Moden für die komplexen Anordnungen, was mit der Translationssymmetrie für eine Kristallgeometrie konsistent war. Darüber hinaus wurden zwei zusätzliche Moden gefunden, deren Verhalten von der Grösse der Anordnung abhing und die mit der kollektiven Dynamik für die gesamte Anordnung in Zusammenhang standen.

Schliesslich haben wir die Präzessionsdynamik in einer magnetischen fraktalen Struktur charakterisiert. Um festzustellen, wie die fraktale Geometrie die Modenbildung beeinflusst, wurde die Präzessionsdynamik in Proben gemessen, die von einer einfachen geometrischen Struktur zu einer fraktalähnlichen Struktur weiterentwickelt wurden. Es wurde festgestellt, dass die experimentell beobachtete Entwicklung der Präzessionsbewegung mit den unterschiedlichen geometrischen Strukturen über das entmagnetisierende Feld zusammenhängt. Weiterhin fanden wir heraus, dass die Modenbildung in Fraktalen der Dilatationssymmetrie folgt, d.h. die Moden neigen dazu, eine skalierte räumliche Verteilung zu bilden, die der geometrischen Skalierung folgt. Darauf aufbauend ermittelten wir zwei notwendige Bedingungen für das Auftreten einer solchen Modenbildung. Eine Bedingung war, dass die zugehörigen magnetischen Grenzen entsprechend skalieren müssen, und die andere Bedingung war, dass die Mode nicht mit den Regionen für die Randmoden zusammenfallen darf.

Um abzuschliessen, in dieser Arbeit zeigen wir, dass die Präzessionsdynamik in gekoppelten magnetischen Dreifachschichten und magnetischen zweidimensionalen Strukturen durch die Konkurrenz zwischen den zugehörigen Energien und den eindeutigen Symmetrien in Bezug auf die geometrischen Strukturen bestimmt wird. Auf diese Weise werden Leitprinzipien für die Verwendung dieser magnetischen Systeme zur Entwicklung funktionaler magnonischer Bauelemente bereitgestellt.

Contents

Abstract i

Zusammenfassung iii

Introduction xvii
- 1. Outline xix
- 2. Contributions xx

1. Background 1
- 1.1. Basics in magnetism 1
  - 1.1.1. Magnetic field and magnetic moment 1
  - 1.1.2. Magnetic interactions and magnetic properties of materials 4
- 1.2. Magnetization dynamics 6
  - 1.2.1. Magnetization dynamics from femtoseconds to microseconds 6
  - 1.2.2. Magnetization precession and damping 8
- 1.3. Magnetostatic spin waves 11
- 1.4. Experimental methods for investigating magnetostatic spin waves 16
  - 1.4.1. Principles of excitation 16
  - 1.4.2. Principles of detection 19
- 1.5. Magnonics 22

2. Experimental 27
- 2.1. Pump-probe experiment 27
- 2.2. All-optical pump-probe experiment with TRMOKE 29
- 2.3. Time-resolved scanning Kerr Microscopy (TRSKM) 33
  - 2.3.1. Setup description 33
  - 2.3.2. Measurement protocol 35
  - 2.3.3. Measurement of dispersion relation 37
- 2.4. Sample fabrication 39

3. Magnetization dynamics in antiferromagnetically coupled ferromagnetic thin films 43
- 3.1. Static magnetic properties of synthetic antiferromagnets 44
- 3.2. Ultrafast laser induced precessional dynamics 47
  - 3.2.1. Experimental data and analysis 47

3.2.2. Theoretical model for precessional dynamics 50
3.2.3. Discussion 52
3.3. TRSKM measurement of synthetic antiferromagnet 58
3.4. Conclusion 59

4. Spin-wave dynamics in artificial spin ice 61
4.1. TRMOKE results 62
4.2. Spin-wave dynamics in single nanomagnet 64
4.3. Evolution of dynamics from building blocks to arrays 65
4.3.1. Spin-wave dynamics in building blocks 66
4.3.2. Spin-wave dynamics in arrays 68
4.4. Conclusion 71

5. Precessional dynamics in ferromagnetic fractal-like structures 73
5.1. Experimental details 75
5.1.1. Sample information 75
5.1.2. TRSKM measurement 77
5.2. Result and discussion 78
5.2.1. Experimental results 78
5.2.2. Precessional dynamics in SQ-2 81
5.2.3. Precessional dynamics in SQ-3 85
5.3. Conclusion 89

6. Conclusions and outlook 91
6.1. Magnetic trilayers 91
6.2. Magnetic 2D structures 92
6.3. Outlook 94
6.3.1. Magnetic trilayers 94
6.3.2. Magnetic 2D structures 95

A. Appendix 97
A.1. Characterization of TRSKM setup 97
A.2. Calculation of precessional dynamics 98
A.3. Supplementary figures for Chapter 5 99

Acknowledgements 103

References 105

Curriculum Vitae 121
Education 121
Publications 121
Conference contributions 122

Teaching experience 122

List of Figures and Tables

1.1. Three types of magnetization dynamics ranging from 1 fs to 1 μs. (a) Ultrafast demagnetization [55], (b) magnetization precession and damping and (c) magnetic domain wall motion. 6

1.2. Schematic of magnetization precession and damping. The directions of the two torques are indicated with the arrows with different colors. 8

1.3. (a)-(c) Static magnetization configuration and wavevector orientation for the three magnetostatic spin-wave modes. (a) and (b) share the same coordinates, and (c) is in another coordinate system. (d) Scaled spin-wave dispersion relation for the three magnetostatic spin-wave modes with $\omega_0/\omega_{\mathrm{M}} = 0.5$ corresponding to (a)-(c). The two volume modes are the lowest-order modes. 13

1.4. Frequency relation of exchange, dipole-exchange, and magnetostatic spin waves as a function of wavelength for a 5 nm yttrium-iron garnets (YIG), while neglecting anisotropy and assuming that the wavevector is parallel to the equilibrium magnetization direction. [81] 16

1.5. (a) and (c) Schematics of the microstrip and coplanar waveguide. (b) Schematic of the magnetic distribution for a cross section of the microstrip. 17

1.6. Three time stages for the laser-induced precession [84]. $\hat{e}$ points along the equilibrium axis of the magnetization, and $\hat{e}'$ points towards the transient equilibrium position at time stage II. 18

1.7. Three MOKE geometries. The dashed plane is plane of incidence. . 19

1.8. (a) Block diagram of the four components for a magnonic device. (b)-(c) Three common methods for manipulating the functional medium. 23

2.1. Diagram of the building blocks of a pump-probe setup. The abbreviations are RF: radio frequency, BLS: Brillouin light scattering and VNA: vector network analyzer. 28

2.2. All-optical pump-probe setup with TRMOKE. A: attenuator, BS: beamsplitter, F: optical filter, G: glass plate, L: optical lens, M: mirror, MO: microscope objective. 29

2.3. Schematic of the working principle of the optical bridge detector. . 30

2.4. Precessional dynamics of a CoFeB film measured from the all-optical setup with TRMOKE. (a) Normalized time-resolved Kerr rotation. (b) Normalized FFT power spectrum. (c) Raw data at 114 mT, with the red line indicating the decay background. 32
2.5. Schematic of the TRSKM setup. (a) Diagram of the signal connections between different components. The black boxes denote the optical devices, electrical devices and the sample. The blue boxes denote the optical or electric signals. The synchronization module is marked with the orange dashed box, with an inset demonstrating the synchronization between the RF (the sinusoidal wave) and laser (red lines) signals. The red dashed lines indicate the new phase that the signal is locked to, when the original signal (red solid lines) is delayed. (b) Schematics of the setup at the sample with a magnetic film under the signal transmission line. 34
2.6. TRSKM measurement protocol and typical data. (a) Flowchart of the steps to perform a TRSKM measurement. Here, SS stands for sample stage, ODS for optical delay stage and Y/N for Yes/No. (b) Time-resolved Kerr rotation with the RF excitation of a CoFeB film at 5.25 GHz. (c) Image of the propagating spin wave on both sides of the transmission line, at f_{RF} = 4.50 GHz. The transmission line (white bar) is along the Y direction, located at X = 10.157 mm, and the external bias field is applied along the Y direction. (d) Line profile of the scanned Kerr rotations in (c) at Y = 1.360 mm. 36
2.7. Characterization of the dispersion relation of the spin waves in a 10 nm-thick CoFeB film. (a) Scanning Kerr rotation measurements along the X direction for f_{RF} ranging from 4.5 to 6.5 GHz. The lines are shifted for clarity. (b) FFT power of the line scanning measurement at 5.75 GHz. (c) Dispersion relation of the measured Damon-Eshbach mode. 38
2.8. Electron beam lithography and fabrication steps of a CoFeB film sample for TRSKM measurement. (a) The schematics of the sample is shown on the right side. The blue part is the CoFeB film, the yellow part is the microstrip, and the closed box is the alignment marker array, with a zoom in of the top left markers. (b) Work flow of a typical e-beam lithography process. Color blue: substrate, red: resist layer, and black: deposited materials. 40
2.9. Composition of the three components of the CoFeB film sample for TRSKM measurement 41

3.1. (a) Layer thicknesses for the four samples, where t_1, t_2 and t_{Ru} are the thickness of the upper magnetic layer, the lower magnetic layer next to the Si(100) substrate and the Ruthenium layer, respectively. (b) The IEC strength J as a function of the Ru thickness. (c) In-plane hysteresis loops for Sample 1 and 4 in a magnetic field range of -75 to +75 mT, and (d) Sample 2 and 3 in a magnetic field range of -1.5 to +1.5 T. 45

3.2. (a) Schematic of the magnetization configuration of the trilayer film and the coordinate system. (b) Magnetization orientation in the two layers, θ_1 and θ_2, of Sample 2 as a function of the applied magnetic field. 46

3.3. Normalized time-resolved (a) reflectivity and (b) Kerr rotation data of Sample 2 measured at a magnetic field of 150 mT. Lines are guided for the eyes. (c) Background subtracted data from (b) after 100 ps. Data is fitted with a two-component damped sine wave function. (d) FFT Power of (c), with the two modes indicated by the two red markers. 48

3.4. Frequency dependence on the applied magnetic field for the different modes. The different precessional modes are indicated with Roman numbers. 49

3.5. Evolution of the precessional modes in Sample 2 with increasing the fluence of the pump laser beam. Time-resolved Kerr rotation and the corresponding frequency spectrum are shown in the left and right column respectively for Sample 2 at $\mu_0 H = 130$ mT. Lines connecting the data points are guides to the eye. Dashed black lines are positioned at the three observed modes. 49

3.6. Flowchart for determining the precessional dynamics in synthetic antiferromagnets. 51

3.7. Dependence of the frequency on the applied magnetic field for the different modes. (a)-(c) Experimental data: The different precessional modes are indicated with Roman numbers. (d)-(f) Theoretical data: f_{a}, f_{o} and f_{K} are the frequencies of the acoustic mode, optical mode, and the FMR mode for a 7.5 nm CoFeB film. The three different background colors indicate the three field regions given in the inset of (d). 53

3.8. Evolution of the transient mode (mode II) with increasing fluence of the pump laser beam. Time-resolved Kerr rotation and the corresponding frequency spectra are shown in the left and right column respectively for Sample 3 at $\mu_0 H = 270$ mT. Lines connecting the data points are guides to the eye. 55

3.9. Frequency relationship of the different modes for symmetric and asymmetric samples 57

3.10. (a) Magnetic hysteresis loop of the sample CoFeB(5 nm)/Ru(0.4 nm)/CoFeB(10 nm). (b) Time-resolved Kerr rotations measured from the all-optical pump-probe experiment. (c) Scanning Kerr rotations along the X direction across the microstrip, with f_{RF} ranging from 3.4 to 4.75 GHz, and lines shifted for clarity. The positions correspond to the 1 μm microstrip are indicated by the shaded area. The magnetic field configuration and sample geometry are shown in the right schematic. 58

4.1. SEM image of the Py trident spin ice, with the orientation of the in-plane component of the applied magnetic field. 62
4.2. (a) Time-resolved Kerr rotation measured at the three applied magnetic fields of 100, 50 and 30 mT. (b) Frequency spectra of (a). (c) Simulated frequency spectra considering a limited excitation region [see Fig. 4.1], with a 1.5 ns relaxation time. 63
4.3. (a) Simulated frequency spectrum for a single nanomaget on applying a magnetic field of 100 mT along the direction indicated by the blue arrow. (b) Amplitude distributions of the four modes labeled in (a). 65
4.4. (a) Simulated spin-wave spectra of the three magnet structure, 2 × 1 structure and 2 × 2 structure with applying an external magnetic field of 100 mT along the direction indicated by the blue arrow. The spatial distributions of the labeled modes are plotted in (b), (c) and (d) for different building block geometries. The modes are marked on the spectra and in images in (b)-(d) with corresponding colored circles, squares and triangles. 66
4.5. Simulated demagnetization fields for (a) three horizontal and vertical magnet structures, (b) the 2 × 1 structure and (c) the 2 × 2 structure. The demagnetization field is plotted along the arrow directions indicated in (a). 69
4.6. (a) Simulated spin-wave spectra for the 4 different array sizes, with a zoomed view in (b) of the part indicated by the box. (c)-(d) Spatial distributions of the two modes at 10.88 GHz and 11.04 GHz in 3 × 3 and 4 × 4 arrays. 70

5.1. (a) SEM images of square samples SQ-0 to SQ-3, and triangular samples TRI-0 to TRI-3. (b)-(e) In-plane magnetic hysteresis loops of square and triangular samples, with the magnetic field direction shown in (a). 76

5.2. (a) Schematic of the experimental TRSKM setup at the sample. (b)-(c) TRSKM measurements of the sample TRI-0 at $B = 15$ mT and $f_{\mathrm{RF}} = 3.7$ GHz. (b) Normalized time-resolved Kerr rotation measured by a de-focused laser beam (beam size indicated by the red circle). (c) Five normalized scanning Kerr rotation images, in the range [-1,1], measured from t_1 to t_5 at 360, 465, 570, 675 and 780 ps, respectively, which are indicated by the solid lines in (b). 77

5.3. TRSKM measurements of triangular samples. (a) Frequency spectra of the triangular samples TRI-0 to TRI-2. (b) SEM images of samples TRI-0 to TRI-2, with the magnetic field direction indicated next to TRI-2. (c) Normalized scanning Kerr images at the 3.7 GHz mode for the three samples. The 3.7 GHz mode is indicated by red markers in (a). 79

5.4. TRSKM measurements of square samples. (a) Frequency spectra of square samples SQ-0 to SQ-2. (b) SEM images of samples SQ-0 to SQ-2, with the magnetic field direction shown besides SQ-2. (c) Normalized scanning Kerr images of the different modes for the three samples. The modes corresponding to different frequencies are indicated by different colored markers in (a). (d) Schematic of the different defined structures in SQ-2. L1-L4 are the four edges with width of 9 μm, s1 is the central 3 $\mu m \times 3$ μm empty square, and s2 corresponds to the eight 1 $\mu m \times 1$ μm empty squares. 80

5.5. Comparison between the (c) experimental scanning Kerr images and (b) simulated m_z distribution with single frequency excitation. The simulated m_z distributions are taken at the time indicated by the red dashed lines in (a). The colormaps in (b) are set to optimize the image contrast for the spatial distribution. 81

5.6. Simulated precessional dynamics of SQ-2. (a) Frequency spectrum of SQ-2 at 15 mT. The shaded areas with different colors indicate the three types of modes, edge mode (E), first order local mode (M) and higher order mode (HO). (b) Mode profiles of the six modes indicated by the dashed lines in (a). For the amplitude distribution, each colormap is set to optimize the image contrast. 83

5.7. (a) Amplitude distribution of the three bulk-like modes M1 to M3 of SQ-2. The colormap is adapted to show the best contrast. (b) Total field distribution B_{tot} inside the magnetic structure of SQ-2. (d) Five line profiles of the total field distribution along the horizontal direction, with positions indicated by dashed lines in (c). 84

5.8. Mode evolution from SQ-1 to SQ-3. (a) Amplitude distributions of the two modes at 3.10 and 4.00 GHz for SQ-1. (b) Amplitude distributions of the three modes M1 to M3 for SQ-2. (c) Amplitude distributions of the three modes for SQ-3 at 4.30 GHz (M1′), 7.55 GHz (M3′) and 6.04 GHz. The white boxes mark the regions where the edge modes occur. (d) Schematic of SQ-3, with different color shaded areas indicating the eight scaled SQ-2 structures $\mathrm{SQ}-2(j)$, $j = 1 - 8$. 86

A.1. Synchronization verification using two signals from the laser and RF current. 97
A.2. Characterization of the laser spot size. 98
A.3. TRSKM measurements of samples SQ-3 and TRI-3. (a) Frequency spectra of samples SQ-3 and TRI-3. (b) SEM images of the two samples. (c) Normalized scanning Kerr images of the different modes for the two samples. The modes are indicated by the red markers in (a). 100
A.4. Simulated (a) frequency spectrum, (b) amplitude distribution and (c) phase distribution of the main mode in TRI-2, which is indicated by the dashed line in (a). 100
A.5. Simulated (a) frequency spectrum, (b) amplitude distribution and (c) Phase distribution of the five modes in SQ-3, which are indicated by the dashed lines in (a). 101

List of Abbreviations

	Explanation
RKKY interaction	Ruderman–Kittel–Kasuya–Yosida interaction
MOKE	Magneto-optical Kerr effect
TRMOKE	Time-resolved magneto-optical Kerr effect
TRSKM	Time-resolved scanning Kerr microscope/ microscopy
LLG equation	Landau-Lifshitz-Gilbert equation
FMR	Ferromagnetic resonance
α	Gilbert damping
M_S	saturation magnetization
RF	Radio frequency
CPW	Coplanar waveguide
BLS	Brillouin light scattering
VNA	Vector network analyzer
FFT	Fast Fourier transformation
SAF	Synthetic antiferromagnet
IEC	Interlayer exchange coupling
FM	ferromagnetic
NM	Non magnetic

Introduction

We all might have observed that slowly swinging a permanent magnet close to a magnetic compass causes the compass needle to follow the movement of the magnet and rotate back and forth. Such a rotational motion of the compass needle occurs because it is experiencing a torque originating from the magnetic field provided by the magnet. This simple system offers a macroscopic and intuitive example of a dynamic magnetic effect, but magnetic systems can exhibit a broad range of dynamical phenomena, many of which cannot be perceived by the human eye. Interestingly, as the length scale at which these dynamic magnetic phenomena occur is decreased from the macroscopic to the mesoscopic scale, the phenomena become more and more complex. When further decreased to the microscopic scale, one eventually needs to use quantum mechanics to describe the resultant phenomena.

At the macroscopic scale, the magnetic object is often modeled as an effective dipole moment. Once the magnetic moment is not aligned with the applied magnetic field, rotational motion will start, and this motion can be well described using the framework of classical mechanics. The physical descriptions of such a macroscopic motion has led to many technological applications of magnetic systems. A famous example is the magnetic microrobot, where a designated and controllable motion of the microrobot can be achieved by tailoring both the magnetic system and the applied magnetic field [1–3]. Moving to a mesoscopic length scale, when describing the magnetic system, it is convenient to use another physical quantity, the magnetization. In this case, the magnetization dynamics is often described by the Landau-Lifshitz-Gilbert equation (LLG) [4]. At this length scale, the complexity of the magnetization dynamics is increased, due to the increased number of magnetic configurations and associated magnetic interactions [5, 6]. As a result, many interesting dynamical phenomena occur, such as magnetization precession and damping [7], propagating spin waves [8, 9], magnetic domain wall motion [10, 11] and magnetization switching [12–14], all of which have led to significant progress in the fields of magnonics and spintronics, as well as many promising technological applications [15–18]. As mentioned above, when moving to the microscopic length scale, one needs to switch to a quantum mechanical description of the system. Accordingly, the concept of magnetization is replaced by the spin operators, which operate on the wave functions of the corresponding systems. At the microscopic length scale, the spin moment mainly exhibits a Larmor precession, which is the physical principle of both nuclear magnetic resonance (NMR) [19] and electron paramagentic resonance [20]. NMR has now been further developed into magnetic resonance imaging (MRI), which is widely used in the medical industry [21].

In this thesis, we focus on the magnetization precession in thin films on the mesoscopic level. Such a precessional motion of the magnetization, when it propagates, is commonly referred to as spin waves or magnons. Spin waves are promising candidates for the low-energy transmission and processing of information [22], and the great potential of spin waves has made magnonics a lively research field. In addition, magnonics has many advantages when compared with other fields. Unlike electronics, the propagation of spin waves does not involve the movement of electrical charges, and hence can exclude the generation of Joule heating, which is the main source of inefficiency for semiconductor-based electronics [23, 24]. Furthermore, magnonic devices are based on magnetic materials, which gives them the intrinsic property of being able to store non-volatile information. Currently, the spin waves used for magnonics are often operated in the gigahertz range, which lies in the microwave frequency band [25]. The wavelengths of the spin waves are several orders of magnitude smaller than the microwaves with the same frequency, which makes magnonic devices more promising for device miniaturization. Moreover, when compared with other new research fields, such as photonics [26] and phononics [27], magnonics offers an additional tuning parameter via the application of a magnetic field.

One important research aspect in magnonics is to determine how to effectively tune the magnetic interactions in order to achieve a variety of functionalities. For example, in magnonic crystals where the magnetic structures are periodically arranged, the magnetostatic interactions are effectively tuned by varying the relevant geometric parameters, which can modify the functionality of filtering of spin waves [28]. With this in mind, we focus on tuning the magnetic interactions in ferromagnetic thin films. To allow for more degrees of freedom, we focus not only on the two dimensional (2D) plane of the thin film, but also extend our investigation to its interfaces. More specifically, we deposit magnetic trilayers to introduce the Ruderman–Kittel–Kasuya–Yosida (RKKY) interaction as an interlayer coupling, which can couple the ferromagnetic layers antiferromagnetically or ferromagnetically [29–31]. Such interlayer coupling results in a coupled precessional motion of the two layer magnetizations that contains the acoustic and optical modes [32]. In addition, the antiparallel coupling has been proposed to give a nonreciprocal spin-wave dispersion in the Damon-Eshbach geometry [33–35], which could be used to build nonreciprocal magnonic devices. The tunability of such coupled precession is achieved by changing the thickness of the nonmagnetic layer between the two ferromagnetic layers [30, 31]. For this research, our aim is to find how the precessional dynamics is modified by the interlayer coupling. In addition to magnetic trilayers, we tune the magnetic interactions by patterning 2D ferromagnetic structures starting from the thin films. For this purpose, we choose two different approaches. For the first approach, we follow the design of artificial spin ices and investigate the spin-wave dynamics in nanomagnet arrays with a 'trident' lattice geometry [36]. In this case, the magnetization dynamics is dominated by the eigenmodes in each nanomagnet, and the collective dynamics for the whole array is mediated by the magnetostatic interactions between the nanomagnets. For the second approach, we investigate the precessional dynamics in ferromagnetic fractal-like structures [37, 38]. In this case, the magnetization dynamics is modified by the different geometric structures via the demagnetizing field. For both approaches, our general aim is to find the relation between the precessional dynamics and system geometry, and hence provide methods of using different geometric designs to effectively tune the magnetization dynamics.

1. Outline

In each chapter of this thesis, a more detailed overview of the related physical concepts and research works are given. In addition, for each specific work presented in this thesis, the related experimental techniques, theory and numerical simulations are introduced. The content of this thesis is as follows:

In Chapter 1, the basics about magnetism and magnetization dynamics are introduced, which facilitates a general understanding for the whole thesis. Next, we present the basic properties of magnetostatic spin waves, their generation and detection methods, and their potential applications in terms of magnonic devices. Our goal here is to give the reader a systematic overview of spin waves and their related applications.

In Chapter 2, we introduce the experimental techniques used for the research described in this thesis. The first part is about the so-called pump-probe experiments, which facilitate a direct observation of the precessional motion of the sample magnetization. Here, we introduce the two experimental setups developed in house. One is an all-optical pump-probe setup with time-resolved magneto-optical Kerr effect (TRMOKE), and the other is a time-resolved scanning Kerr microscope (TRSKM). Using these setups, different characterizations of spin waves can be performed. The second part of this chapter is about sample fabrication, where the lithography processes for fabricating different samples are introduced.

In Chapter 3, we report on the magnetic trilayer films in which two ferromagnetic layers are coupled antiferromagnetically and are experimentally investigated using both the all-optical pump-probe setup with TRMOKE and TRSKM. The observed precessional dynamics measured by the all-optical setup is a coupled precession, and both the acoustic and optical modes are observed. In addition, we observe a transient mode, whose occurrence depends on the intensity of the excitation. To describe all these different modes, we have solved the coupled LLG equations. We find that the frequency dependence of each mode on the applied magnetic field can be explained by considering the relative contributions of the Zeeman energy and the energy associated with the interlayer exchange coupling. Finally, the observed precessional dynamics obtained by TRSKM does not show a propagating nature, and we provide several possible explanations for this.

In Chapter 4, we investigate nanomagnet arrays forming a trident spin ice using both the all-optical setup and micromagnetic simulations. Experimentally, by measuring the time-resolved precession, we find that an external field can significantly modify the spin-wave spectra. Following this, micromagnetic simulations are performed to reveal the spatial distribution of the modes. Based on the simulated results, we examine the evolution of spin-wave dynamics from three types of building blocks to large arrays. We find that the eigenmodes present in the building blocks are important for the dynamics of large arrays. In addition, we find two extra modes whose behaviors depend on the array size, which are related to a collective behavior of the whole array.

In Chapter 5, we describe the investigation of ferromagnetic fractal-like structures using both the TRSKM and micromagnetic simulations. By determining the mode evolution from a simple geometric structure to a complex fractal-like structure, we find a general trend of the mode formation related to the geometric scaling defined in these fractal structures. A detailed analysis of the mode profiles in the sample reveals how the mode formation is related to the different geometric structures via the demagnetizing field. Furthermore, we show how the scaling relation determines the relationship between the amplitude distributions of certain modes in the fractal samples, with additional modifications introduced by structures at different length scales.

In Chapter 6, a summary of the conclusions of this thesis and an outlook are provided.

2. Contributions

Since the works presented in this thesis were performed as part of a research team, for clarity, an overview of the contributions of the PhD student, Jingyuan Zhou, are described here for each chapter, along with collaborations and supervision.

Chapter 2

- Optimized the measurement parameters for the all-optical setup.
- Designed and built the TRSKM setup, with supervision from Susmita Saha and Valerio Scagnoli, and technical help from Alexander Dietrich, Sergii

Parchenko, Simone Finizio, and Jörg Raabe.

- Developed the sample fabrication process in collaboration with Zhaochu Luo, and measurement protocols for the TRSKM measurement.

Chapter 3

- Fabricated the samples in collaboration with Eugenie Kirk and Zhaochu Luo.
- Performed the all-optical pump-probe measurements and analyzed the data with supervision from Susmita Saha and Valerio Scagnoli.
- Performed the theoretical calculations with supervision from Peter Derlet, and interpreted the results.
- Wrote the manuscript with contributions from all authors.
- Performed the TRSKM measurements and analyzed the data.

Chapter 4

- Kevin Hofhuis fabricated the samples.
- Susmita Saha and Jingyuan Zhou performed the all-optical pump-probe measurements and analyzed the data.
- Attila Kákay, Sebastian Gliga and Susmita Saha performed the micromagnetic simulations.
- Susmita Saha and Sebastian Gliga interpreted the data, and wrote the manuscript with contribution from all authors.

Chapter 5

- Fabricated the samples in collaboration with Zhaochu Luo.
- Performed the TRSKM measurements and analyzed the data.
- Mateusz Zelent performed the micromagnetic simulations.
- Analyzed and interpreted the simulation results in collaboration with Susmita Saha.
- Wrote the manuscript with contributions from all authors.

1. Background

In this chapter, we introduce basic concepts that will guide the reader in the understanding of the results presented in this thesis. In Sec. 1.1, the basic concepts in magnetism and several relevant magnetic interaction mechanisms are introduced. In Sec. 1.2, different types of magnetization dynamics that occur from femtosecond to microsecond are introduced, with an emphasis on the formalism for describing the magnetization precession. In Sec. 1.3, a commonly used method for calculating the magnetostatic spin waves is introduced, followed with explanations of the basic properties of magnetostatic spin waves. In Sec. 1.4, the different physics principles behind exciting and detecting spin waves are introduced. Finally, in Sec. 1.5, potential applications for spin waves are discussed, with an emphasis on describing the analog and digital magnonic devices.

1.1. Basics in magnetism

1.1.1. Magnetic field and magnetic moment

One of the most common and ancient applications of magnetism is the magnetic compass. It aligns with the geographic north pole of the earth and, since its discovery, it has made significant contributions to human history because of its navigation function. The physics principle behind its function is that both the compass needle and the earth are magnetic, and can be treated as two magnetic poles. Different magnetic poles attract each other while the same poles repel themselves. This phenomenon, for a long time, has been the only understanding that people perceived for magnetism. Once the concept of the magnetic field was introduced, the research into magnetism has officially started.

Today, people have realized that the magnetic field is strongly related to the electric field, and are together often referred to as electromagnetic field. The governing equations for electromagnetism are the Maxwell's equations [39],

$$\nabla \cdot \mathbf{D} = \rho, \tag{1.1a}$$

$$\nabla \cdot \mathbf{B} = 0, \tag{1.1b}$$

$$\nabla \times \mathbf{E} = -\frac{\partial \mathbf{B}}{\partial t}, \tag{1.1c}$$

$$\nabla \times \mathbf{H} = \mathbf{J} + \frac{\partial \mathbf{D}}{\partial t}. \tag{1.1d}$$

In this thesis, all the physics quantities are in SI units. The quantities in Maxwell's equations are:

- **D**: electric displacement field (C/m^2);
- ρ: electric volume charge density (C/m^3);
- **B**: magnetic flux density (T);
- **E**: electric field (V/m);
- **H**: magnetic field strength (A/m);
- **J**: electric volume current density (A/m^2).

To describe the 'magnetic field', two field quantities are introduced, one is the magnetic flux density **B**, and the other is the magnetic field strength **H**. For convenience, they are often referred as the **B**-field and **H**-field. Eqs. (1.1b) and (1.1d) describe the two properties of the 'magnetic field'. Eq. (1.1b) indicates that the divergence of the **B**-field is always zero, meaning that the field lines of the **B**-field always form closed loops. From Eq. (1.1c), we can infer that there are two sources for the **H**-field. One is the the electric current **J**, and the other one is the time-varying **D**-field. Apart from these properties, the two magnetic and electric field quantities are also related, whose relationship are referred to as the constitutive relations,

$$\mathbf{D} = \varepsilon_0 \mathbf{E} + \mathbf{P}, \tag{1.2a}$$

$$\mathbf{B} = \mu_0(\mathbf{H} + \mathbf{M}). \tag{1.2b}$$

Here the four newly introduced quantities are:

- $\varepsilon_0 \approx 8.854 \times 10^{-12}$ F/m: vacuum permittivity;
- **P**: electric polarization (C/m^2);
- $\mu_0 = 4\pi \times 10^{-7}$ H/m: vacuum permeability;
- **M**: magnetization (A/m).

In Eq. (1.2b), another important quantity in magnetism **M** is introduced, which is defined as the magnetic moment **m** per unit volume. For a given material, **P** and **M** depend on both the applied electric, and magnetic field and the material itself. If the response of **P** and **M** is linear with respect to the applied fields, it can be written as,

$$\mathbf{P} = \varepsilon_0 \bar{\chi}_\mathrm{e} \cdot \mathbf{E}, \tag{1.3a}$$

$$\mathbf{M} = \bar{\chi}_\mathrm{m} \cdot \mathbf{H}. \tag{1.3b}$$

Here $\bar{\chi}_\mathrm{e}$ and $\bar{\chi}_\mathrm{m}$ are the electric and magnetic susceptibility tensors. These linear responses can again be used to rewrite the constitutive equations as,

$$\mathbf{D} = \varepsilon_0(\bar{\mathbf{I}} + \bar{\chi}_\mathrm{e}) \cdot \mathbf{E} = \bar{\varepsilon} \cdot \mathbf{E}, \tag{1.4a}$$

$$\mathbf{B} = \mu_0(\bar{\mathbf{I}} + \bar{\chi}_\mathrm{m}) \cdot \mathbf{H} = \bar{\mu} \cdot \mathbf{H}, \tag{1.4b}$$

where $\bar{\varepsilon}$ and $\bar{\mu}$ are commonly referred as the permittivity and permeability tensors for a material, respectively. For magnetism, the two relations, M versus H and B versus H, are often used to characterize the magnetic properties of a material. In this case, a magnetic hysteresis loop is often obtained by measuring either B or M as a function of the H-field.

Until now, the Maxwell's equations and the constitutive relations give an excellent description of both the electric and magnetic fields, as well as their relations. However, the origin of the magnetization is not explained. The magnetization **M** is just a phenomenological concept introduced in the constitutive relations, which is used to characterize the density of the magnetic moment for a given material. To further understand **M**, two aspects need to be discussed. The first is the origin of a magnetic moment and the second is the interactions between magnetic moments.

Classically, a current loop can be used to model a magnetic moment, which is effectively a magnetic dipole moment [40]. However, to explain the magnetic moment properly, concepts from quantum mechanics need to be introduced. Microscopically, the magnetic moment $\boldsymbol{\mu}$ of an atom mainly comes from the total angular momentum **J** of its electrons. **J** has two contributions. One is the orbital angular momentum **L**, and the other is the spin angular momentum **S**. The relations between these momenta are,

$$\mathbf{J} = \mathbf{L} + \mathbf{S}, \tag{1.5a}$$

$$\boldsymbol{\mu} = \gamma \mathbf{J} = g \frac{-e}{2m_e} \mathbf{J}. \tag{1.5b}$$

Here, γ is the gyromagnetic ratio, g is the Landé g-factor, e is the elementary charge and m_e is the electron mass. The g-factor is approximately 1 for **L** and 2 for **S**. Therefore, $\boldsymbol{\mu}$ and **J** are not exactly collinear, and Eq. (1.5b) is just an approximation. Additionally, since the electron is negatively charged, its magnetic moment and total angular moment are indeed antiparallel. For convenience, the atomic magnetic moment is often described in terms of the Bohr magneton,

$$\mu_\mathrm{B} = \frac{e\hbar}{2m_e}. \tag{1.6}$$

Here, $\hbar$ is the reduced Planck constant. For example, for an electron, the spin angular momentum is $\hbar/2$ and the magnetic moment associated with its spin angular momentum is then approximately $1\mu_\mathrm{B}$.

1.1.2. Magnetic interactions and magnetic properties of materials

Magnetic interactions, namely how a magnetic moment interacts with a magnetic field or another magnetic moment, emerge for different reasons. In the framework of this thesis, we will introduce the Zeeman, exchange and magnetic dipole-dipole interactions. The Hamiltonians that quantify their associated energies are,

$$\mathcal{H}_\mathrm{Z} = -\mathbf{m} \cdot \mathbf{B}, \tag{1.7a}$$
$$\mathcal{H}_\mathrm{ex}^\mathrm{S} = -\mathbf{J}_{ij} \left(\mathbf{S}_i \cdot \mathbf{S}_j\right), \tag{1.7b}$$
$$\mathcal{H}_\mathrm{ex}^\mathrm{AS} = \mathcal{H}_\mathrm{DMI} = -\mathbf{D}_{ij} \cdot \left(\mathbf{S}_i \times \mathbf{S}_j\right), \tag{1.7c}$$
$$\mathcal{H}_\mathrm{dip} = -\frac{\mu_0}{4\pi r^3}[3(\mathbf{m}_1 \cdot \mathbf{r})(\mathbf{m}_2 \cdot \mathbf{r}) - \mathbf{m}_1 \cdot \mathbf{m}_2]. \tag{1.7d}$$

The Hamiltonian for the Zeeman energy $\mathcal{H}_\mathrm{Z}$ describes the interaction between the magnetic moment and magnetic field, which favors a parallel alignment between $\mathbf{m}$ and $\mathbf{B}$. Here, $\mathbf{m}$ could be either a microscopic magnetic moment of an atom, or a macroscopic effective dipole moment of a ferromagnetic object. As for the exchange interaction, it is of a quantum mechanical origin, i.e., the exchange operation between the indistinguishable particles that occurs at the atomic length scale [41]. The exchange interaction, according to its mathematical form, can be classified into two categories. One is the symmetric exchange $\mathcal{H}_\mathrm{ex}^\mathrm{S}$, which is commonly referred as the exchange interaction. It favors a collinear alignment between the two spin moments. The symmetric exchange $\mathbf{J}_{ij}$ can have many origins, such as the direct exchange, superexchange [42, 43] and Ruderman–Kittel–Kasuya–Yosida (RKKY) interaction [44–46]. All these exchange interactions can be effectively modeled by Eq. (1.7b), however for each case, $\mathbf{S}_{i,j}$ are referred to different spin moments. For direct exchange interaction, $\mathbf{S}_{i,j}$ are defined as the total spin moment of the two neighboring atoms. For super exchange interaction, $\mathbf{S}_{i,j}$ are usually defined as the total spin moments of the two next-nearest neighbor magnetic atoms. For RKKY interaction, $\mathbf{S}_{i,j}$ are referred to the two spin moments that interact via the conduction electrons. The specific meanings of $\mathbf{S}_{i,j}$ should be adapted to each case considered. The other is the asymmetric exchange $\mathcal{H}_\mathrm{ex}^\mathrm{AS}$, which is commonly referred as the Dzyaloshinskii–Moriya interaction (DMI) that favors a non-collinear spin texture [47, 48]. The occurrence of the DMI requires two conditions, which are the inversion symmetry breaking and the spin-orbit coupling. The magnetic dipole-dipole interaction $\mathcal{H}_\mathrm{dip}$, commonly referred to as the dipolar interaction, describes the energy between the two magnetic dipoles via the magnetic dipole field.

It depends on the orientation and distance between the two dipole moments. The main differences of these interactions are the length scales at which they occur. Both the Zeeman and dipolar interactions can occur at both long-range and short-range length scales. On the other hand, the exchange interactions are short-range, since they are related to the exchange operation in quantum mechanics.

Having introduced these magnetic interactions, many magnetic properties and magnetic configurations can now be explained, which are the direct result of the energy minimization of the Hamiltonian associated with the relevant magnetic interactions. The Zeeman interaction is often associated with applying an external magnetic field. For a magnetic system, if only the Zeeman interaction is present, it will exhibit a paramagnetic response. The properties of magnetic materials in the absence of externally applied field mainly involve the exchange and dipolar interactions. In general, the exchange interaction can be the dominating term in the system's Hamiltonian, and is responsible for short-range magnetic effects at the atomic length scale. For example, it is due to the intra-atomic exchange interaction that an atom made of several electrons can develop a non-zero total magnetic moment. The inter-atomic exchange and superexchange interaction, depending on the sign of the exchange constant, can determine the type of magnetism in some materials, i.e. whether the magnetic material is ferromagnetic or antiferromagnetic. The DMI is usually the driving force for the presence of many non-collinear spin textures on the small length scale, such as spin spirals [49, 50] and magnetic skyrmions [51].

The dipolar interaction, on the atomic level, is negligible compared with the exchange interaction. However, since it is long-range in nature, the contribution from all the dipoles becomes important at larger length scales, and hence affects the magnetic properties. For example, the dipolar interaction is responsible for the magnetic shape anisotropy of a ferromagnetic object, and the dipolar field related with this effect is often referred as the demagnetization field. For a uniformly magnetized thin film, if only the demagnetization field is considered, the minimum energy is achieved by an in-plane magnetized configuration. There are also other interactions that result in different types of anisotropies, such as the magnetocrystalline anisotropy that is due to the spin-orbit coupling [52, 53].

For a magnetic system, the final magnetic configuration often arises from a competition between all such interactions. For example, for a ferromagnetic film, it often forms magnetic domains that are separated by domain walls [54]. The formation of magnetic domains is in a general a competition between the dipolar interaction, exchange interaction and magnetocrystalline anisotropy.

1.2. Magnetization dynamics

1.2.1. Magnetization dynamics from femtoseconds to microseconds

Having introduced the static magnetic properties in the context of different magnetic interactions, we now explain the dynamic part for the magnetic system. Magnetization dynamics describes the time evolution of the magnetization of a magnetic material, which involves different time scales. An overview of the different time scales of the magnetization dynamics for a ferromagnetic material is shown in Fig. 1.1. Here, three types of dynamics are introduced. The first one is the ultrafast demagnetization that is induced by a femtosecond laser pulse, whose characteristic time scale is below 1 ps. The second one is the magnetization precession and damping, which ranges between tens of picoseconds up to several nanoseconds. The third one is the domain wall motion, which is typically on the time scale of microseconds.

Among the different dynamical processes, the fastest is the phenomenon of ultrafast demagnetization [see Fig. 1.1(a)], which was first observed in ferromagnetic Nickel by E. Beaurepaire et al. in 1996 using MOKE [55]. It was reported that 'the magnetization of the film drops rapidly during the first picosecond'. This was also later confirmed to be around 100-300 fs using other experimental techniques such as spin-resolved photoemission and X-ray magnetic circular dichroism [56–58]. Following these measurements, different mechanisms have been proposed to explain this ultrafast phenomena. Firstly, a three temperature model was introduced to describe the interactions between the electron orbitals, spin and lattice [55]. This

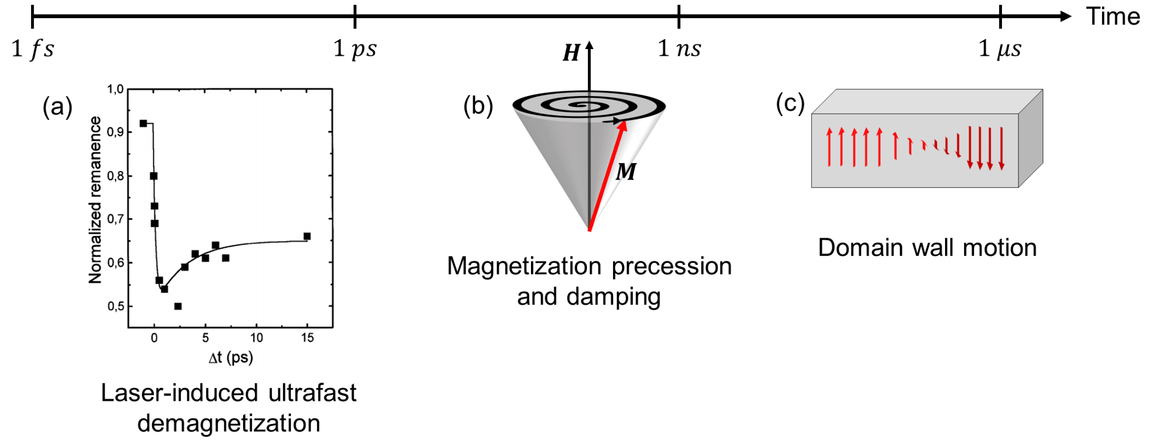

Laser-induced ultrafast demagnetization

Magnetization precession and damping

Domain wall motion

Figure 1.1. Three types of magnetization dynamics ranging from 1 fs to 1 μs. (a) Ultrafast demagnetization [55], (b) magnetization precession and damping and (c) magnetic domain wall motion.

model successfully described the energy transfer between the three sub-systems with some interaction constants, and hence enabled a phenomenological description of the experimental results. However, this model only covered the energy transfer between the sub-systems. To give a more complete description, the transfer of the angular momentum needs to be introduced. To allow this, the electron orbital moment was first considered, where both the spin-orbit coupling and the laser field are taken into account [59]. Later, the lattice was also considered for the dissipation of the angular momentum via Elliott-Yafet spin-flip scattering [60]. Another completely different route to explain the ultrafast demagnetization was also proposed based on superdiffusive spin transport [61]. In this model, a spin-polarized superdiffusive current is excited by the laser pulse, and causes the ultrafast demagnetization. This theoretical transport model has later been experimentally proven to contribute significantly to the ultrafast demagnetization [62]. However, the origin of the ultrafast demagnetization is still very much under debate.

The second type of magnetization dynamics, the magnetization precession and damping, spans from a few picoseconds to nanoseconds. Classically, this motion can be visualized as the magnetization vector precessing around the equilibrium magnetic field, with the precession amplitude decreasing over time, as shown in Fig. 1.1(b). When all the magnetization vectors are precessing in-phase, a ferromagnetic resonance (FMR) is achieved [63]. Such a phenomenon is a powerful tool to characterize magnetic properties. In addition to FMR, if the phase of the precession varies in space, it often corresponds to a propagating spin wave. Research in the field of spin waves has significantly increased recently [64–70], due to the potential of spin waves to transmit information. This research area, where the spin waves are used as information carriers and processors, is referred to as magnonics [22]. The study of magnetization precession and magnonics are the focus of this thesis, and will be explained in detail in the following sections.

The third type of magnetization dynamics, domain wall motion, occurs at a much slower time scale, i.e. microseconds. The motion of a domain wall can be effectively driven by applying an appropriate torque, which is realized by the injection of spin-polarized current [10, 11]. One of the most appealing applications for domain walls is to build a domain-wall racetrack memory, which is a 3D structure where the data information is encoded in the magnetic domain pattern [17]. Many domain-wall logic devices have also been demonstrated, where the digital information 0/1 is encoded in the two magnetization states, and the switching between 0 and 1 is obtained by the injection of domain walls [71, 72].

1.2.2. Magnetization precession and damping

Magnetization precession and damping are often described by the Landau-Lifshitz-Gilbert (LLG) Equation [73], which is given by

$$\frac{d\mathbf{M}}{dt} = \gamma\mu_0(\mathbf{M} \times \mathbf{H}_{\mathrm{eff}}) + \frac{\alpha}{M_{\mathrm{S}}}(\mathbf{M} \times \frac{d\mathbf{M}}{dt}). \tag{1.8}$$

Here, M_{S} is the saturation magnetization, $\mathbf{H}_{\mathrm{eff}}$ is the total effective magnetic field, and α is the Gilbert damping. The original form the LLG equation is the Landau-Lifshitz equation [4], which is

$$\frac{d\mathbf{M}}{dt} = \gamma\mu_0(\mathbf{M} \times \mathbf{H}_{\mathrm{eff}}) + \frac{\lambda\gamma\mu_0}{M_{\mathrm{S}}}\mathbf{M} \times (\mathbf{M} \times \mathbf{H}_{\mathrm{eff}}). \tag{1.9}$$

It can be seen that the expressions of the second term on the right hand side in Eqs. (1.8) and (1.9) are different. However, if the magnetization is only slightly perturbed from its equilibrium position, these two expressions are equivalent. By analyzing the dimensions of the LLG equation, it can be seen that it is a torque equation. The left hand side represents the rate of change of the magnetic angular momentum. On the right hand side, there are two torque terms that drive the motion of the magnetization. To visualize the effects of the two torque terms, their directions are shown in Fig. 1.2. The first term is called the precession term. As indicated by the red arrow, this torque drives the magnetization to precess around the effective field $\mathbf{H}_{\mathrm{eff}}$. Here, it should be noted that the direction of the precession torque is given by $-\mathbf{M} \times \mathbf{H}_{\mathrm{eff}}$, since the sign of γ is negative. The second term is the damping term, indicated by the blue arrow, which points towards the equilibrium position for the magnetization. The effect of this torque is to reduce the amplitude of precession, and hence let the magnetization relax to its equilibrium position.

The precessional part of the LLG equation is particularly interesting as it is the driving torque for determining the spin-wave frequency and wavelength. The

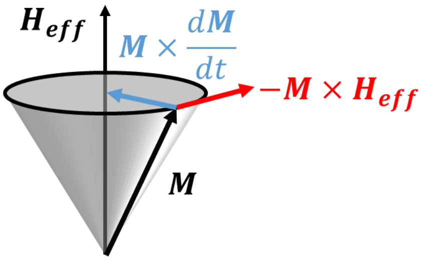

Figure 1.2. Schematic of magnetization precession and damping. The directions of the two torques are indicated with the arrows with different colors.

driving field for this torque, $\mathbf{H}_{\text{eff}}$, can be deduced from

$$\mathbf{H}_{\text{eff}} = -\frac{1}{\mu_0}\frac{\partial\mathcal{H}}{\partial\mathbf{M}}, \tag{1.10}$$

where $\mathcal{H}$ is the Hamiltonian of the system. This effective field can have many origins. In the framework of this thesis, the following sources are considered,

$$\mathbf{H}_{\text{eff}} = \mathbf{H}_{\text{ex}} + \mathbf{H}_{\text{ext}} + \mathbf{H}_{\text{demag}}, \tag{1.11a}$$

$$\mathbf{H}_{\text{ex}} = \lambda_{\text{ex}}\nabla^2\mathbf{M}, \tag{1.11b}$$

$$\mathbf{H}_{\text{demag}} = -\overline{N}^{\text{a}} \cdot \mathbf{M}. \tag{1.11c}$$

Here, we consider the total effective field with mainly three contributions [see Eq. (1.11a)], the exchange field, the applied external field and the demagnetization field. λ_{ex} is a constant related to the exchange field , and $\overline{N}^{\text{a}}$ is the demagnetizing tensor. The exchange field originates from the exchange interaction. From Eq. (1.8), only the part that is perpendicular to **M** will contribute to the torque, so here only the non-uniform part of the exchange field is considered, which is proportional to $\nabla^2\mathbf{M}$. The second contribution to the effective field is from the Zeeman interaction, and $\mathbf{H}_{\text{ext}}$ is simply the applied magnetic field. The third contribution is the demagnetization field, whose origin is from magnetostatics. The characteristics of the demagnetization field is contained in the demagnetizing tensor, which is determined by the geometry of the magnetic object. When considering the simple case of a uniformly magnetized ellipsoid with principal axes x, y and z, the tensor is of a diagonal matrix form as follows,

$$\begin{pmatrix} N_{xx} & 0 & 0 \\ 0 & N_{yy} & 0 \\ 0 & 0 & N_{zz} \end{pmatrix}, \tag{1.12}$$

where $N_{xx} + N_{yy} + N_{zz} = 1$. For example, for an infinite uniformly in-plane magnetized thin film in the XY plane, $N_{zz} = 1$ and $N_{xx} = N_{yy} = 0$. Therefore, only the out-of-plane component of the magnetization will generate the demagnetization field.

The second term in the LLG equation is the damping term, which is in the first instance introduced as a phenomenological term in order to let the magnetization relax to its equilibrium position. The damping is characterized by a dimensionless parameter α, which is only determined by the material properties. This damping parameter is commonly referred as the intrinsic damping of the material, whose origin is the spin-orbit coupling [74]. To experimentally determine this parameter, the line width at the half maximum of the ferromagnetic resonance (FMR) peak is often used [75]. In a real magnetic system, there are many other contributions to the damping term, which together contribute to the so-called the extrinsic damping.

One common contribution is the inhomogeneity of the applied magnetic field. This inhomogeneity can equivalently cause the dephasing between the spins, and hence increase the damping [76]. Other possible sources of the extrinsic damping are the non-local spin relaxation processes [77, 78] and two-magnon scattering process [79].

In addition to the descriptions of the magnetization precession based on the LLG equation, the precessional dynamics can also be understood in the framework of thermodynamics and statistics. In this case, perturbations of the static magnetization are thermal fluctuations of the system. At given temperature T, for all magnetic configurations, the free energy of the system F should be minimized, which is defined as,

$$F = E - TS. \tag{1.13}$$

Here, E is the total energy considering all the magnetic interactions, T is the absolute temperature, and S is the system entropy. The entropy S is a measure of the possible microstates and is defined as,

$$S = k_\mathrm{B} \log \Omega, \tag{1.14}$$

where k_B is the Boltzmann constant, and Ω is the number of states. The ground state of a magnetic system is defined as the magnetic configuration at $T = 0$. If there is only one possible ground state, e.g. all the spins are aligned in the same direction, the entropy of the system is zero. Although the increase of the temperature increases the energy E, it can lower the total free energy through the term $-TS$. Therefore, the effect of the temperature is to populate excited states above the ground state. These excited states are often of a collective nature, with the low energy collective excitations being well describe by spin waves. The quanta of the spin waves are referred as magnons. An example of the spin waves can be obtained by considering the excitations of a 1D ferromagnetic chain with a Heisenberg Hamiltonian of the form of $\mathcal{H}_\mathrm{ex}^\mathrm{S}$ in Eq. (1.7b). In this system, all spins are equally spaced at the distance a. For the lowest excited state with one spin flip $\Delta S = 1$, the dispersion relation is [80],

$$\hbar\omega(k) = \hbar^2 J_{ij}[1 - \cos(ka)]. \tag{1.15}$$

This excitation results in a collective precession of all the spins. The wave nature of this excitation is that the phase shift of the precession between the neighboring spins is ka. Therefore, k is defined as the wavevector of the spin wave, and the corresponding wavelength is $\lambda = 2\pi/k$. From the energy point of view, the wavevector quantifies how much non-collinear the neighboring spins are, and hence how much exchange energy is involved in this excitation. This amount of energy quanta $\hbar\omega$ also has a representation in the time domain, in terms of $2\pi/\omega$, effectively meaning that higher energy magnon corresponds to a shorter precession period.

1.3. Magnetostatic spin waves

In the framework of this thesis, we mainly focus on the spin-wave dynamics occurring in the gigahertz range and at the micrometer length scale. In this regime, the governing interactions are the Zeeman and dipolar interactions. Therefore, these spin waves are commonly referred as the magnetostatic spin waves or dipolar spin waves.

To determine the spin-wave modes, in particular the dispersion relations for different spin-wave modes, the LLG equation needs to be rearranged into a more suitable form. For simplicity, only the precessional part is used, which is

$$\frac{d\mathbf{M}}{dt} = \gamma\mu_0(\mathbf{M} \times \mathbf{H}_{\mathrm{eff}}). \tag{1.16}$$

The expressions for the magnetization and magnetic field are separated into the static and dynamic parts, which are

$$\mathbf{M} = \mathbf{M}_0 + \mathbf{m}(t), \tag{1.17a}$$

$$\mathbf{H}_{\mathrm{eff}} = \mathbf{H}_0 + \mathbf{h}(t). \tag{1.17b}$$

Substituting them into Eq.(1.16) gives

$$\frac{d\mathbf{m}}{dt} = \gamma\mu_0(\mathbf{M}_0 \times \mathbf{H}_0 + \mathbf{M}_0 \times \mathbf{h} + \mathbf{m} \times \mathbf{H}_0 + \mathbf{m} \times \mathbf{h}). \tag{1.18}$$

Before solving this equation, some simplifications can be made. We first assume that $\mathbf{M}_0$ aligns with $\mathbf{H}_0$, which is chosen to be the $\hat{z}$ direction, and the two dynamic components are rather small when compared with the static components. Therefore, the first term in Eq.(1.18) can be assumed to be zero, and the last term can be neglected. Furthermore, we assume that the static magnetization is equal to the saturation magnetization value M_{S}, and the time dependence of the dynamic part, for both $\mathbf{m}(t)$ and $\mathbf{h}(t)$, is of the form $e^{-i\omega t}$. As a result, Eq.(1.18) can then be written as,

$$-i\omega\mathbf{m} = \hat{z} \times (-\omega_{\mathrm{M}}\mathbf{h} + \omega_0\mathbf{m}), \tag{1.19}$$

with

$$\omega_{\mathrm{M}} = -\gamma\mu_0 M_{\mathrm{S}}, \tag{1.20a}$$

$$\omega_0 = -\gamma\mu_0 H_0. \tag{1.20b}$$

Next, Eq.(1.19) is rearranged into the following form,

$$\mathbf{m} = \overline{\chi} \cdot \mathbf{h}, \tag{1.21}$$

whose explicit expression is,

$$\begin{bmatrix} m_x \\ m_y \end{bmatrix} = \begin{bmatrix} \chi & -i\kappa \\ i\kappa & \chi \end{bmatrix} \begin{bmatrix} h_x \\ h_y \end{bmatrix}, \tag{1.22}$$

where

$$\chi = \frac{\omega_0 \omega_{\mathrm{M}}}{{\omega_0}^2 - \omega^2}, \tag{1.23a}$$

$$\kappa = \frac{\omega \omega_{\mathrm{M}}}{{\omega_0}^2 - \omega^2}. \tag{1.23b}$$

The dynamic susceptibility tensor $\overline{\chi}$ in Eq. (1.21) relates both dynamic components of the magnetization and the magnetic field. In some simple cases, Eq. (1.21) can be directly solved, such as for the FMR case where the expressions for **h** are simple. However, for magnetostatic spin waves, directly solving Eq. (1.21) is too complex. Therefore, the dynamic susceptibility tensor is used to solve the magnetostatic conditions in a self consistent way. The magnetostatic conditions are the following,

$$\nabla \times \mathbf{h} = 0, \tag{1.24a}$$

$$\nabla \cdot \mathbf{b} = 0. \tag{1.24b}$$

The two quantities **h** and **b** are related via the constitutive relation, which is

$$\mathbf{b} = \overline{\mu} \cdot \mathbf{h} = \mu_0(\overline{\mathbf{I}} + \overline{\chi}) \cdot \mathbf{h}. \tag{1.25}$$

The explicit expression for the dynamic permeability tensor is

$$\overline{\mu} = \mu_0 \begin{bmatrix} 1+\chi & -i\kappa & 0 \\ i\kappa & 1+\chi & 0 \\ 0 & 0 & 1 \end{bmatrix}. \tag{1.26}$$

To solve the magnetostatic conditions, using Eq. (1.24a), we write **h** as,

$$\mathbf{h} = -\nabla\phi, \tag{1.27}$$

where ϕ is the magnetic scalar potential. Substituting the constitutive relation into Eqs. (1.24) gives,

$$\nabla \cdot (\overline{\mu} \cdot \nabla\phi) = 0. \tag{1.28}$$

This equation can be rewritten as,

$$(1+\chi)(\frac{\partial^2\phi}{\partial x^2} + \frac{\partial^2\phi}{\partial y^2}) + \frac{\partial^2\phi}{\partial z^2} = 0. \tag{1.29}$$

Eq. (1.29) is commonly referred as the Walker's equation, whose solutions are the magnetostatic spin-wave modes.

In the framework of this thesis, we discuss the magnetostatic spin waves in ferromagnetic thin films. Due to the nature of magnetostatic interactions, magnetostatic spin waves are highly anisotropic when compared with exchange spin waves. More specifically, the behavior of the dipolar spin waves strongly depends on both the static magnetization configuration and the relative orientation between the magnetization vector the spin-wave wavevector. Accordingly, the spin waves are classified into three categories,

- magnetostatic surface mode: in-plane magnetized, $\mathbf{k} \perp \mathbf{M}$ [Fig. 1.3(a)];
- magnetostatic backward volume mode: in-plane magnetized, $\mathbf{k} \parallel \mathbf{M}$ [Fig. 1.3(b)];
- magnetostatic forward volume mode: out-of-plane magnetized [Fig. 1.3(c)].

For consistency, the coordinate system for each mode is defined where $\hat{z}$ is along the magnetization direction.

The three modes differ from each other in terms of their dispersion relations $\omega(k)$. For the magnetostatic surface mode, the dispersion relation is rather simple, which is

$$\omega^2 = \omega_0(\omega_0 + \omega_M) + \frac{{\omega_M}^2}{4}(1 - e^{-2kd}), \tag{1.30}$$

where d is the thickness of the ferromagnetic film. For the magnetostatic backward volume mode, the solutions consist of a manifold of spin waves. The dispersion relation for the spin wave with mode number n is

$$\tan[\frac{kd}{2\sqrt{-(1+\chi)}} - \frac{(n-1)\pi}{2}] = \sqrt{-(1+\chi)}, n = 1, 2, 3 \ldots \tag{1.31}$$

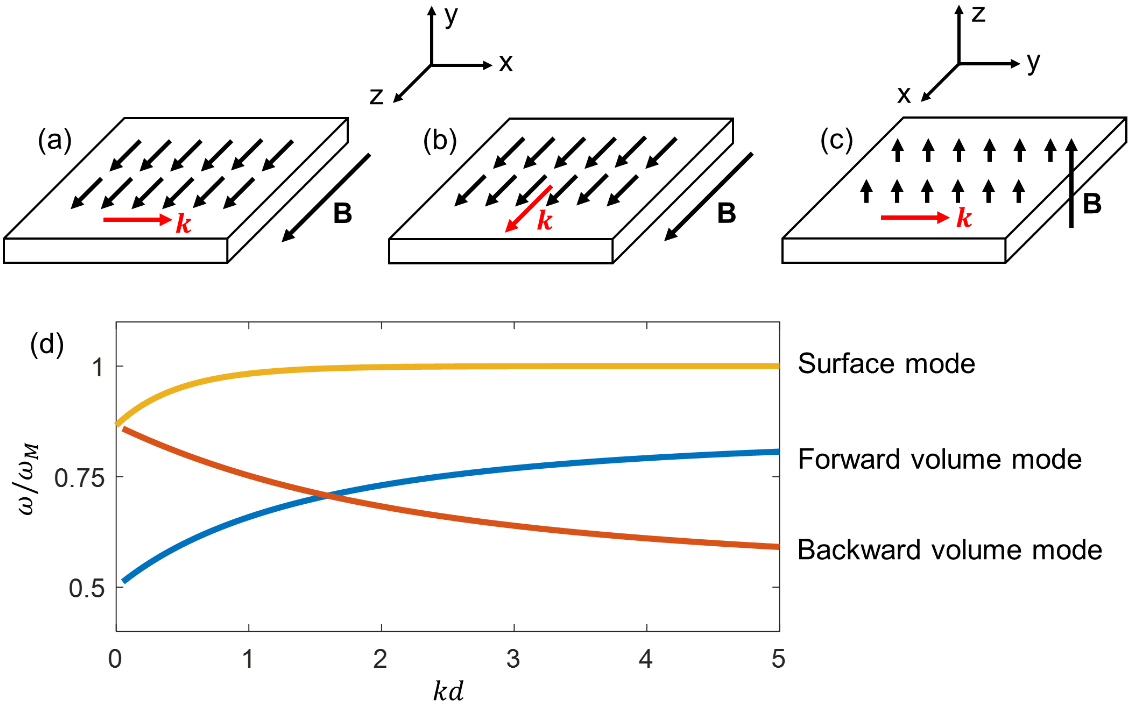

Figure 1.3. (a)-(c) Static magnetization configuration and wavevector orientation for the three magnetostatic spin-wave modes. (a) and (b) share the same coordinates, and (c) is in another coordinate system. (d) Scaled spin-wave dispersion relation for the three magnetostatic spin-wave modes with $\omega_0/\omega_M = 0.5$ corresponding to (a)-(c). The two volume modes are the lowest-order modes.

For the magnetostatic forward volume mode, the dispersion relation is

$$\tan[\frac{kd}{2}\sqrt{-(1+\chi)}-\frac{n\pi}{2}]=\frac{1}{\sqrt{-(1+\chi)}}, n=0,1,2... \tag{1.32}$$

For both volume modes, the dispersion relations are of the complex form, where ω and k are related via χ. The manifold nature of these two modes is represented by the periodicity of the tan function. To better visualize these dispersion relations, the scaled dispersion relations for the three modes, $\omega/\omega_{\mathrm{M}}$ as a function of kd with $\omega_0/\omega_{\mathrm{M}}=0.5$, are plotted in Fig. 1.3(d). For the backward and forward volume modes, the dispersion relations for lowest-order modes are plotted, which can be approximated as,

$$\omega^2=\omega_0[\omega_0+\omega_{\mathrm{M}}(\frac{1-e^{-kd}}{kd})], \tag{1.33a}$$

$$\omega^2=\omega_0[\omega_0+\omega_{\mathrm{M}}(1-\frac{1-e^{-kd}}{kd})], \tag{1.33b}$$

respectively. From the dispersion relation, the group velocity for the mode can be inferred, which is

$$v_g=\frac{\partial\omega}{\partial k}. \tag{1.34}$$

Comparing the dispersion curves in Fig. 1.3(d), when $k>0$, for the surface and forward volume modes, $v_g>0$, whereas for the backward volume modes, $v_g<0$. When v_g and k are of the same sign, the solution is referred to as a forward mode, otherwise it is referred to as a backward mode.

To further understand the properties of each mode, solutions of the potential function ϕ in Eq.(1.29) need to be analyzed. From the expressions of ϕ, $\mathbf{h}$ and $\mathbf{m}$ can also be inferred. In the dispersion relation discussed previously, the wavevector k is introduced, which is the in-plane propagation vector for the spin waves. However, this is only one component of the spin-wave wavevector, with the other component of the wavevector being in the out-of-plane direction. For consistency, we still denote the in-plane component as $\mathbf{k}$, and the out-of-plane component as $\mathbf{k}_{\mathrm{oop}}$.The solution of ϕ inside the film, for the magnetostatic surface mode is,

$$\phi_\nu(\mathbf{r})=\phi_0[e^{k_{\mathrm{oop}}}+p(\nu)e^{-k_{\mathrm{oop}}}]e^{i\nu kx}. \tag{1.35}$$

Here, $\nu=\pm1$ indicates the two opposite directions of propagation. ϕ_0 is an arbitrary constant related to the potential amplitude, $p(\nu)$ is a function of ν which modifies the distribution along the film thickness. For the backward volume mode, the solutions of the odd and even modes are,

$$\phi^{\mathrm{odd}}(\mathbf{r})=\phi_0\sin(k_{\mathrm{oop}}y)e^{i\nu kz}, \tag{1.36a}$$

$$\phi^{\mathrm{even}}(\mathbf{r})=\phi_0\cos(k_{\mathrm{oop}}y)e^{i\nu kz}. \tag{1.36b}$$

For the forward volume mode, the solutions of the even and odd modes are,

$$\phi^{\mathrm{even}}(\mathbf{r}) = \phi_0 \cos(\sqrt{-(1+\chi)}\, k_{\mathrm{oop}} z) e^{i\mathbf{k}\cdot\mathbf{r}}, \tag{1.37a}$$

$$\phi^{\mathrm{odd}}(\mathbf{r}) = \phi_0 \sin(\sqrt{-(1+\chi)}\, k_{\mathrm{oop}} z) e^{i\mathbf{k}\cdot\mathbf{r}}. \tag{1.37b}$$

For all three modes, along the in-plane direction, the potential function takes the form of a plane wave, characterized by its wavevector is $\mathbf{k}$. In the out-of-plane direction, there are two different distributions of the potential function. For both the backward and forward volume mode, the distribution has a sinusoidal form along the film thickness, similar to the form of a standing wave. Therefore, they are referred to as the volume modes. In contrast, for the surface mode, the amplitude of the potential function decays exponentially from the surface towards the inside of the film. Due to this property, the potential function is localized on one of the film surfaces, which is why it is referred to as a surface mode. The magnetostatic surface mode is also commonly referred to as the Damon-Eshbach mode [33].

These different properties, i.e. the dispersion relation and amplitude distribution of the potential function, give rise to the anisotropic behavior of the magnetostatic spin waves, which result from the dipolar interaction and the boundary conditions of the Maxwell's equations. In addition, these modes are strongly dependent on the strength of the applied magnetic field. For example, for a special case where $k = 0$, these modes reduce to the scenario of the ferromagnetic resonance, giving

$$\omega_{\mathrm{IP}} = |\gamma|\mu_0 \sqrt{H_{\mathrm{ext}}(H_{\mathrm{ext}} + M_{\mathrm{S}})}, \tag{1.38a}$$

$$\omega_{\mathrm{OOP}} = |\gamma|\mu_0 (H_{\mathrm{ext}} - M_{\mathrm{S}}). \tag{1.38b}$$

for the in-plane and out-of-plane magnetized cases, respectively. From these expressions, the dependence on the applied magnetic field can be clearly seen.

Until now, both magnetostatic spin waves and one example of exchange spin waves are introduced. They are equally important in terms of characterizing the dynamic properties of magnetic materials. Nevertheless, they are in general well separate in different frequency ranges and wavelengths. From Fig. 1.4 [81], it can be seen that an overlap between the exchange and magnetostatic spin waves occurs at the length scales from several tens of nanometers to several hundreds of nanometers. Above 1 μm, the spin waves are completely dominated by magnetostatic interactions, with the corresponding frequency in the GHz range. Below 20 nm, the spin waves are completely dominated by exchange interactions, with the corresponding frequency in the THz and sub THz range. In this case, inelastic neutron scattering is often used to investigate exchange spin waves [82, 83].

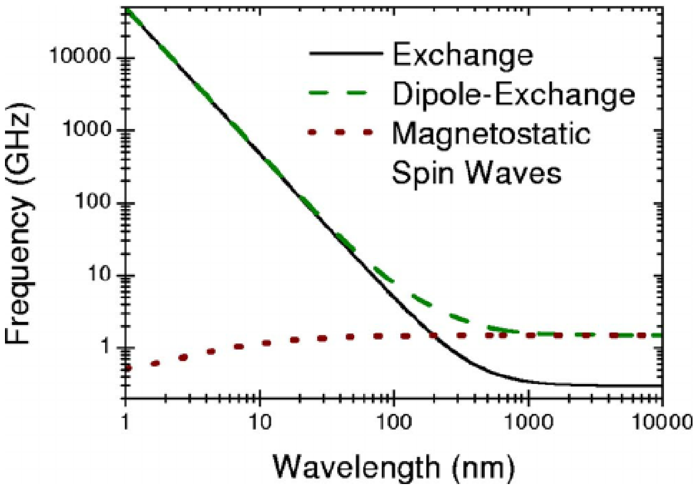

Figure 1.4. Frequency relation of exchange, dipole-exchange, and magnetostatic spin waves as a function of wavelength for a 5 nm yttrium-iron garnets (YIG), while neglecting anisotropy and assuming that the wavevector is parallel to the equilibrium magnetization direction. [81]

1.4. Experimental methods for investigating magnetostatic spin waves

Previously, the properties of the magnetostatic spin waves have been discussed. Before utilizing different spin-wave properties to transmit and process information, the principles of spin-wave excitation and detection need to be introduced.

1.4.1. Principles of excitation

In general, the excitation of spin waves requires the perturbation of the ordered magnetic state of the system. The excitation can be either global or local, which in general corresponds to the case of ferromagnetic resonance or propagating spin waves, respectively. Many methods can be used for the excitation, such as a radio-frequency (RF) magnetic field [80], an ultrafast laser pulse [84] and spin-polarized current [85]. In the framework of this thesis, we divide the excitation methods into two categories, the electrical and optical methods. For the electrical methods, we only discuss the RF magnetic field approach. For the optical methods, we discuss mainly two approaches, using an ultrafast laser pulse and the Brillouin light scattering (BLS) technique [86]. All three techniques are widely used for magnonics research, and the first two techniques are used in our experiments.

The principle of the RF magnetic field approach is to use the Oersted field generated by an RF current. The RF current is often carried by an RF antenna. Two types of antennas are often used, namely a microstrip and a coplanar waveguide (CPW), as shown in Figs. 1.5(a) and (c). The microstrip [Fig. 1.5 (a)] consists of the signal transmission line (S) on top of the dielectric substrate, whose lower surface is coated with a metal plate that serves as the ground (G). The relevant geometric parameter for the microstrip is the width of the signal line w. The CPW [see Fig. 1.5(c)] consists of one signal line placed in between the two ground lines, which are all placed on top of a dielectric substrate. Three relevant geometric parameters for the CPW are the width of the signal line w_1, width of the ground line w_2, and the gap width s between the signal and ground lines.

For the RF excitation technique, two important aspects need to be considered for the spin-wave excitation. One is the RF transmission efficiency, which is usually optimized by matching the total impedance of the RF antenna to 50 Ω. The other aspect is to match the excited spin-wave frequency with the corresponding RF excitation wavelength. To achieve this, one must choose the right geometry of the antennas. For the microstrip, a schematic of the Oersted field distribution is shown in Fig. 1.5(b). This magnetic field can be viewed as a global uniform excitation, if the magnetic material is on either the top or bottom of the signal line, and its size is much smaller than the signal line. In this case, the excited dynamics corresponds approximately to the ferromagnetic resonance. When the size of the signal line is much smaller than the magnetic sample, for example, a signal line on top of a magnetic film, the Oersted field then acts as a local excitation. In this case, the power spectrum of the Fourier transform of the spatial distribution of the Oersted field corresponds to the excitation efficiency of the spin waves as a function of k [87, 88]. For this case, the wavelength of spin waves λ with the highest excitation efficiency is close to the value of w. For the CPW, the situation is similar. The wavelength of the spin wave with the highest excitation efficiency is given by the distance between the centers of the signal and ground lines, which is $(w_1 + s + w_2)/2$.

Since the excitation fields are around the antenna, the spin waves must propagate away from the antenna. If we define a unit vector $\hat{a}$, which is along the signal line direction, then the wavevector should be perpendicular to $\hat{a}$. Therefore, the magnetic field should be applied along $\hat{a}$ for the Damon-Eashbach mode, perpendicular to $\hat{a}$ but still in-plane for the backward volume mode, and along the out-of-plane

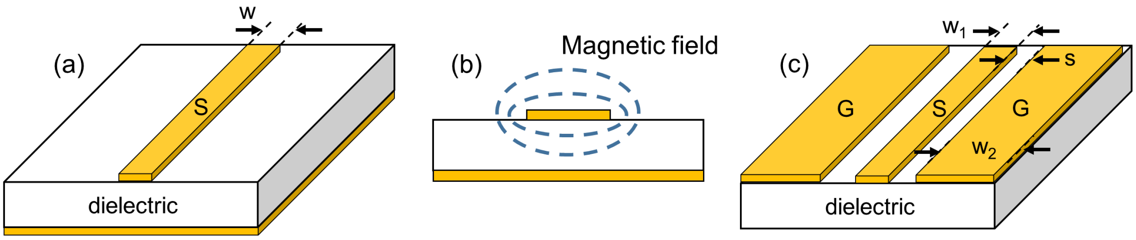

Figure 1.5. (a) and (c) Schematics of the microstrip and coplanar waveguide. (b) Schematic of the magnetic distribution for a cross section of the microstrip.

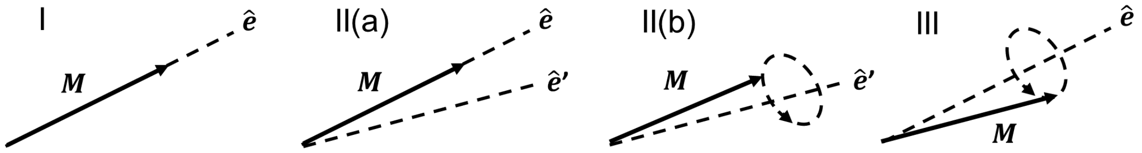

Figure 1.6. Three time stages for the laser-induced precession [84]. $\hat{e}$ points along the equilibrium axis of the magnetization, and $\hat{e}'$ points towards the transient equilibrium position at time stage II.

direction for the forward volume modes. The precision of the excited spin wave with f_0 and λ_0 is guaranteed by the frequency of the RF current, since these days the frequency precision of the RF synthesizer is extremely high. For the wavelength, the correct geometric parameters of the antenna must be chosen so that the excitation efficiency at λ_0 is high.

Apart from the electrical method, the optical methods are also quite efficient at exciting the spin-wave dynamics. In the following, we first introduce the method of using the ultrafast laser pulse. Then we briefly describe the BLS technique. As already introduced in Sec. 1.2.1, the femtosecond laser pulse can induce ultrafast demagnetization within 1 ps. Following this ultrafast demagnetization, if certain conditions are met, a coherent precession can be also induced [84]. A general three-stage process is illustrated in Fig. 1.6 for the laser-induced coherent precession. At stage I, $t < 0$, the magnetization is at equilibrium along $\hat{e}$. At stage II(a), $t = 0$, the laser pulse arrives and heats the magnetic material, and hence changes the total anisotropy field. The total anisotropy field can contain all possible contributions from the shape anisotropy, magneto-crystalline anisotropy and surface anisotropy. Subsequently, the equilibrium axis will change to $\hat{e}'$. At time stage II(b), $0 < t < 10$ ps, the magnetization is not aligned with $\hat{e}'$, and hence will start to precess around $\hat{e}'$. At stage III, $t > 10$ ps, as the heat dissipates, the equilibrium axis returns to $\hat{e}$. Since the magnetization is still not aligned with $\hat{e}$, it will continue to precess but along $\hat{e}$. From this stage on, a coherent precession is induced that can last up to a nanosecond.

From the complex process described above, two necessary conditions are required in order to excite such a coherent precession. The first requirement is that the laser pulse duration should be extremely short so that the time between stage II and III can be well differentiated. The second requirement is that the laser heating must induce a change of the transient equilibrium axis from $\hat{e}$ to $\hat{e}'$. Otherwise, the magnetization will not start to precess.

This method is often used in the all-optical pump-probe experiment with magneto-optical effects to observe the time evolution of the magnetization. Moreover, if the laser beam is well focused, a propagating spin wave can also be excited [89]. Apart from using the heat of the laser to excite spin waves, there are other properties of the laser pulse that can be used to excite the spin-wave dynamics, such as the inverse Faraday effect [90].

While not being used in this thesis, we briefly mention the second optical method, which is the BLS technique. It is an inelastic scattering process, where photons exchange energy and momentum with magnons [22]. The change of the frequency and wavevector $(\Delta\omega, \Delta\mathbf{k})$ of the scattered photons are the same as the frequency and wavevector of the scattering magnons. Strictly speaking, the BLS technique is not only an excitation method, since by measuring $(\Delta\omega, \Delta\mathbf{k})$ the detection of the spin waves is simultaneously achieved. This parts will be further explained in the next section, from the perspective of spin-wave detection.

1.4.2. Principles of detection

For the detection of spin waves, we again divide the methods into two main categories, the optical and electrical methods. For the optical methods, we focus on the magneto-optical Kerr effect (MOKE), which is the detection method used for all our experiments. The other one, the magneto-optical Faraday effect, is based on the same principle, but in the transmission geometry. Moreover, the BLS technique is also explained briefly, as it is a widely used in magnonics research. For the electrical methods, we introduce the use of vector network analyzer (VNA) to detect spin-wave signals.

MOKE describes the change of polarization of light, upon reflection from a magnetic material, which resulted from the light matter interaction. In this thesis, MOKE in magnetic thin films is explained, which is the main detection principle for the experiments. Depicted in Fig. 1.7 are the three different MOKE geometries:

- Polar MOKE: **M** is out-of-plane;
- Longitudinal MOKE: **M** is in-plane, and also in the optical plane of incidence;
- Transverse MOKE: **M** is in-plane, and perpendicular to the optical plane of incidence.

As indicated by polarization vector of the incident and reflected light, for the polar and longitudinal geometries, a linearly polarized light becomes elliptically

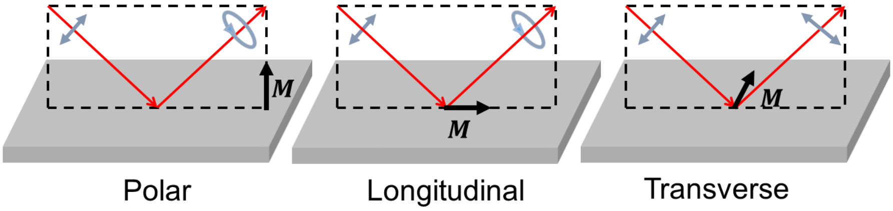

Figure 1.7. Three MOKE geometries. The dashed plane is plane of incidence.

polarized. Whereas for the transverse geometry, the light remains linearly polarized and changes intensity.

To illustrate the principle of MOKE, we use the example of the polar MOKE. We assume that the film is magnetized along the $\hat{z}$ direction, which is the out-of-plane direction. The dielectric tensor for such a medium is of the following form [91]

$$\bar{\boldsymbol{\varepsilon}} = \begin{bmatrix} \varepsilon & \varepsilon' & 0 \\ -\varepsilon' & \varepsilon & 0 \\ 0 & 0 & \varepsilon \end{bmatrix}. \tag{1.39}$$

The two off-diagonal terms $\varepsilon_{xy} = \varepsilon'$ and $\varepsilon_{yx} = -\varepsilon'$ represent the magneto-optical effect. As can be seen from the constitutive relation Eq.(1.4a), E_x contributes to D_y with a factor of $-\varepsilon'$, and E_y contributes to D_x with a factor if ε. These contributions already indicate a change of the polarization of light induced by the magneto-optical interaction. Solutions of the light propagating in the film of the form $\mathbf{E}_0 e^{i(\mathbf{k}\cdot\mathbf{r}-\omega t)}$ can be obtained by solving the Maxwell's equations using the dielectric tensor in Eq.(1.39). The two important parameters are $\mathbf{E}_0$ that can be used to identify the polarization state, and $\mathbf{k}$ the propagation vector. For the polar geometry, two eigenmodes can be obtained,

$$\mathbf{E}_{0,1} = (E_{x,1}, iE_{x,1}, 0), \quad \mathbf{k}_1 = (0, 0, -k_0\sqrt{\varepsilon + i\varepsilon'}); \tag{1.40a}$$

$$\mathbf{E}_{0,2} = (E_{x,2}, -iE_{x,2}, 0), \quad \mathbf{k}_2 = (0, 0, -k_0\sqrt{\varepsilon - i\varepsilon'}). \tag{1.40b}$$

These two eigenmodes can be identified as the left and right circularly polarized light with the two different refractive indices, which are

$$n_1 = \sqrt{\varepsilon + i\varepsilon'}, \tag{1.41a}$$

$$n_2 = \sqrt{\varepsilon - i\varepsilon'}. \tag{1.41b}$$

The different $\mathbf{k}$ of the two eigenmodes imply that they propagate with different phase velocities. For an intuitive understanding of the two different wavevectors for the left and right circularly polarized light, one could consider effects from two different circularly polarized light to the magnetic materials. These two circulating electric fields, one clockwise and one counterclockwise, can induce two circular motions of electrons in the materials, one counterclockwise and one clockwise, which subsequently produce two magnetic fields with opposite directions. As a result, these two magnetic fields can delay the propagation of one of the circularly polarized light and advance the other one. Based on this fact, the principle of MOKE can be explained as follows. When a linearly polarized light is incident on the surface, it can be decomposed into the left and right circularly polarized components. Upon reflection, since the two components have different refractive indices, the amplitude ratio and phase difference between the two components will change. When the reflected light is then recovered by superimposing these two components, the polarization state is changed. The change of the polarization is often characterized by the Kerr rotation ϕ' and ellipticity ϕ''. For s- and p-polarized light, the general expressions of these two quantities are as follows,

$$\phi_s = \phi'_s + i\phi''_s = \frac{r_{ps}}{r_{ss}}, \tag{1.42a}$$

$$\phi_p = -\phi'_p + i\phi''_p = \frac{r_{sp}}{r_{pp}}, \tag{1.42b}$$

where r_{ss}, r_{sp}, r_{ps} and r_{pp} are the four components of the reflection matrix. From this perspective, for the polar and longitudinal geometries, r_{sp} and r_{ps} are non-zero. Therefore, a change of the polarization can be observed. For the transverse geometry, $r_{sp} = r_{ps} = 0$, and hence the change of polarization is absent and the MOKE signal is represented by the change of light intensity.

For our experiments, the polar MOKE geometry is used to detect the out-of-plane component of the magnetization. Since we are investigating in-plane magnetized samples, the behavior of out-of-plane component is a good measure of the magnetization dynamics.

Apart from the magneto-optical effects, another important optical method for detecting spin waves is the BLS technique. As already explained, by measuring $(\Delta\omega, \Delta\mathbf{k})$ of photons scattered by a magnetic sample, the frequency and wavevector of the corresponding magnons can be mapped. By measuring the different $(\Delta\omega, \Delta\mathbf{k})$ pairs, the spin-wave dispersion can be directly mapped [92], which is the biggest advantage of the BLS technique. Another advantage of the BLS is that it can detect both thermal magnons and externally pumped magnons [22]. Recently, many adaptations of this technique have been implemented to enhance its functionality. For example, for the micro-focus BLS, the laser light is focused to a spot size of a few hundreds of nanometers, which is used to image the spin waves [93, 94]. Moreover, the phase sensitive micro-focus BLS technique is also developed, which can be used to image both the power and phase distribution of the spin waves [95].

Finally, the VNA for detecting the spin waves is explained. In RF engineering, VNA is often used to measure the S-parameters for the circuit network [25]. For example, for a two-port network, the relationship between the reflected and incident waves is given by,

$$\begin{bmatrix} b_1 \\ b_2 \end{bmatrix} = \begin{bmatrix} S_{11} & S_{12} \\ S_{21} & S_{22} \end{bmatrix} \begin{bmatrix} a_1 \\ b_2 \end{bmatrix}. \tag{1.43}$$

The 2×2 matrix is commonly referred as the S-parameter matrix, and a_i and b_i are the amplitude of thes incident and reflected waves. From this relationship, it can be seen that, for a certain port i, b_i has two contributions. For example, for b_1, one contribution is the reflection from its own port $S_{11}a_1$, and the other is the transmission from the other port $S_{12}b_2$. In general, the S-parameters are complex numbers.

For exciting and detecting the propagating spin waves, a two-port network is needed. For each port, this can be realized by a microstrip or CPW, and the two ports are separated by a certain distance to allow for the spin-wave propagation. In the following, we assume Port 1 is for the excitation, and Port 2 is for the detection. Then it is often the case that the imaginary part of S_{21} is measured as a function of frequency. The peak in this spectrum indicates the frequency of the detected spin waves. From here, it can be seen that the VNA can also be used to excite the spin waves, but the principle is the RF magnetic field technique.

The principle of using a VNA to detect the spin waves is the opposite process of using the RF field to excite the spin waves. When the propagating spin waves arrive at Port 2, the precessing magnetization generates a dynamical magnetic flux $\Phi(t)$, which through induction will generate a voltage on the CPW. This voltage is then measured by the VNA to further extract the S-parameters. Moreover, in certain cases, by carefully fitting the $\mathrm{Im}\{S_{21}\}(f)$ curve, the wavevector of the spin waves can be extracted [87].

To summarize all the methods above, for the electrical method, the RF field method uses the Oersted field to drive the magnetization precession and hence excites the spin waves. The VNA technique measures the voltage inductively induced by the precessing magnetization, and hence detects the spin waves. For the optical method, the BLS technique uses an inelastic scattering process to generate and detect the spin waves. For the ultrafast laser technique, the heating of the laser is often used for the excitation, and MOKE is used for the detection. Each method has its pros and cons, and generally electrical and optical methods are often combined to better investigate the spin-wave dynamics.

1.5. Magnonics

As introduced in Sec. 1.2.1, magnonics is an emerging research field in magnetism, where the spin waves are used to carry and process information. Spin waves, as the name suggests, naturally possess many wave-like properties. Experiments have demonstrated the reflection [64], refraction [65, 66], interference [67, 68] and diffraction [69, 70] of spin waves, which behave similarly to electromagnetic waves. Spin waves in finite-size magnetic structures can also form standing waves [96–98]. In addition to their wave-like nature, spin waves also behave as quasiparticles, whose quanta are referred to as magnons. Magnons are classified as bosons, due to the fact that when flipping a spin, the change of the spin quantum number is $\Delta S = 1$. Therefore, an ensemble of magnons can reach the Bose-Einstein condensate, which is a macroscopic quantum state. This novel phenomenon has been experimentally observed in the yttrium-iron garnets (YIG) system [99–102]. Apart from the wave-particle duality of spin waves, spin waves originate from many types of interactions on different length scales as introduced in Sec. 1.2.2, allowing for a number of ways to tune their dispersion relation. All these properties of spin waves can bring novel functionalities to magnonic devices, and hence have significantly boosted the research of magnonics.

Apart from its many advantages, magnonics also holds several drawbacks. The most prominent problem for spin waves is the damping, which limits their propagation length and duration. For this reason, the only materials suitable for applications is YIG, which has the smallest Gilbert damping parameter of the order of 10^{-5} [103, 104]. Therefore, searching for new low-damping materials and reducing the damping have become two significant topics in magnonic research [105–109]. Another drawback of magnonics is the associated different magnetic interactions. On the one hand, this offers more ways of tuning the spin waves but, on the other hand, it also limits the precision of controlling the spin waves. Therefore, when tuning the magnetic interactions for a specific system, a balance must be achieved.

To build a magnonic device, several functional building blocks are needed [22]. As shown in Fig. 1.8(a), a magnonic device consists of four building blocks, which are the input, output, control unit and the functional medium. The arrows in Fig. 1.8(a) indicate the direction of information flow. The input and output units are responsible for the generation and detection of spin waves. Many methods can be used to achieve these goals, which will be introduced in Sec. 1.4. The processing unit of a magnonic device consists of the control unit and the functional medium, where the spin waves are manipulated.

For an analog magnonic device, when spin waves propagate in the functional

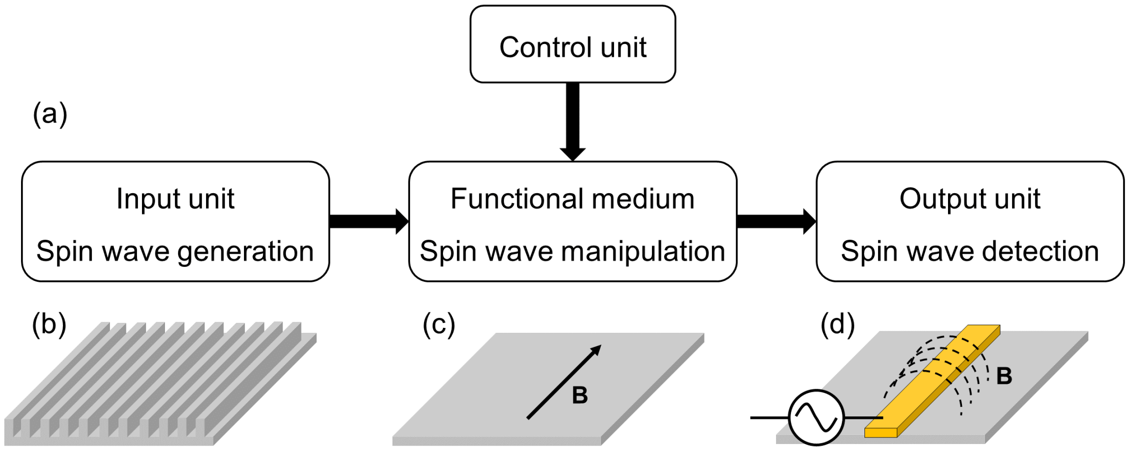

Figure 1.8. (a) Block diagram of the four components for a magnonic device. (b)-(c) Three common methods for manipulating the functional medium.

medium, their frequency, phase and amplitude can be modified via the control unit, which corresponds to certain operations of the processing unit. These operations are often realized by modifying the $\mathbf{H}_{\text{eff}}$ inside the functional medium, either globally or locally. To manipulate the functional medium, three methods are commonly used. The first method [Fig. 1.8(b)] is to pattern the magnetic materials into certain structures [110–112], which effectively modifies the $\mathbf{H}_{\text{demag}}$. The second method [Fig. 1.8(c)] is to apply a global uniform magnetic field [15], and the third method [Fig. 1.8(d)] is to apply a local magnetic field [16, 113]. For the second and third method, the magnetic field can be either static or dynamic. For the first method, the most well known example is the magnonic crystal, where magnetic materials are periodically modulated [28, 114]. One most prominent feature of the magnonic crystal is that, due to the translation symmetry, its spin-wave dispersion forms a band structure, which has allowed and forbidden bands [110]. The magnonic crystal can therefore be effectively used as a magnonic filter, which can filter out the spin waves with the frequencies in the forbidden band [115]. For the second method, by applying a global magnetic field, the dispersion relation of the functional medium can be effectively tuned. In this way, the whole functional medium can also be used as a phase shifter for the spin waves [116]. If a dynamic global field is applied, it is normally treated as quasi-static, and its physical influence is similar to that of a static field. Because the global external field is often generated by an electromagnet, its frequency is limited to a rather low value. For the third method, the local magnetic field is often operated in the high-frequency regime, i.e. the frequency of the local field is comparable with the spin-wave frequency. In this case, the functional medium can be operated as a frequency mixer or an amplifier [117]. Moreover, if the local fields are quasi-static and are arranged in a periodic fashion, the functional medium will be equivalent to a magnonic crystal that is reprogrammable.

Apart from the above analog functions, another route for magnonics is to build magnonic devices that are able to perform digital operations, i.e. the logic-gate operations which are the basic operations for contemporary computers [118]. The block diagram for the digital magnonic device is the same as that shown in Fig. 1.8. The difference is that the input/output signal can now only be 0 or 1. Naturally, the first task is to encode the spin waves into 0/1. In general, there are two methods. One is using the amplitude, and the other is using the phase. For the first method, the low-amplitude spin waves are often encoded as 0, and the high-amplitude spin waves as 1. One of the choices for the functional medium is to build it as a spin-wave interferometer, which is commonly referred to as a Mach-Zehnder-type spin-wave interferometer [15, 16]. The output from the interferometer, depending on whether there is destructive or constructive interference, is defined as 0 or 1. For the second method, the spin-wave phase 0 and π are often encoded as 0 and 1. Here, an effective way of shifting the phase between 0 and π is needed in order to perform the logic operations. For example, a spin-wave waveguide of the length $\lambda/2$ can be used to change the phase from 0 to π [119]. Currently, the most challenging aspects of magnonic logic devices are to build all-magnonic logic gates and enhance the conversion efficiency between the spin-wave and electrical signals.

To summarize, magnonics is a young research field that holds many promising aspects, such as no Joule heating and external field control. Nevertheless, there are many challenges in this field, such as reducing the damping of magnetic materials and precise control of magnetic interactions.

2. Experimental

In this chapter, we introduce the experimental techniques that are used in the thesis. In the first three sections, pump-probe experiments are explained. For these experiments, the pump of the measurement system is used to excite the dynamics, and the probe is used to detect the dynamics. More specifically, in Sec. 2.1, a general description for a pump-probe experiment setup is given. Following this, two different types of experimental realizations are introduced, which have different functions in terms of measuring the magnetization dynamics. In Sec. 2.4 the sample fabrication processes are described, with an emphasis on sample preparation using lithography techniques.

2.1. Pump-probe experiment

In general, any time-resolved observations of a physical process can be analyzed from the perspective of a pump-probe experiment. For example, a person throws a stone into water, and watches the water wave propagate. In this case, the pump is the falling stone that excites the water wave. The probe is simply the human eye, which monitors the water wave. The feasibility of this observation is guaranteed by the fact that our eyes can capture movements of both the stone and water wave at different times. After the images have been processed by our brain, we then have a movie in our mind of how this process occurs. Following this simple example, several important concepts for a pump-probe experiment can already be extracted. However, to observe the magnetization dynamics, more complex excitation and time-resolved detection schemes are needed.

The block diagram of our pump-probe setup is shown in Fig. 2.1. The system is divided into mainly three parts, in terms of their functionalities. The first part is the pump that is used to excite the dynamics. The second part is the probe that is used to measure a specific physical quantity to characterize the dynamics. For these two parts, several techniques that are commonly used for exciting and detecting magnetization dynamics are listed. The third part is the mechanism that facilitates the time-resolved measurement. This part involves three important elements, the time resolution of the setup, the synchronization between the pump and probe, and a variable time delay between the pump and probe.

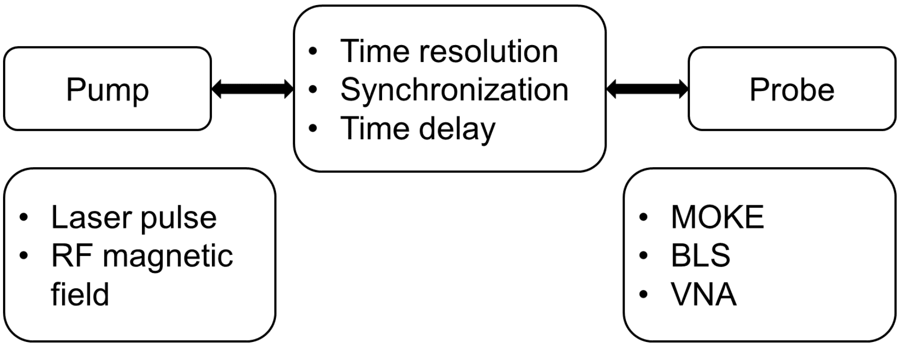

Figure 2.1. Diagram of the building blocks of a pump-probe setup. The abbreviations are RF: radio frequency, BLS: Brillouin light scattering and VNA: vector network analyzer.

Our pump-probe setup is based on an ultrafast fiber laser system, with a central wavelength $\lambda = 1030$ nm, pulse length ~ 50 fs and repetition rate of 200 kHz. Such an ultrafast laser pulse is used as the probe beam, and is sensitive to the out-of-plane component of the sample magnetization when using the polar MOKE geometry. To excite the magnetization dynamics in the sample, we can use either a laser pulse or an RF magnetic field. After determining the pump and probe, the next task is to determine the time resolution for the measurement system. For the case of an all-optical pump-probe setup, this time resolution is given by the convolution of the pump and probe pulses. Approximately, this value is given by the maximum pulse width of the pump or probe, which is $\sim 100 - 200$ fs for our setup. Following this, a synchronization must be achieved between the pump and probe. This is easily done for an all-optical system, since both pump and probe beams are from the same laser. After the synchronization, in the case of an all-optical system, by equalizing the lengths of both pump and probe paths, the time zero for the system can be found where the pump and probe beams arrive at the sample at the same time. By adjusting the path of the probe beam, the probe beam can arrive at the sample before or after pump beam, which subsequently can be used to measure the dynamics before and after the excitation. For the approach based on exciting the sample with RF magnetic field, a more complex synchronization mechanism is needed, which will be explained in Sec. 2.3.

The three building blocks shown in Fig. 2.1 are the most essential parts of a pump-probe setup. The realization of each block can be different depending on the goal for a specific measurement. In the next two sections, two types of setups are introduced. One is an all-optical pump-probe setup with TRMOKE, and the other one is a time-resolved scanning Kerr microscope.

2.2. All-optical pump-probe experiment with TRMOKE

As its name suggests, in an all-optical pump-probe experiment, optical light is used as both pump and probe beams. As shown in Fig. 2.2, the laser light, after being reflected by a mirror (M1), is divided by a 90:10 beam splitter (BS1) into two optical paths. The higher intensity part of the laser light is guided to an optical lens (L1) and focused onto a BaB_2O_4 (BBO) nonlinear crystal, which generates the second harmonic light with λ = 515 nm, and pulse width around 100 fs. The second harmonic light is used as the pump beam for the system, and the other path with the fundamental wavelength is for the probe beam. The second harmonic light is chosen as the probe beam in order to avoid inference effects between the pump and probe beams. After a series of mirrors and attenuators, the pump beam arrives at the optical chopper. The optical chopper is made of several metal blades, which can block the beam intermittently while it is rotating. The chopper is used to modulate the pump beam, which is used for the lock-in detection.

The probe beam is guided through a series of mirrors to a variable optical delay stage, composed of a retroreflector mounted on a motorized translation stage. By moving the retroreflector, a variable time delay between the pump and probe beams can be created. The zero delay is defined as the position for the retroreflector, where

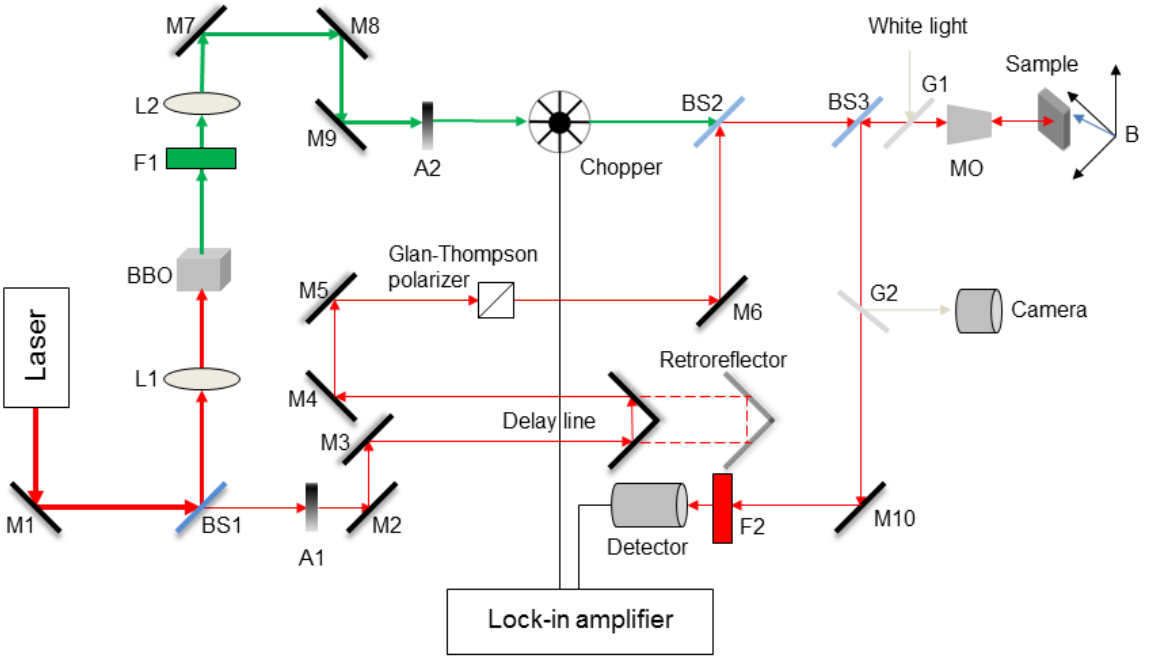
M7
M8
White light
Sample
G1
L2
BS2
BS3
B
M9
A2
Chopper
MO
F1
Glan-Thompson polarizer
BBO
M5
M6
G2
Camera
Laser
Retroreflector
L1
M4
Delay line
M3
M1
BS1
A1
M2
Detector
F2
M10
Lock-in amplifier

Figure 2.2. All-optical pump-probe setup with TRMOKE. A: attenuator, BS: beamsplitter, F: optical filter, G: glass plate, L: optical lens, M: mirror, MO: microscope objective.

the pump and probe beams arrive at the sample at the same time.

Before combining the two optical paths, the probe beam is passed through a Glan-Thompson polarizer to remove the unwanted polarization after passing all the optical components. The two beams are subsequently combined by a beam combiner (BS2) and focused onto the sample with a microscope objective, with the beam size being about 10 um in diameter. The back-reflected beam passes through the infrared bandpass filter (F2), where the pump beam component is removed, and is guided to the detector. Another imaging path is introduced via two glass plates G1 and G2 towards a CCD camera. In this case, a white light source is used in order to obtain an image of the sample. This imaging function is used when the laser beams need to be guided to a specific part of the sample.

The detector used in this setup is an optical bridge detector. As depicted in Fig. 2.3, when the beam enters the detector, it first passes a half-wave plate, and then is guided to a Wollaston prism. The Wollaston prism is used to split the beam into two parts of orthogonally linearly polarized light. These two parts of light are detected by two photodiodes, giving the two intensities A and B. The Kerr rotation is given by the measured signal $A - B$, and the reflectivity is given by the signal $A + B$. During the experiment, two output channels A and B are constantly monitored using an oscilloscope. To maximize the sensitivity for the MOKE signal, prior to the measurement, A and B are adjusted to zero by rotating the half-wave plate [see Fig. 2.3]. The other two output channels, $A - B$ and $A + B$, are used for exporting the data of the measurement, i.e., $A - B$ for the Kerr rotation and $A + B$ for the reflectivity.

Since the measured signal is proportional to the out-of-plane component of the magnetization, in most cases this requires the sensitivity to detect very small Kerr rotations. In order to improve the signal-to-noise ratio, a lock-in amplifier is used to extract the signal. In the following, we explain the three important signals for

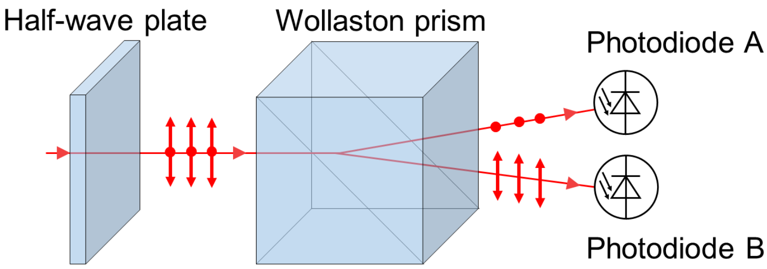

Figure 2.3. Schematic of the working principle of the optical bridge detector.

the lock-in detection, which are,

$$\begin{aligned} S_{\mathrm{ref}} &= A_{\mathrm{ref}} \sin(2\pi f t + \phi), && (2.1a) \\ L_{\mathrm{pump}} &= L^{0}_{pump}(t) \cdot R(t), && (2.1b) \\ L_{\mathrm{probe}} &= L^{0}_{probe}(t) + \delta L_{\mathrm{probe}}(t), && (2.1c) \end{aligned}$$

First, as required by the lock-in detection, the signal must to be modulated by a reference signal. In this case, the reference signal S_{ref} with f close to 1 kHz, is generated by the lock-in amplifier internally. The reference signal is then used to drive the optical chopper which modulates the pump light. More specifically, as shown in Eq. (2.1b), the original pump light $L^{0}_{pump}(t)$, which is a sequence of 200 kHz pulses, is modulated by $R(t)$ that is approximately a square wave with a frequency f. When the probe beam is moved to a position after the zero delay, meaning that it is probing at a time after the excitation, another component in the probe beam is generated, i.e., $\delta L_{\mathrm{probe}}(t)$ in Eq. (2.1c) that has a frequency f. This component is a result of the excitation from the pump beam. When measuring $A - B$, this is the change of Kerr rotation, and when measuring $A + B$ this is the change of reflectivity. Because these signals are oscillating at the same frequency as the reference signal, both their amplitude and phase values can be extracted from the lock-in amplifier.

Since it is an all-optical system, the quality of the measurement strongly depends on alignments of both the beam path and optical components. The alignment of the setup involves mainly three steps.

- Alignment of the pump and probe beams before the sample:
  All the mirrors before the sample are used to align the beam path as depicted in Fig. 2.2. This is to obtain a collinear configuration of the pump and probe beams when incident on the sample, which can maximize the overlap between the two beams, and hence improve the signal quality.
- Alignment of the microscope objective:
  This aligns the main axis of the microscope objective with respect to the pump/probe beam path. Therefore, more light can enter and reflect back through the microscope objective.
- Alignment of the probe after the sample and detector:
  This is to guide to beam to the detector, and align the two split beam spots onto the two photodiodes.

Using this setup, the evolution of both the Kerr rotation and reflectivity can be traced from femtoseconds to nanoseconds. For our purpose, the time window that is often investigated is from tens of picoseconds to one nanosecond, where the magnetization precesses and slowly returns to its equilibrium position. A typical measurement data is shown in Fig. 2.4, which is a systematic characterization of the precessional dynamics of the magnetization in a 7.5 nm CoFeB film with an applied in-plane magnetic field range of 114 – 295 mT. The Kerr rotation data is often taken

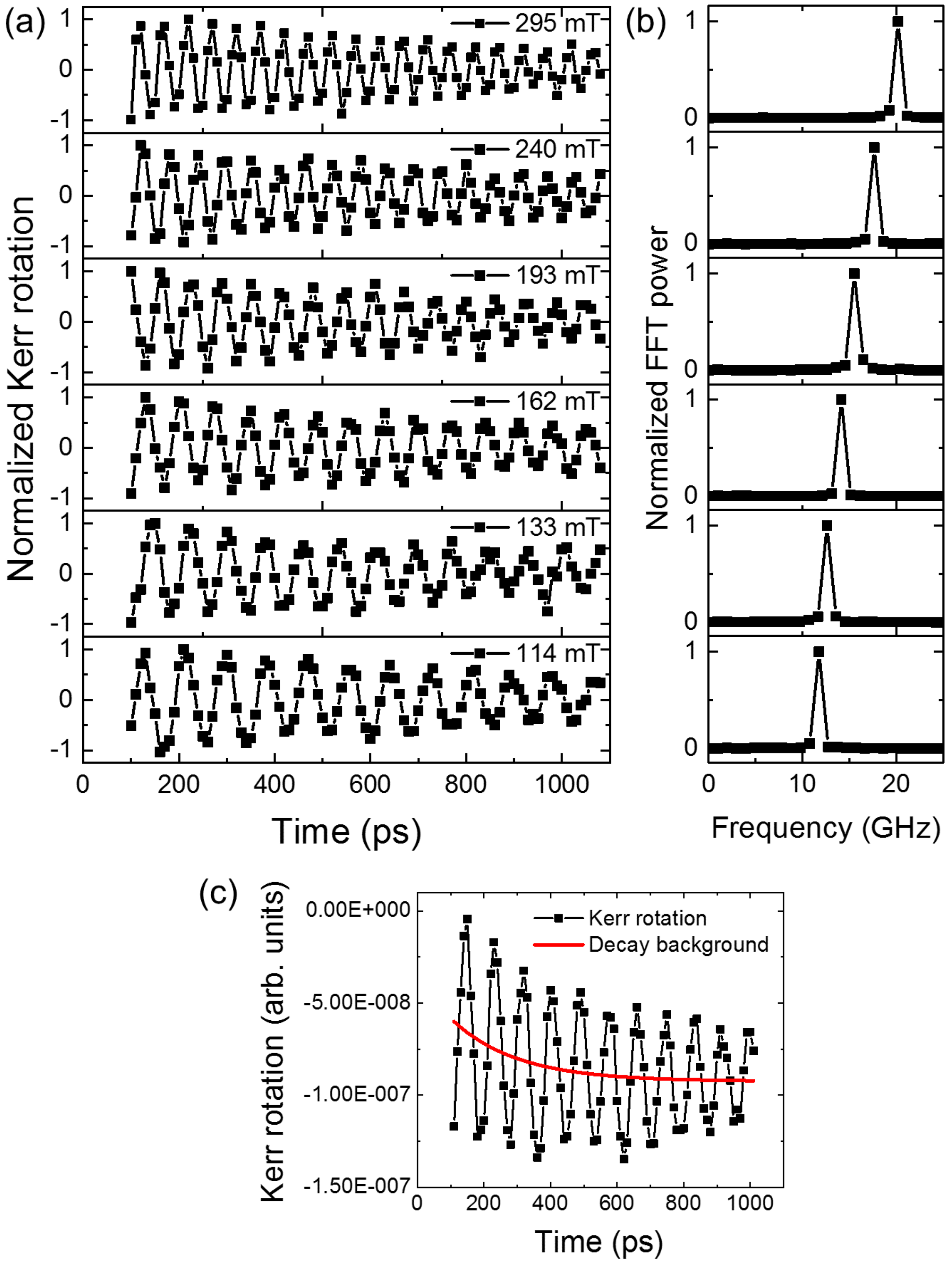

Figure 2.4. Precessional dynamics of a CoFeB film measured from the all-optical setup with TRMOKE. (a) Normalized time-resolved Kerr rotation. (b) Normalized FFT power spectrum. (c) Raw data at 114 mT, with the red line indicating the decay background.

after 100 ps, which is after the ultrafast demagnetization and remagnetization process. The decay background [see Fig. 2.4(c)] is subsequently subtracted to get the precession data, as shown in Fig. 2.4(a). A fast Fourier transform (FFT) is of the precession data is often performed, in order to obtain a frequency spectrum [see Fig. 2.4(b)]. From the data in Fig. 2.4(b), a blue shift of the precession frequency can be clearly observed when increasing the applied field. This blue shift is in good agreement with the field dependence of an in-plane magnetized thin film, which is

$$f = \frac{|\gamma|\mu_0}{2\pi}\sqrt{H_{\text{ext}}(H_{\text{ext}} + M_{\text{S}})}. \tag{2.2}$$

2.3. Time-resolved scanning Kerr Microscopy (TRSKM)

With our all-optical setup, the precession and damping of the magnetization can be measured in real time. However, the collinear configuration of the pump and probe beams brings certain limitations to the setup i.e., the dynamics that the probe beam measures is approximately a uniform precession. This limitation excludes the possibility of using this setup to study propagating spin waves, which are important topics for magnonics research. In addition, the position of the probe beam on the sample with respect to the pump beam is fixed, and hence excludes the possibility of performing scanning microscopy, resulting in the loss of the spatial information for the magnetization dynamics. To overcome these two limitations, modifications of the all-optical setup up are introduced to give a time-resolved scanning Kerr microscope.

2.3.1. Setup description

To build a time-resolved scanning Kerr microscope, the optical excitation is replaced by a continuous RF magnetic excitation that is produced by an RF current in an electrical transmission line and can excite propagating spin waves. The magnetization dynamics is probed in a similar fashion to the method described earlier.

In order to perform the pump-probe measurement, the excitation provided by the RF magnetic field and the optical probe pulses must be synchronized. Since the RF excitation is not a pulsed signal, in this case the synchronization must be defined in terms of the phase of the RF excitation. As shown in Fig. 2.5(a), for an RF signal with 4 GHz, $t = 0.0$ ns is defined, where the corresponding phase is zero. The synchronization is achieved under the condition that, if any optical pulse arrives at a phase ϕ_0, the next pulse will arrive at a phase of $\phi_0 + 2n\pi$, where n is an integer. For example, in the inset, the two signals (red solid lines) are synchronized at $\phi_0 = 4/5\pi$.

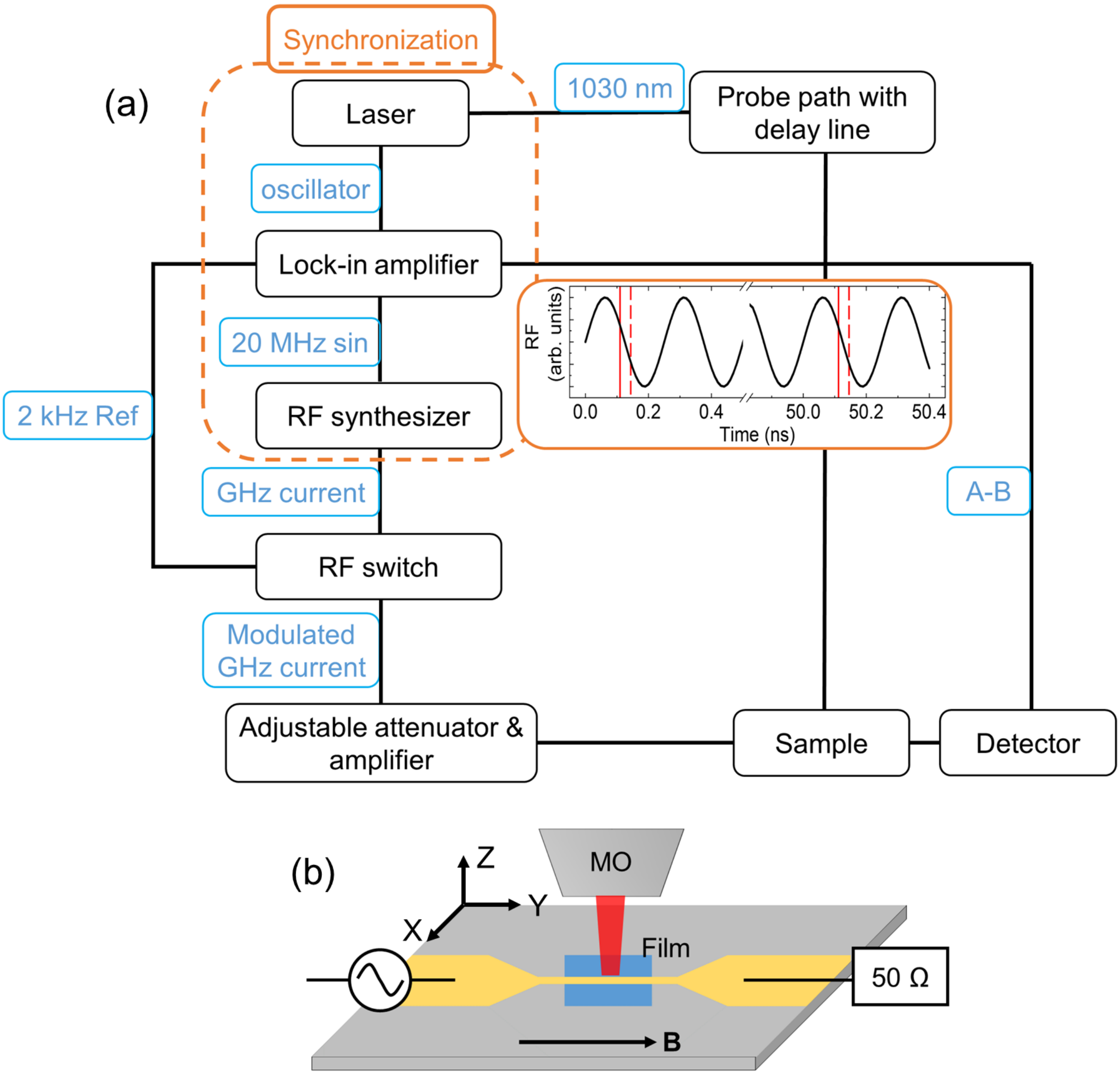
(a)
Synchronization
Laser
1030 nm
Probe path with delay line
oscillator
Lock-in amplifier
20 MHz sin
RF synthesizer
2 kHz Ref
RF
(arb. units)
0.0
0.2
0.4
50.0
50.2
50.4
Time (ns)
GHz current
A-B
RF switch
Modulated GHz current
Adjustable attenuator & amplifier
Sample
Detector
(b)
Z
Y
X
MO
Film
50 Ω
B

Figure 2.5. Schematic of the TRSKM setup. (a) Diagram of the signal connections between different components. The black boxes denote the optical devices, electrical devices and the sample. The blue boxes denote the optical or electric signals. The synchronization module is marked with the orange dashed box, with an inset demonstrating the synchronization between the RF (the sinusoidal wave) and laser (red lines) signals. The red dashed lines indicate the new phase that the signal is locked to, when the original signal (red solid lines) is delayed. (b) Schematics of the setup at the sample with a magnetic film under the signal transmission line.

The synchronization module is marked by the dashed square in Fig. 2.5(a), and in order to achieve the synchronization, the laser oscillator signal that is a 20 MHz pulsed signal is first transformed into a 20 MHz sinusoidal signal by the lock-in amplifier. The transformed 20 MHz signal is subsequently used as the reference frequency signal of the RF synthesizer. The output of the RF synthesizer is an RF current in the GHz range, whose phase is related to the 20 MHz reference signal. Using this scheme, the pulse signal of the laser oscillator is locked at a specific phase of the GHz current. The optical laser pulse driven by the oscillator signal is then inherently locked with the GHz current. An experimental verification of the synchronization is shown in Fig. A.1. Once the synchronization is achieved, it is relatively easy to change the phase that the optical pulse is locked to. In this case, the optical delay line of the probe is used, which can delay or advance the arrival of the probe beam, and hence the optical pulse can be locked to a larger or smaller phase. For example, in the inset in Fig. 2.5(a), when the original optical signal (red solid lines) is delayed, the new signal (red dashed lines) is locked to a larger phase.

The generated RF current first passes through an RF switch, which is driven by the 2 kHz reference signal sent by the lock-in amplifier. As a result, the RF current is modulated by the RF switch, similar to the modulated pump beam in the all-optical setup, and hence makes lock-in detection feasible. The modulated RF current subsequently passes through a series of adjustable attenuators and amplifiers, to be able to generate the required Oersted field to excite spin waves. To guide the RF current to the transmission line of the sample, the amplified current is connected to one end of the transmission line of a customized printed circuit board (PCB), whose other end is connected to the left contact pad of the signal transmission line of the sample shown in Fig. 2.5(b). The right contact pad on the sample is connected to another transmission line of the PCB, with its other end connected to a 50 Ω terminator. When the RF current passes through the signal line, the generated RF Oersted field around the current line excites the spin wave with the same frequency.

The detection scheme of the TRSKM setup is similar to that of the all-optical setup. The probe beam is focused using a long working distance microscope objective with a numerical aperture of 0.55, which gives probe beam size of 1.1 μm [see detailed characterization in Fig. A.2]. The back reflected beam is guided to an optical bridge detector, and the MOKE signal is extracted with the lock-in amplifier. Furthermore, in order to function as a scanning microscope, the PCB containing the sample is fixed onto a 3D piezo stage, which can scan the sample while the probe beam is fixed.

2.3.2. Measurement protocol

The most prominent difference between the TRSKM and our all-optical setup is that its excitation is from a continuous RF current. In order to excite the spin wave,

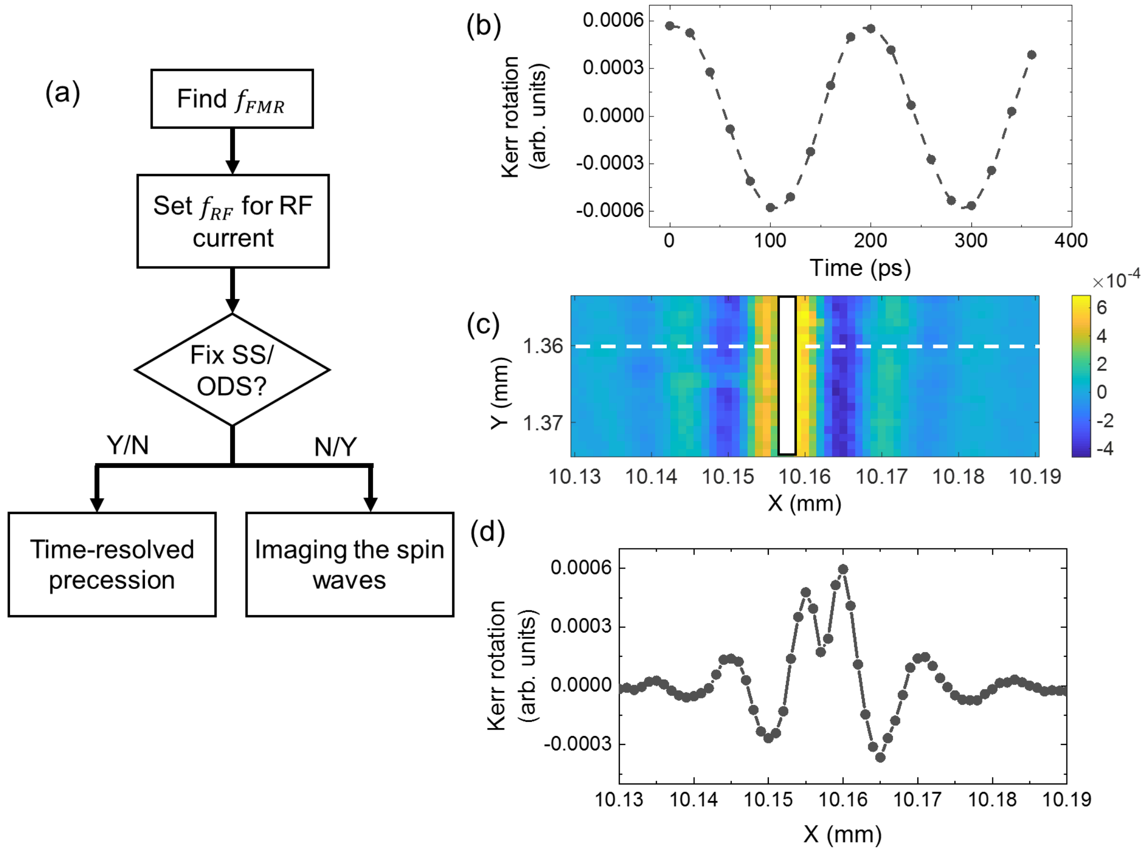

Figure 2.6. TRSKM measurement protocol and typical data. (a) Flowchart of the steps to perform a TRSKM measurement. Here, SS stands for sample stage, ODS for optical delay stage and Y/N for Yes/No. (b) Time-resolved Kerr rotation with the RF excitation of a CoFeB film at 5.25 GHz. (c) Image of the propagating spin wave on both sides of the transmission line, at f_{RF} = 4.50 GHz. The transmission line (white bar) is along the Y direction, located at X = 10.157 mm, and the external bias field is applied along the Y direction. (d) Line profile of the scanned Kerr rotations in (c) at Y = 1.360 mm.

the frequency of the spin wave must be equal to the RF current, f_{RF}. Therefore, prior to the measurement, some preliminary characterization is needed in order to determine a suitable value for the RF frequency. To explain the measurement protocol [see Fig. 2.6(a)], we used an example of measuring propagating spin waves in a 10-nm thick CoFeB film.

As shown in Fig. 2.6(a), the first step of the TRSKM measurement is to find the FMR frequency f_{FMR} of the film. This is done by measuring the precession frequency using the all-optical setup with TRMOKE. In this case, f_{FMR} = 3.0 GHz is found. The second step is to set the frequency of the RF excitation f_{RF}. Since the bias field is along the Y direction [see Fig. 2.5(b)], the spin waves that propagate along the X direction should have a higher frequency than f_{FMR}, and hence $f_{RF} > f_{FMR}$.

Using TRSKM, two types of measurements can be performed [see Fig. 2.6(a)]. One is the measurement of a time-resolved precession, where the sample stage should be fixed, while the optical delay stage is moved to provide the time resolution. This measurement, in principle, does not provide any further information on spin-wave frequency. It is simply a reconfirmation that the f_{RF} is correctly chosen to be able to excite the precession. Such a measurement result is shown in Fig. 2.6(b). The other measurement is to image spin waves, where the optical delay is fixed, and the sample stage is moved to provide the spatial resolution. Typical data of such a measurement is shown in Fig. 2.6(c). From the data, it can be clearly observed that the spin waves are excited on both sides of the transmission line. Moreover, from the line profile at $Y = 1.360$ mm [Fig. 2.6(d)], it can be seen that the spin wave on the right hand side has a higher intensity. This is due to the mismatch between the spatial chirality of spin waves on the left hand side and the chirality of the RF magnetic field. Such phenomena is commonly referred to as the amplitude nonreciprocity for the Damon-Eschbach mode with such an excitation configuration [120].

2.3.3. Measurement of dispersion relation

To fully demonstrate the capability of the TRSKM setup, a series of scanning Kerr rotation measurements along the X direction with varying f_{RF} values are used to characterize the dispersion relation of propagating spin waves in a Damon-Eschbach geometry [see magnetic field direction in Fig. 2.5(b)]. These measurements are the special case of an imaging measurement, where the Y stage is fixed, and the Kerr rotation is recorded for each X coordinate. As shown in Fig. 2.7(a), the scanning Kerr rotation measurements are performed with varying the RF frequency from 4.5 to 6.5 GHz, in steps of 0.25 GHz. It can be seen that, with increasing f_{RF}, the wavelength of the spin wave decreases monotonically, which corresponds to the behavior of a Damon-Eschbach mode. To extract its corresponding wave vector, an FFT is performed, with the FFT peak indicating the value $1/\lambda$ and the corresponding wavevector $k = 2\pi/\lambda$ for each frequency [Fig.2.7(b)].

From the TRSKM measurements, a dispersion curve of the spin waves is obtained, with a wavevector range of $0.7 - 2.5$ rad/μm and a frequency range of $4.5 - 6.5$ GHz. At a first glance, the dispersion curve [Fig. 2.7(c)] does not look similar to the Damon-Eschbach mode (yellow curve) shown in Fig. 1.3(d). To explain this, we examine more carefully the terms in Eq. (1.30). The relation between w^2 and k is via an exponential factor e^{-2kd}, where d is the film thickness. In order to have a similar curve shape in Fig. 1.3(d), the value of kd needs to cover the value range from 0 to 1. However, for the experimental data in Fig. 2.7(c), the maximum value of kd is less than 3×10^{-3}, which is far below 1. Therefore, the experimental dispersion relation cannot exhibit a characteristic shape, as the one shown in Fig. 1.3(d). Indeed, since

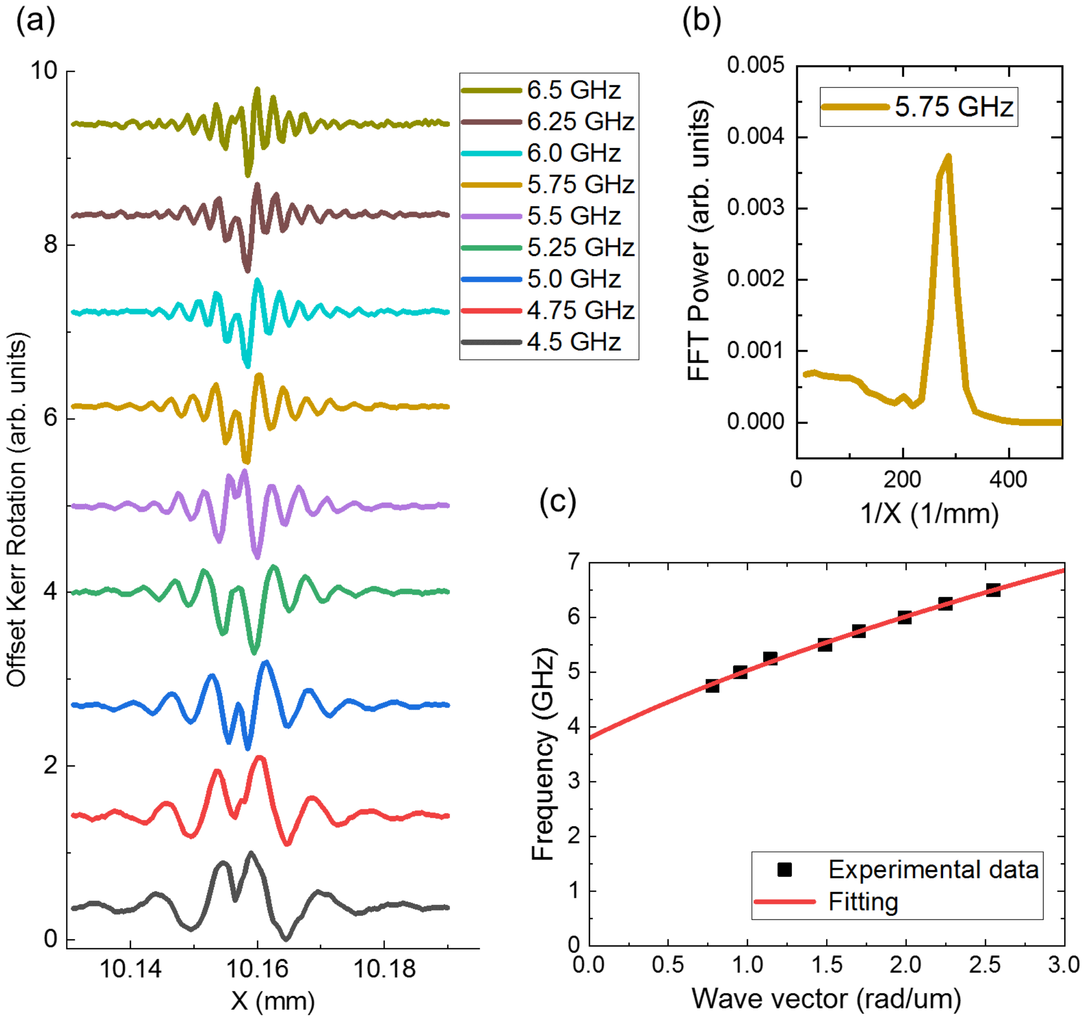

Figure 2.7. Characterization of the dispersion relation of the spin waves in a 10 nm-thick CoFeB film. (a) Scanning Kerr rotation measurements along the X direction for f_{RF} ranging from 4.5 to 6.5 GHz. The lines are shifted for clarity. (b) FFT power of the line scanning measurement at 5.75 GHz. (c) Dispersion relation of the measured Damon-Eshbach mode.

$kd << 1$, Eq. (1.30) can be approximated by the following,

$$\omega^2 = \omega_0(\omega_0 + \omega_{\mathrm{M}}) + \frac{\omega_{\mathrm{M}}^2}{2}kd, \tag{2.3}$$

which can then be rewritten as,

$$f = \frac{1}{2\pi}\sqrt{A + Bk}, \tag{2.4}$$

with $f = \omega/2\pi$, $A = \omega_0(\omega_0 + \omega_{\mathrm{M}})$ and $B = \omega_{\mathrm{M}}^2 d/2$. Therefore, in this k range, Eq. (2.4) is a good approximation for the dispersion relation. This equation can be used to fit the experimental data, which gives the value for the two fitting parameters. From the fitting result, the FMR frequency of the film can be extrapolated by setting $k = 0$, and is found to be approximately 3.8 GHz.

To summarize, from the TRSKM measurement, a part of the dispersion relation of the spin waves can be obtained. However, for this setup, there are certain limitations for detecting the propagating spin waves, which are the range of both the wave vector and frequency in the dispersion curve. This limitation brings the detectable dispersion range into the long-wavelength regime for thin films, where $kd << 1$. The limitations are mainly from two reasons. The first one is the spatial resolution. The wavelength of the probe beam is 1030 nm, which is focused using a microscope objective with numerical aperture of 0.55. The resulting size of the focused beam is around 1.1 μm, which sets the upper limit of the detectable spin wave to $k \sim 3.1$ rad/μm. On top of that, there is a spatial decay length for the propagation of spin wave, which can be observed in Fig. 2.7(a). This limits the setup to detect spin waves whose wavelength is more than 15 μm, which sets a lower limit for wavevector, $k \sim 0.4$ rad/μm. The second limitation is from the RF synthesizer, whose output range is from 1.5 to 6.7 GHz. Therefore, this setup is not able to excite spin waves with frequencies larger than 6.7 GHz. For future improvements, one could consider using 515 nm wavelength light as a probe, and using the second harmonic component of the RF synthesizer to excite spin waves with higher frequencies.

2.4. Sample fabrication

To illustrate the sample fabrication process, the steps for fabricating the CoFeB film sample for TRSKM measurements are explained. As depicted in Fig. 2.8, each unit of the sample has a microstrip transmission line on top of a CoFeB structure. These structures require three steps of lithography, namely the fabrication of the alignment marker, the CoFeB structure and the microstrip. The purpose of the alignment marker is to introduce a coordinate system for the whole sample, and

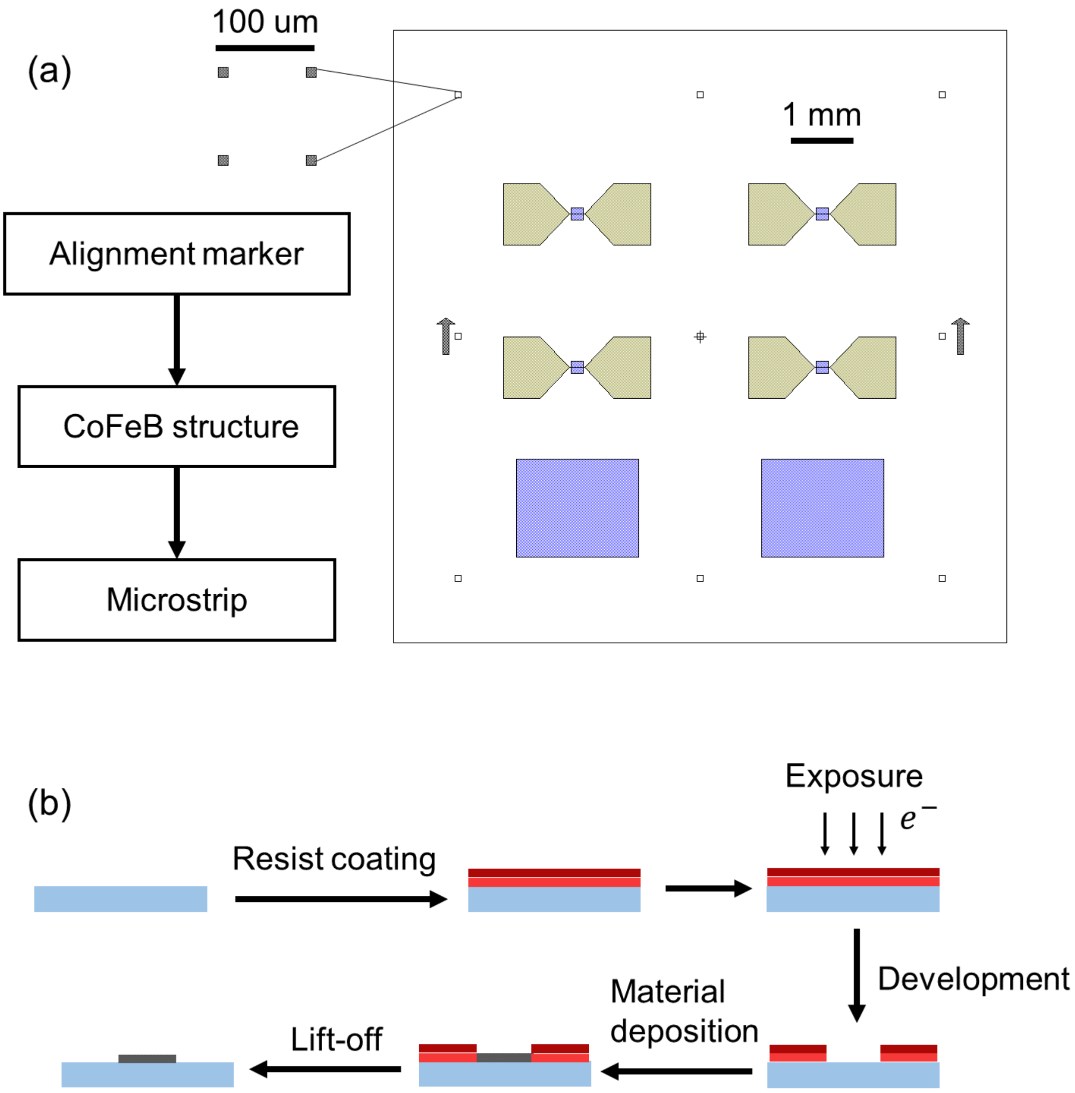
(a)
100 um
Alignment marker
CoFeB structure
Microstrip
1 mm
(b)
Exposure
e^-
Resist coating
Development
Material deposition
Lift-off

Figure 2.8. Electron beam lithography and fabrication steps of a CoFeB film sample for TRSKM measurement. (a) The schematics of the sample is shown on the right side. The blue part is the CoFeB film, the yellow part is the microstrip, and the closed box is the alignment marker array, with a zoom in of the top left markers. (b) Work flow of a typical e-beam lithography process. Color blue: substrate, red: resist layer, and black: deposited materials.

Table 2.9. Composition of the three components of the CoFeB film sample for TRSKM measurement

Sample component	Composition
Alignment marker	Cr(1.5 nm)/Au(20 nm)
CoFeB film	CoFeB(10 nm)/AlO_x(2 nm)
Microstrip	Cr(1.5 nm)/SiO_2(100 nm)/Cr(1.5 nm)/Cu(200 nm)/Cr(10 nm)

hence offers a precise control of the positions of the CoFeB film and microstrip relative to the marker.

The lithography method used in this thesis for all structures is electron-beam (e-beam) lithography. It contains five steps of processing, as shown in Fig. 2.8(b). The first step is to coat a resist layer on top of the substrate, which is usually a double layer of 4% Poly(methyl methacrylate) (PMMA) and 4% MMA (methyl methacrylate). For the spin coating, a spinning speed of 3000 rpm for one minute is used, which gives each coated PMMA and MMA layer of the thickness around $200 - 300$ nm. Afterwards, the sample is baked at 180° for five minutes.

The second step is the exposure, where the resist is exposed to a focused electron beam, with an e-beam dose of 680 μC/cm^2. The third step is the development, where the exposed part of the resist is removed by a mixture of Methyl isobutyl ketone (MIBK) and Isopropyl alcohol (IPA), with MIBK : IPA = 1 : 3. The fourth step is the material deposition. In this case, an AJA DC magnetron sputtering system is used for growing high quality CoFeB films, with a base pressure $\sim 1 - 2 \times 10^{-8}$ mbar. During the deposition, the sputtering power is set to 80 W, which gives a deposition rate for CoFeB $\sim$ 0.025 nm/s. For other materials, e-beam evaporation is used, with the system's base pressure $\sim 1 \times 10^{-6}$ mbar. The evaporation rate is controlled at the level $\sim$ 0.1 nm/s, in order to maintain a decent vacuum. The composition of each component of the sample is listed in Table. 2.9. For the microstrip, the first two Cr layers are for improving the adhesion, and the last Cr layer is for protection against oxidization. The SiO_2 layer is used to isolate the CoFeB from the RF current. For other samples, the composition specifications for each component are similar. The final step is the lift-off process where the residual resist is removed by acetone, and the sample is afterwards rinsed using IPA. After these five steps, only the parts where the resist was exposed to the e-beam will have the structures.

3. Magnetization dynamics in antiferromagnetically coupled ferromagnetic thin films

*Part of the work of this chapter has been published in Zhou et. al., Physical Review B **101**, 214434 (2020)* [121].

Magnetic trilayer films, in which two ferromagnetic (FM) layers can couple antiferromagnetically via a nonmagnetic (NM) spacer layer, led to the discovery of the giant magnetoresistance (GMR) effect [122, 123]. Since then, these systems have attracted significant attention due to their potential applications such as magnetic field sensors [124, 125] and magnetic random access memory [126]. These trilayer films are also referred to as synthetic antiferromagnets (SAF) [127], where the large tunability of the interlayer coupling in these systems has played an important role in many related research areas such as the motion of domain walls [128], solitons [129], skyrmions [130], and the use of synthetic antiferromagnets for flexible spintronics and biotechnology applications [131, 132]. The tunability of the trilayer films arises from the oscillatory nature of the Ruderman–Kittel–Kasuya–Yosida (RKKY) type interlayer exchange coupling (IEC) [29, 133], which means that not only an antiferromagnetic coupling, but also a ferromagnetic coupling can be achieved by tuning the thickness of the spacer layer [30, 31]. In addition, with an antiferromagnetic IEC, the precessional dynamics of the magnetization involves more modes, which is more complex than the one in a single FM layer [32, 134]. Accordingly, the spin-wave dispersion relations in these systems are also modified [135, 136], which are important for their potential applications in magnonics. For example, the antiferromagnetic IEC has been proposed to give a nonreciprocal spin-wave dispersion in the Damon-Eshbach geometry [33–35]. This nonreciprocity could be exploited to build nonreciprocal magnonic devices that function in a similar manner to isolators and circulators that are widely used in electronics or photonics [137–139].

Due to the presence of the IEC, the precessional dynamics of the trilayer films can be described as a coupled precession of the two FM layers. The coupled dynamics has two characteristic modes; the acoustic mode where the magnetization in the two layers precess in phase, and the optical mode where the magnetization in the two layers precess out of phase with a π difference [140]. Theoretically, one can describe the precessional dynamics using the formalism of statistical thermodynamics, as described by Liu *et al*. [32], or using the Landau-Lifshitz-Gilbert (LLG) equation [141]. Experimentally, one can measure the frequencies of both the acoustic and optical modes in the frequency and time domain using broadband FMR [32, 134, 140, 142, 143] and TRMOKE [144–147], respectively.

In the work described in this chapter, we exploit the competition between the Zeeman energy and the energy associated with the IEC to provide a comprehensive understanding of different precessional modes in the trilayer films. To do so, we measure the precessional dynamics of three samples with different IEC strengths in the same range of applied magnetic fields using the all-optical pump-probe technique with TRMOKE. In Sec. 3.1, the static magnetic properties of synthetic antiferromagnets are discussed. In Sec. 3.2, a systematic study of the precessional dynamics in synthetic antiferromagnets is presented. In Sec. 3.3, a trial experiment of using the time-resolved scanning Kerr microscope (TRSKM) setup to measure propagating spin waves in synthetic antiferromagnets is presented. Finally, in Sec. 3.4, we present the conclusions.

3.1. Static magnetic properties of synthetic antiferromagnets

For our study, a composition of Si(100)/$Co_{40}Fe_{40}B_{20}$/Ru/$Co_{40}Fe_{40}B_{20}$ is chosen for the trilayer films. The layer thicknesses for the trilayer samples are listed in Fig. 3.1(a), where t_2 is the thickness of the lower magnetic layer deposited on the substrate and t_1 is the thickness of the upper magnetic layer. Samples 1, 2 and 4 incorporate two FM layers with different thicknesses where $t_1 = 2t_2$, which are referred to as asymmetric samples. Sample 3 includes two FM layers with the same thickness, which is referred to as the symmetric sample. Going from Sample 1 to 4, the thickness of the Ru layer, t_{Ru} is varied to give a different IEC strength for the four samples. All samples were coated with a 2 nm Al layer to prevent oxidization. The naming of the sample sequence facilitates the discussion of the precessional dynamics of these samples in Sec. 3.2.

The magnetic properties of the four samples are characterized at room temperature with an MPMS3 Superconducting Quantum Interference Device - Vibrating Sample Magnetometer (SQUID-VSM). Their in-plane hysteresis loops are shown in Figs. 3.1(c) and (d). Because of the antiferromagnetic IEC, the magnetizations of the two FM layers prefer to align antiparallel, which leads to a reduction of the net magnetization at zero field compared with the saturation magnetization. With increasing the applied magnetic field, the magnetizations of the two FM layers start

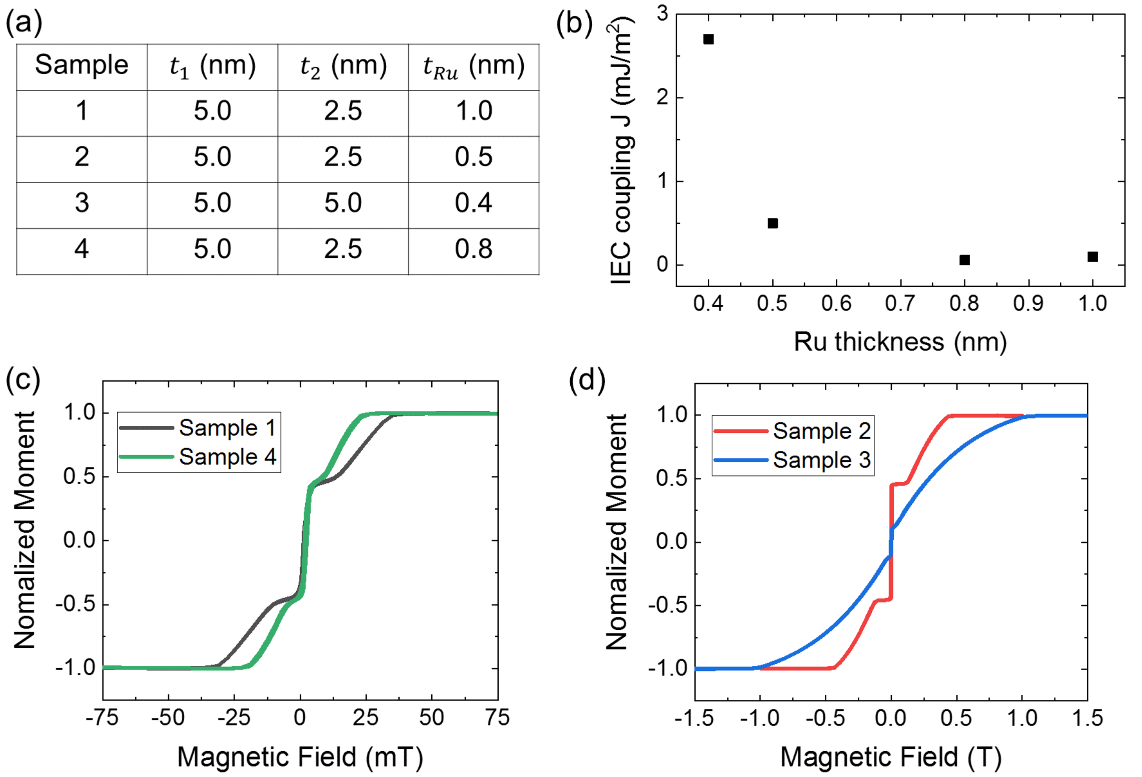

(a)

Sample	t_1 (nm)	t_2 (nm)	t_{Ru} (nm)
1	5.0	2.5	1.0
2	5.0	2.5	0.5
3	5.0	5.0	0.4
4	5.0	2.5	0.8

Figure 3.1. (a) Layer thicknesses for the four samples, where t_1, t_2 and t_{Ru} are the thickness of the upper magnetic layer, the lower magnetic layer next to the Si(100) substrate and the Ruthenium layer, respectively. (b) The IEC strength J as a function of the Ru thickness. (c) In-plane hysteresis loops for Sample 1 and 4 in a magnetic field range of -75 to +75 mT, and (d) Sample 2 and 3 in a magnetic field range of -1.5 to +1.5 T.

to align along the direction of the applied field, which results in a recovery of the net magnetization for all the samples.

To further extract information from the hysteresis loops, a simple model is built to describe such a synthetic antiferromagnet. For simplicity, we consider uniformly in-plane magnetized FM layers without easy axes with the following energy terms in per unit area,

$$E = E^{\text{IEC}} + \sum_{j=1,2} (E_j^{\text{Z}} + E_j^{\text{D}}), \tag{3.1}$$

where E^{IEC}, E^{Z} and E^{D} are the IEC, Zeeman and demagnetization energies, respectively. The dipolar interaction between the two layers is neglected. The detailed expressions for each of the terms are as follows,

$$E = J\frac{\mathbf{M}_1 \cdot \mathbf{M}_2}{|\mathbf{M}_1||\mathbf{M}_2|} - \sum_{j=1,2} \mu_0 t_j [\mathbf{H}^{\text{ext}} \cdot \mathbf{M}_j + \frac{1}{2}(\mathbf{M}_j \cdot \hat{z})^2]. \tag{3.2}$$

According to the schematic of the magnetizations in trilayer films shown in Fig. 3.2,

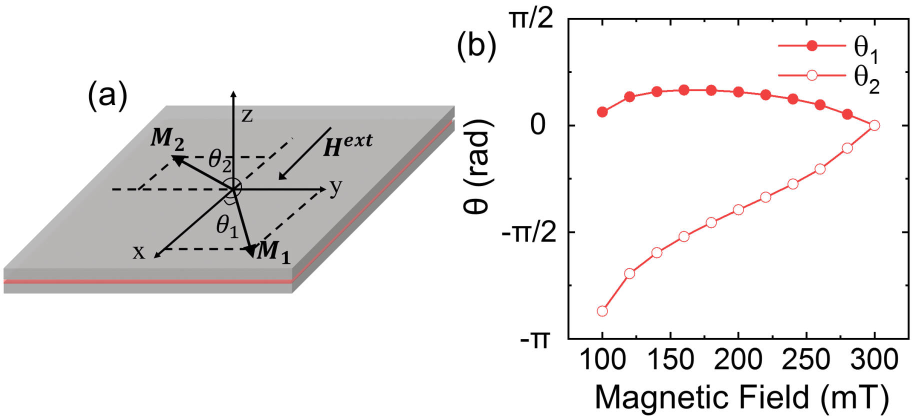

Figure 3.2. (a) Schematic of the magnetization configuration of the trilayer film and the coordinate system. (b) Magnetization orientation in the two layers, θ_1 and θ_2, of Sample 2 as a function of the applied magnetic field.

$\mathbf{M}_1$ and $\mathbf{M}_2$ (or $\mathbf{M}_j$, where $j = 1, 2$) are the magnetization of the upper and lower FM layers, both of which have in-plane magnetization with a saturation value of M. $\mathbf{H}^{\text{ext}}$ is also in-plane, with the absolute value of H. The antiferromagnetic IEC is quantified by the exchange constant J, with $J > 0$. t_j is the thickness of each FM layer, μ_0 is the vacuum permeability, and $\hat{z}$ is the unit vector along the z axis. In this model, we neglect the dipole-dipole interaction between the two FM layers, since we consider the magnetization dynamics inside each FM layer to be uniform. To determine the static magnetization configuration, the total energy given in Eq. (3.2) is minimized with respect to the orientation of $\mathbf{M}_1$ and $\mathbf{M}_2$. As illustrated in Fig. 3.2, the static magnetization configuration is described by the angles θ_1 and θ_2, which are between the x axis and $\mathbf{M}_1$ and $\mathbf{M}_2$, respectively.

For the symmetric sample ($t_1 = t_2 = t$), the following analytic expression of the static magnetization configuration can be obtained, given that $\theta_1 = -\theta_2 = \theta$,

$$\cos\theta = \frac{\mu_0 H M t}{2J}. \tag{3.3}$$

From this equation, it is straightforward to extract the value of J using the following expression,

$$J = \frac{1}{2}\mu_0 H^{\text{sat}} M t, \tag{3.4}$$

where H^{sat} is the minimum field needed to align the two layer magnetizations parallel to each other. For the asymmetric sample ($t_1 = 2t_2 = 2t$), only numerical values of θ_1 and θ_2 can be obtained. In this case, the numerical results for Sample 2 are shown in Fig. 3.2(b). To estimate J , we adjust its value until the theoretically calculated hysteresis loop matches the experimental one.

With the help of the theoretical model, two important pieces of information can be obtained from the hysteresis loops. The first is the strength of the IEC, which is shown in Fig. 3.1(b) for each sample. On increasing the thickness of the Ru layer from 0.4 to 0.8 nm, the strength of the IEC continuously decreases. On further increase to 1.0 nm, the value of J starts to increase again, indicating the start of the second period of oscillation of the RKKY coupling. The second piece of information is the significant differences between asymmetric and symmetric samples in terms of their magnetization reversal. For asymmetric samples, since the thicknesses of the two FM layers are different, there is a net magnetization close to the zero magnetic field. For symmetric samples, since the two layer thicknesses are the same, there is no net magnetization close to the zero field. Moreover, this asymmetry of layer thickness will further influence the Zeeman energy in each layer, as shown in Eq. (3.2). This allows, for the asymmetric samples, the antiparallel alignment of the two layer magnetizations to remain unchanged for a given range of the applied field, which is represented by the plateaus in the hysteresis loops close to the zero field. In contrast, the static magnetization configuration for the symmetric sample is immediately altered when applying the external field.

To summarize, the strength of IEC can be effectively tuned by changing the thickness of the Ru layer, as exhibited by the four samples. In addition, the hysteresis loop for each sample strongly depends on whether the sample is symmetric or asymmetric in terms of the thicknesses of the two FM layers.

3.2. Ultrafast laser induced precessional dynamics

3.2.1. Experimental data and analysis

To investigate the precessional dynamics in synthetic antiferromagnets, we use the all-optical pump-probe technique with TRMOKE. The samples investigated are Samples 1, 2 and 3, since Samples 1 and 4 are similar. During the experiment, two physical quantities are recorded, namely the reflectivity and Kerr rotation. Shown in Fig. 3.3 is the data for Sample 2 at an applied magnetic field of 150 mT. When the pump and probe pulses impinge on the sample simultaneously, a significant change of the reflectivity is observed, followed by an exponential decay [see Fig. 3.3(a)]. From the Kerr rotation measurement, a damped sinusoidal oscillation is observed, which corresponds to a damped precessional motion of the magnetization. To analyze this precession, the data after 100 ps is used after subtracting its decaying background, as shown in Fig. 3.3(c). An FFT is first performed, from which the number of modes and their frequencies can be extracted. In this case, the two extracted frequencies are 7.1 and 15.6 GHz, indicated by the red arrows in Fig. 3.3(d). Subsequently, the precession data is fitted with a two-component damped sine wave function which is

$$\sum_{i=1,2} A_i e^{-\frac{t}{\tau_i}} \sin(2\pi f_i(t - t_i)), \tag{3.5}$$

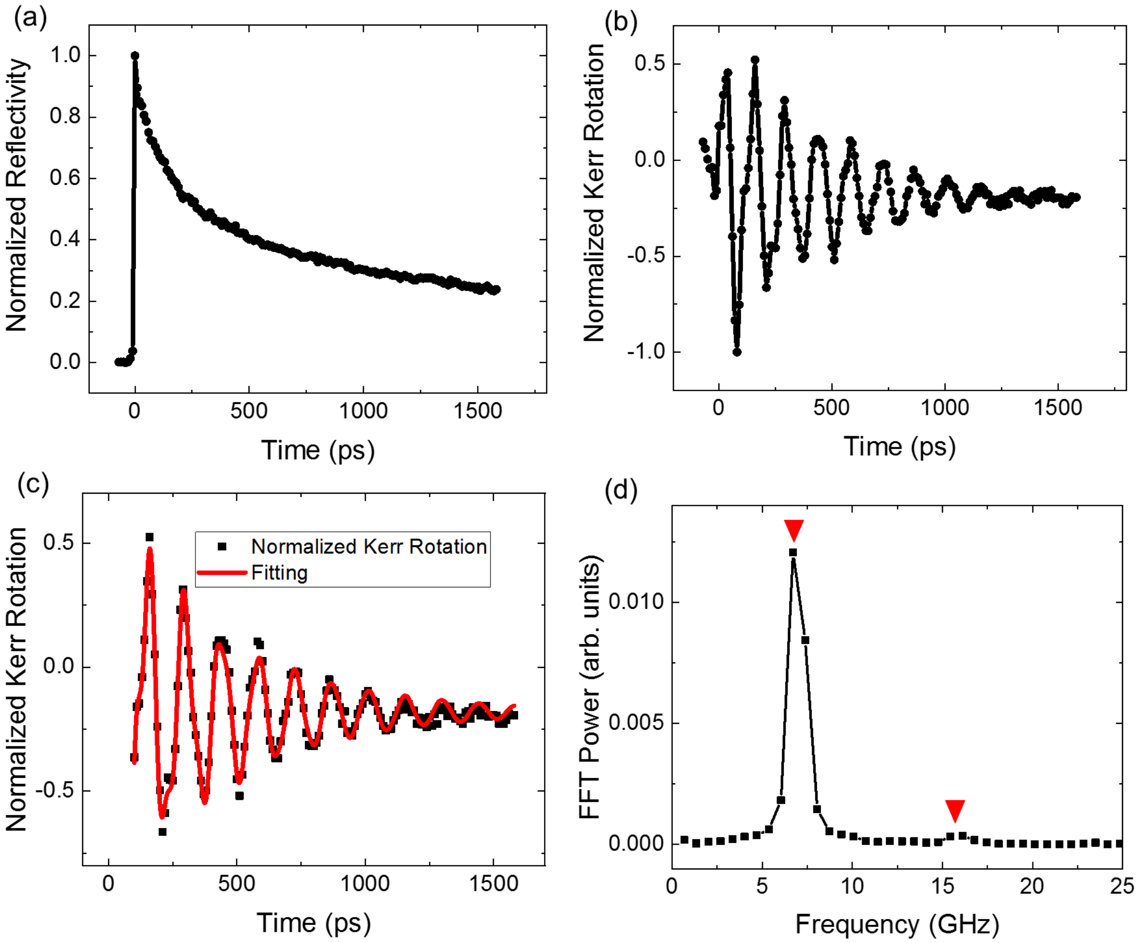

Figure 3.3. Normalized time-resolved (a) reflectivity and (b) Kerr rotation data of Sample 2 measured at a magnetic field of 150 mT. Lines are guided for the eyes. (c) Background subtracted data from (b) after 100 ps. Data is fitted with a two-component damped sine wave function. (d) FFT Power of (c), with the two modes indicated by the two red markers.

where A_i, τ_i, f_i, and t_i are the amplitude, time constant, frequency and initial time for the corresponding mode. From the fitting, the time constants τ_i for the lower and higher frequency modes are extracted, which are 482 and 253 ps, respectively.

A systematic characterization of the precessional dynamics for each sample is performed, by applying the external magnetic field with an in-plane component from 100 to 300 mT. For Samples 1 and 2, the laser excitation fluence is 10.0 mJ/cm^2, and for Sample 3, it is 13.4 mJ/cm^2. Their frequency dependence on the applied magnetic field is shown in Fig. 3.4. At a first glance, their behaviors are rather different. For Sample 1, two modes are always present at any applied magnetic field. For Sample 2, three modes are present from 100 to 175 mT. With increasing the field to 200 mT, the number of modes reduces to two, and further reduces to

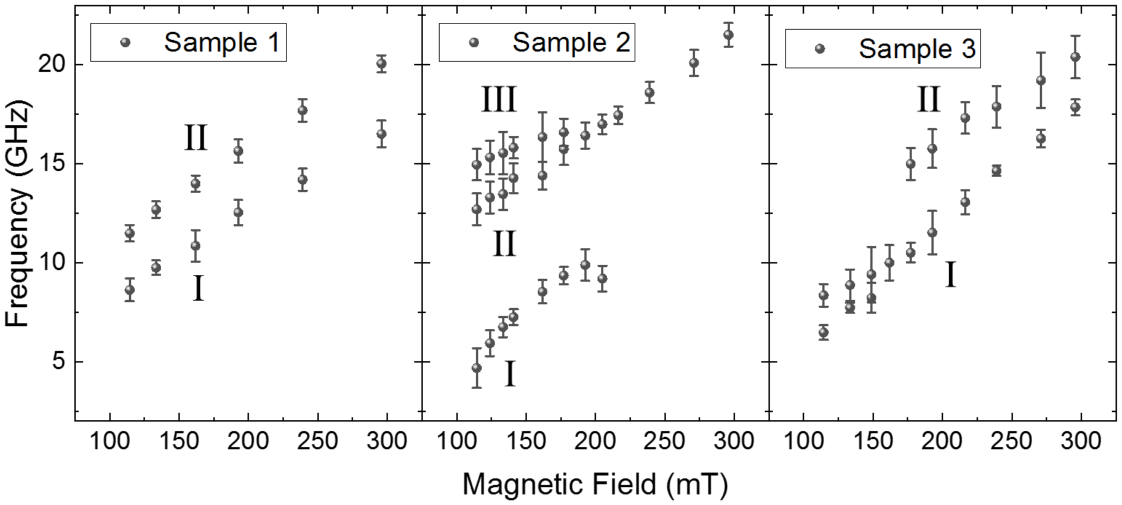

Figure 3.4. Frequency dependence on the applied magnetic field for the different modes. The different precessional modes are indicated with Roman numbers.

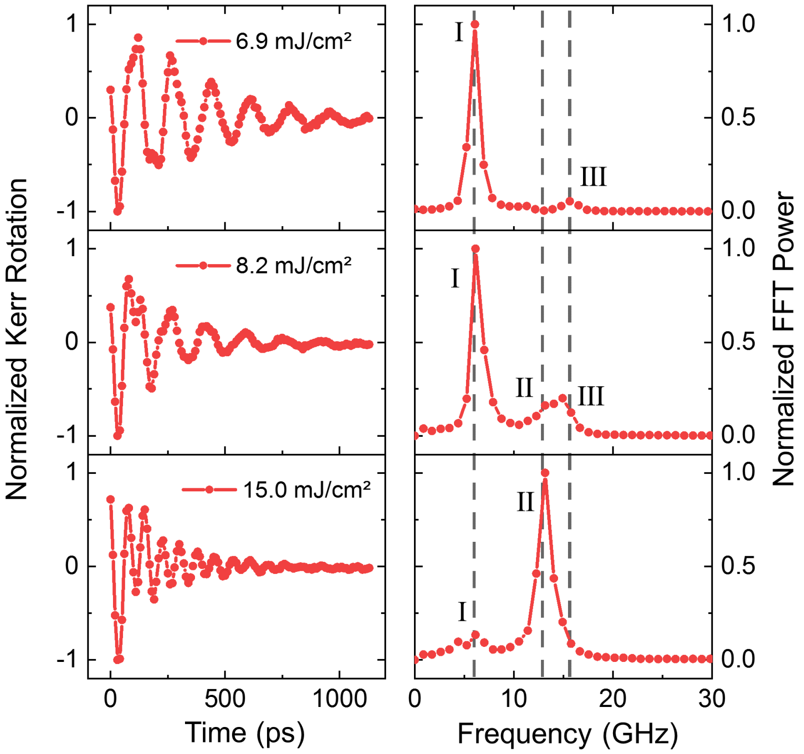

Figure 3.5. Evolution of the precessional modes in Sample 2 with increasing the fluence of the pump laser beam. Time-resolved Kerr rotation and the corresponding frequency spectrum are shown in the left and right column respectively for Sample 2 at $\mu_0 H$ = 130 mT. Lines connecting the data points are guides to the eye. Dashed black lines are positioned at the three observed modes.

one with further increasing the field value. For Sample 3, from 100 to 150 mT, there are two modes present. From 175 to 300 mT, there are also two modes present, but with larger frequency differences. The two main reasons for these different dynamics shown in these samples are differences of both the IEC strength and the FM layer symmetry, which will be quantitatively explained after introducing the theoretical model for calculating the precessional dynamics.

A rather interesting point in Fig. 3.4 is that, for Sample 2, in the field range of 100 to 175 mT, there are three modes. However, as previously mentioned, in this synthetic antiferromagnet, there are only two characteristic modes, which are the acoustic and optical modes. To understand the origin of the extra mode, we trace the evolution of each mode with changing the fluence of the pump beam, as shown in Fig. 3.5. It is observed that only mode I and III are present at a relatively low fluence, whereas mode II starts to appear when the fluence is increased to 8.2 $\mathrm{mJ/cm^2}$. From this information, we can deduce that mode I and III are the two characteristic modes, and mode II is an emergent mode that is related to the high pump fluence.

To summarize, the frequency dependence of different precessional modes on the applied magnetic field for the three samples are rather different. Moreover, an extra mode that belongs to neither the acoustic nor optical mode is observed, which is related to a relatively high fluence of the pump laser. In the next part, theoretical calculations for determining the precessional dynamics are presented, whose results will be compared with the experimental data, so that the origin of each mode can be identified.

3.2.2. Theoretical model for precessional dynamics

To determine the precessional dynamics, we consider the differential equations involving the two FM layers based on the precession part of the LLG equation,

$$\frac{\mathrm{d}\mathbf{M}_j}{\mathrm{d}t} = -|\gamma|\mu_0\mathbf{M}_j \times \mathbf{H}_j^{\mathrm{eff}}, \tag{3.6}$$

where $j = 1, 2$ indicating the top and bottom FM layer, and $\mathbf{H}^{\mathrm{eff}}$ is the total effective magnetic field that drives the magnetization precession. Following the procedure summarized in Fig. 3.6, the effective field for each FM layer is obtained by differentiating the energy density with respect to the layer magnetization. To solve the differential equations, the ansatz, which contains the static part $\mathbf{M}_j^{\mathrm{S}}$ and dynamic part $\mathbf{m}_j e^{i\omega t}$, is used. The static magnetization configuration, in this case, can be deduced by the energy minimization of Eq. (3.2). The differential equations can be solved analytically if an analytic expression for the static magnetization configuration can be obtained. In this case, the explicit form of $\mathbf{m}$ can be obtained. In the following, the final expression for the precession frequency f is expressed in units of Hz. A detailed calculation for asymmetric samples is presented in Sec. A.2.

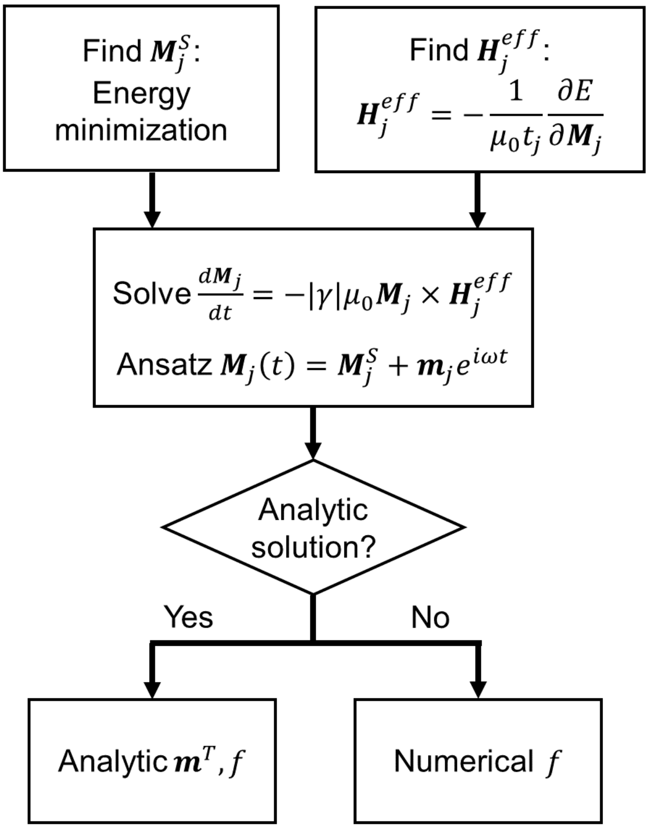
Find $\boldsymbol{M}_j^S$: Energy minimization
Find $\boldsymbol{H}_j^{eff}$: $\boldsymbol{H}_j^{eff} = -\frac{1}{\mu_0 t_j}\frac{\partial E}{\partial \boldsymbol{M}_j}$
Solve $\frac{d\boldsymbol{M}_j}{dt} = -|\gamma|\mu_0 \boldsymbol{M}_j \times \boldsymbol{H}_j^{eff}$
Ansatz $\boldsymbol{M}_j(t) = \boldsymbol{M}_j^S + \boldsymbol{m}_j e^{i\omega t}$
Analytic solution?
Yes
No
Analytic $\boldsymbol{m}^T, f$
Numerical f

Figure 3.6. Flowchart for determining the precessional dynamics in synthetic antiferromagnets.

For symmetric samples, the precession frequency and the phase of the dynamic components m_{jz} for the acoustic and optical modes are

$$f_\mathrm{a} = \frac{|\gamma|\mu_0}{2\pi}\sqrt{H(H + M\cos\theta)},$$
$$(m_{1z}, m_{2z}) = k_1 e^{i\omega_\mathrm{a} t}(1, 1); \tag{3.7a}$$
$$f_\mathrm{o} = \frac{|\gamma|\mu_0}{2\pi}\sqrt{H^2 + 2A^2M^2 + HM\cos\theta - 4AHM\cos\theta 2AM^2\cos(2\theta) + 2A^2M^2\cos(2\theta)},$$
$$(m_{1z}, m_{2z}) = k_2 e^{i\omega_\mathrm{o} t}(-1, 1). \tag{3.7b}$$

Here, a constant $A = J/(\mu_0 t M^2)$ is introduced in order to simplify the expressions. f_a and f_o are the frequencies for the acoustic and optical modes, and k_1 and k_2 are related to the amplitude of the precession. From the expressions of m_{jz}, it can be seen that the two layer magnetizations precess in-phase in the acoustic mode, and out-of-phase in the optical mode.

For the asymmetric samples with $t_1 = 2t$ and $t_2 = t$, a general analytic solution of the precessional dynamics cannot be obtained. It is only in the saturated state, with two layer magnetizations aligned parallel with the applied magnetic field, that there are analytic expressions for both the precession frequency and phase as follows,

$$\begin{aligned} f_\mathrm{a} &= \frac{|\gamma|\mu_0}{2\pi}\sqrt{H(H+M)}, \\ (m_{1z}, m_{2z}) &= k_1 e^{i\omega_\mathrm{a}t}(\frac{1}{2}, 1); \end{aligned} \tag{3.8a}$$

$$\begin{aligned} f_\mathrm{o} &= \frac{|\gamma|\mu_0}{2\pi}\sqrt{(H-3AM/2)(H+M-3AM/2)}, \\ (m_{1z}, m_{2z}) &= k_2 e^{i\omega_\mathrm{o}t}(-\frac{1}{2}, 1). \end{aligned} \tag{3.8b}$$

In the unsaturated states, only numerical values of the precession frequency can be obtained. In this case, an explicit expression for m_{jz} cannot be determined.

3.2.3. Discussion

Having introduced the theoretical model that is used to calculate the frequency and phase information for the precessional dynamics, a comparison can be made between the experimental data and theory, in order to identify the origin of each mode.

Identification of different precessional modes

As shown in Fig. 3.7, both the theoretical and experimental frequency dependence on the applied magnetic field is presented for each mode. The parameters used for the theoretical calculations are $M = 1042$ kA/m and $|\gamma| = 1.76 \times 10^{11}$rad/(s · T). We also determine a reference frequency $f_\mathrm{K} = \frac{|\gamma|\mu_0}{2\pi}\sqrt{H(H+M)}$, which is the frequency of the FMR mode for a single 7.5 nm-thick CoFeB film.

For Sample 1, as shown in Fig. 3.7(a), mode I and II are present for magnetic fields in the range of 100 to 300 mT, and the frequencies of both modes increase with increasing the applied magnetic field, which is in agreement with our calculations for this sample [Fig. 3.7(d)]. By comparing the experimental and theoretical results in Figs. 3.7(a) and (d), we can therefore identify mode I as the optical mode, and mode II as the acoustic mode.

For Sample 2, the observed and calculated frequency dependence is not linear, and two field regions can be identified that are separated by a discontinuity in the frequency dependence of the characteristic modes. Experimentally, a different number of modes are present in the two field regions. First, we discuss the field region with small magnetic field values, where three modes are observed, and the calculations and experiments are in a qualitatively good agreement, as shown by the red shaded area in Figs. 3.7(b) and (e). Through comparison, mode I can be identified as the acoustic mode and mode III as the optical mode. Mode II, having a frequency similar to the FMR mode in a single layer CoFeB film, is neither an acoustic nor an optical mode, and we refer it to as a transient mode. As explained later, this transient mode is due to a laser-induced decoupling between the two FM layers. We can now turn our attention to the higher magnetic field region of 190-300 mT. While the theoretical data [Fig.3.7(e), blue region], in addition to the FMR mode f_K, exhibit two modes, experimentally the three modes are first reduced to two modes, and eventually only a single mode is observed with further increase of the field. Close to 190 mT, there are discontinuities in the frequencies of the acoustic and optical modes, with mode I (III) changing to the optical (acoustic) mode.

Finally, for Sample 3 the theoretical calculations [Figs. 3.7(f)] exhibit almost linear dependence of all the modes as a function of the applied magnetic field. However,

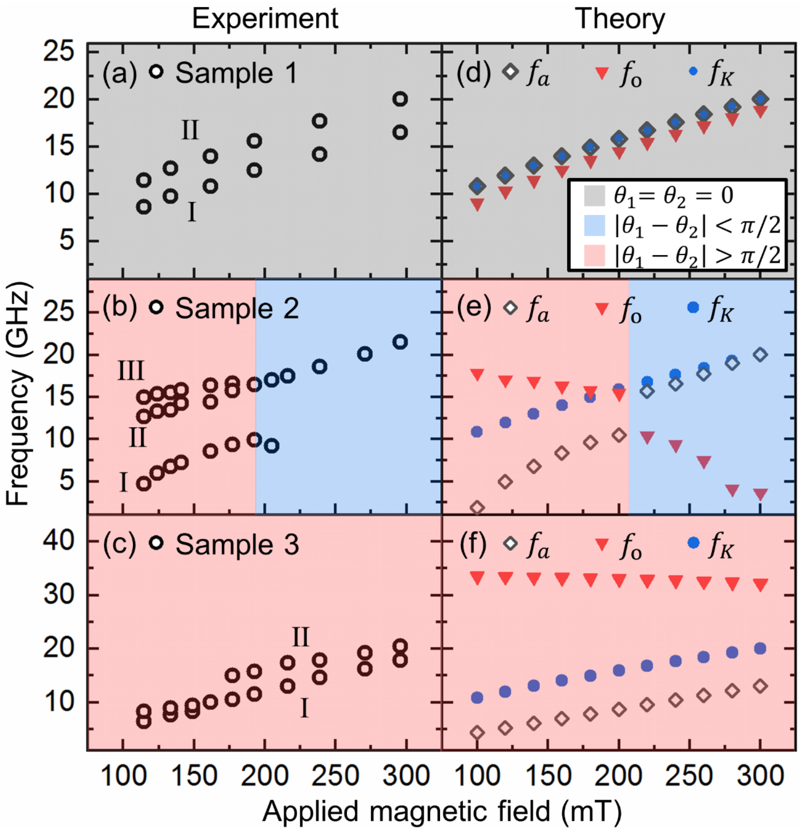

Figure 3.7. Dependence of the frequency on the applied magnetic field for the different modes. (a)-(c) Experimental data: The different precessional modes are indicated with Roman numbers. (d)-(f) Theoretical data: f_a, f_o and f_K are the frequencies of the acoustic mode, optical mode, and the FMR mode for a 7.5 nm CoFeB film. The three different background colors indicate the three field regions given in the inset of (d).

the experimental data looks, at a first glance, quite different. To reconcile our measurements with the calculations, first we note that the net MOKE signal of the optical mode ($m_{1z} = -m_{2z}$) from the two equally thick FM layers is zero, and hence cannot be observed experimentally. Therefore, for $\mu_0 H > 175$ mT, mode I, having a lower frequency than f_K, is the acoustic mode, and mode II is the transient mode. At magnetic fields $\mu_0 H < 175$ mT, two modes are also observed, but with a smaller frequency difference. As their frequencies are smaller than f_K, they cannot be attributed to the transient mode, and they might be a result of the splitting of the acoustic mode due to domain formation, as reported for a similar system [145].

To summarize, the three samples exhibit significantly different precessional dynamics, which are in good agreement with the theoretical model except for the so-called transient mode. To elucidate its origin, we have performed fluence-dependent TRMOKE measurements on Samples 2 and 3, which reveals how the transient mode evolves with varying the laser excitation fluence. Finally, we explain the relationship between the frequencies of the different modes in the three field regions [FIG. 3.7], i.e. which mode has a higher frequency, considering the relative contribution between E^{Z} and E^{IEC}.

Origin of the transient mode

In this section, we present further measurements with varying laser fluence to support our claims that the presence of the transient mode is caused by laser-induced decoupling of the FM layers due to a suppression of the IEC.

The first hint for the presence of a laser induced IEC suppression is the existence of a threshold effect in the laser fluence, which is not expected for characteristic modes of the trilayers. Indeed, as illustrated in Figs. 3.5 and 3.8, the transient mode (mode II) only appears above a laser fluence threshold of 8.2 mJ/cm^2 for Sample 2, and 13.4 mJ/cm^2 for Sample 3. The intensity of this mode increases further with the increase of the laser fluence. If we consider the energy deposited by the laser excitation, the first effect would be an increase in the temperature of the sample, which leads to a reduction of the IEC strength that is known to be dependent on temperature [134, 143]. As a result, above a certain threshold level, the two FM layers become decoupled. In this case, the magnetization precession is only driven by the applied field and the demagnetization field. Therefore, the frequency of the transient mode should be the same as the FMR mode of a single layer ferromagnetic film, as observed experimentally.

An interesting comparison between the time constant of the acoustic, optical and acoustic modes can be made, by fitting the time-resolved data with Eq. (3.5). For Sample 2, at the fluence of 8.2 mJ/cm^2, the time constant for the acoustic, optical and transient modes are 253, 150 and 104 ps, respectively. For Sample 3, at the fluence of 13.4 mJ/cm^2, the time constant for the acoustic and transient mode are

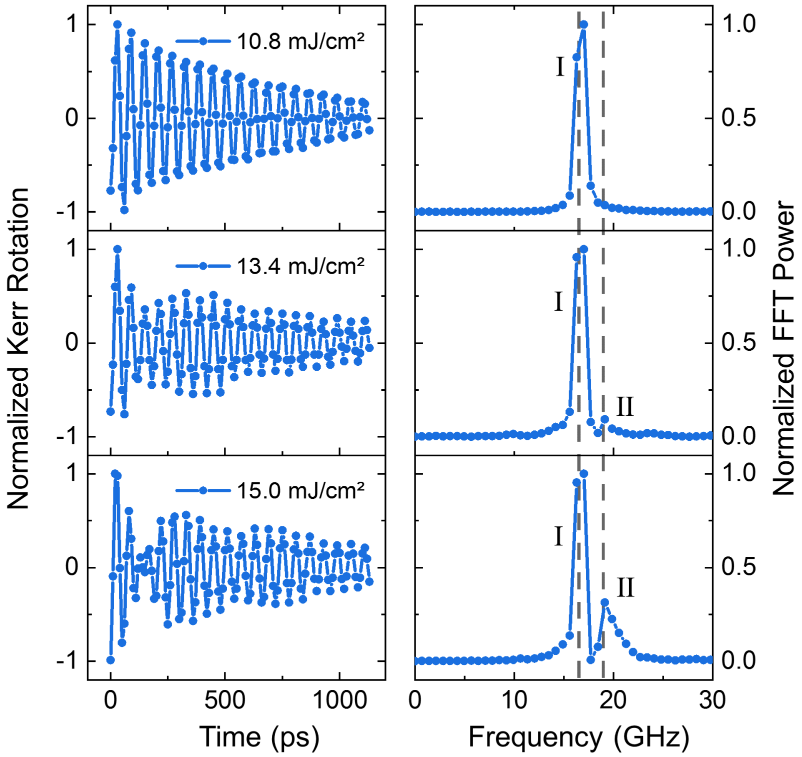

Figure 3.8. Evolution of the transient mode (mode II) with increasing fluence of the pump laser beam. Time-resolved Kerr rotation and the corresponding frequency spectra are shown in the left and right column respectively for Sample 3 at $\mu_0 H$ = 270 mT. Lines connecting the data points are guides to the eye.

936 and 317 ps. In both cases, the time constant of the transient mode is shorter than the other characteristic modes, which is due to the recovery of the IEC when the heat dissipates away. A further confirmation of the extrinsic nature of the transient mode is that a higher fluence is required to excite the transient mode in Sample 3 compared with Sample 2. This is because the IEC in Sample 3 is stronger than Sample 2, and more energy must be deposited into the sample in order to decouple the two FM layers.

Frequency relationship between different modes

Given that the frequency relationship between the different modes can be explained by considering the relative contributions of the Zeeman energy and IEC, this frequency dependence on the applied field for the different modes can be divided into three field regions, as indicated by the three background colors in Fig. 3.7. For the three samples, because of their differences in IEC strength and FM layer thicknesses, the range of the applied field that corresponds to a specific field region for each sample will be different. Hence, the three samples exhibit different precessional dynamics between 100 and 300 mT.

We first determine how the IEC modifies the frequencies of the acoustic and optical modes, compared with the reference frequency f_{K}. For the acoustic mode, its frequency f_{a} is modified by the IEC only because the IEC affects the static magnetization configuration, which is given by the $M\cos\theta$ term in Eqs. (3.7). In contrast, the frequency of the optical mode f_{o} depends on both the static magnetization configuration and effective field from the IEC, given by several terms in Eqs. (3.7) containing the constant A that is related to the IEC. Here, although Eqs. (3.7) are valid only for Sample 3, they can still provide some qualitative information about Samples 1 and 2.

Knowing how the IEC modifies the frequency of the acoustic and optical modes, it is straightforward to use the relative contribution between the E^{IEC} and E^{Z} as a criterion to analyze the frequency relationships between the different modes. Following this idea, three field regions are defined, which are quantified by the static magnetization configuration, as shown in Fig. 3.7. The first field region (in gray) is for when the samples are saturated, where E^{Z} dominates. The second field region (in blue) is for a field below the saturation field but where the field is strong enough to have an almost parallel alignment of the layer magnetizations, with $|\theta_1 - \theta_2| < \pi/2$. The third field region (in red) is where the applied field is no longer strong enough to overcome the antiparallel alignment, with $|\theta_1 - \theta_2| > \pi/2$.

We begin with the precessional dynamics in the first field region [Fig. 3.7, gray region]. As can be seen for Sample 1, in the first field region where the Zeeman energy dominates, the frequency relationship between the different modes is $f_{\mathrm{o}} < f_{\mathrm{a}} = f_{\mathrm{K}}$. For the acoustic mode, as previously stated, the IEC can only modify f_{a} if the static magnetization configuration is different from the saturated state. Since in this field region the sample is saturated, the acoustic mode has the same frequency as the FMR mode of a single layer CoFeB film. For the optical mode, the additional contribution from the effective field of the IEC $\mathbf{H}^{\mathrm{IEC}}$ needs to be considered. For a saturated sample, $\mathbf{H}^{\mathrm{IEC}}$ [corresponding to the terms including A in Eq. (3.8b)] counteracts $\mathbf{H}^{\mathrm{ext}}$, so that $f_{\mathrm{o}} < f_{\mathrm{K}}$. This can be explained by the phase difference between the precessing magnetizations in the two layers in the optical mode. For the optical mode, an antiparallel alignment of the dynamic m_z components in the two layers is favored by the antiferromagnetic IEC. In contrast, for the acoustic mode, the parallel alignment of the two dynamic m_z components is not favored by the IEC. Therefore, less energy is required to excite the optical mode, and hence the optical mode has a lower precession frequency than the acoustic mode. It should be mentioned that this argument is only valid for saturated samples, since the π-phase shift for the dynamic components is the only difference between the acoustic and optical modes.

Next, we explain the frequency relationship between different modes in the second

Table 3.9. Frequency relationship of the different modes for symmetric and asymmetric samples

Field region	Definition	Symmetric sample	Asymmetric sample
1	$\theta_1 = \theta_2 = 0$	$f_\mathrm{a} = f_\mathrm{K}$	$f_\mathrm{o} < f_\mathrm{a} = f_\mathrm{K}$
2	$\lvert\theta_1 - \theta_2\rvert < \pi/2$	$f_\mathrm{a} \approx f_\mathrm{K}$	$f_\mathrm{o} < f_\mathrm{a} \approx f_\mathrm{K}$
3	$\lvert\theta_1 - \theta_2\rvert > \pi/2$	$f_\mathrm{a} < f_\mathrm{K}$	$f_\mathrm{a} < f_\mathrm{K} < f_\mathrm{o}$

field region [Fig. 3.7(b), blue region]. This field region extends for Sample 2 from 200 to 300 mT. In this field region, the alignment of the magnetizations is not completely parallel because the Zeeman energy starts to exceed the energy associated with the IEC. Since the effects of $\mathbf{H}^{\mathrm{ext}}$ counteracts $\mathbf{H}^{\mathrm{IEC}}$ for the optical mode [Eq. (3.7b)], in this field region, the frequency of the optical mode should decrease with increasing the applied magnetic field. At the same time, since the two layer magnetizations are close to parallel alignment, the frequency of the acoustic mode is almost the same as f_K. These trends in the optical and acoustic modes are reflected by the theoretical results in Fig. 3.7(e). As for the experimental data [Fig. 3.7(b)], the acoustic mode is in good agreement with the theory, although the optical mode is only observed ~ 200 mT. We speculate that this is because the decrease of the frequency of the optical mode towards zero results in a gradual decrease of the intensity of this mode. As the optical mode already has quite a low intensity, it is therefore not possible to detect it on a further increase of the applied magnetic field.

Finally, we explain the phenomena behind the dynamics in the third field region [Figs. 3.7(b) and (c), red regions]. This field region extends for Sample 3 from 175 to 300 mT, and for Sample 2 from 100 to 200 mT. In this field region, the static magnetization configuration is close to an antiparallel alignment of the layer magnetizations, because the energy associated with the IEC is greater than the Zeeman energy. For the acoustic mode, the non-parallel alignment between the two layer magnetizations makes f_a smaller than f_K [Eq. (3.7a)]. For the optical mode, since the energy associated with IEC is stronger than the Zeeman energy, the effective field from the IEC makes the frequency of the optical mode higher than f_K. As a result, these give the frequency relationship $f_\mathrm{a} < f_\mathrm{K}$ for Sample 3, and $f_\mathrm{a} < f_\mathrm{K} < f_\mathrm{o}$ for Sample 2. For the small quantitative mismatch between the experimental and theoretical data, there could be various causes, such as a non-uniformity in the Ru layer. The above discussions is summarized in Table 3.9. For the symmetric samples in the first and second field regions, the frequency relationships are deduced, as the experimental data for Sample 3 are only available for the third field region.

3.3. TRSKM measurement of synthetic antiferromagnet

Having illustrated the coupled precessional dynamics in synthetic antiferromagnets, the next step of our investigations is to use the TRSKM setup to study propagating spin waves in such systems. However, the trial experiments did not succeed due to several reasons. One typical measurement result is shown in Fig. 3.10(c). In this case, an asymmetric sample CoFeB(5 nm)/Ru(0.4 nm)/CoFeB(10 nm) is chosen, whose hysteresis loop is shown in Fig. 3.10(a). From the hysteresis loop, it can be seen that the saturation field for this sample is approximately 0.7 T, and the antiparallel alignment of the two layer magnetizations can be maintained with

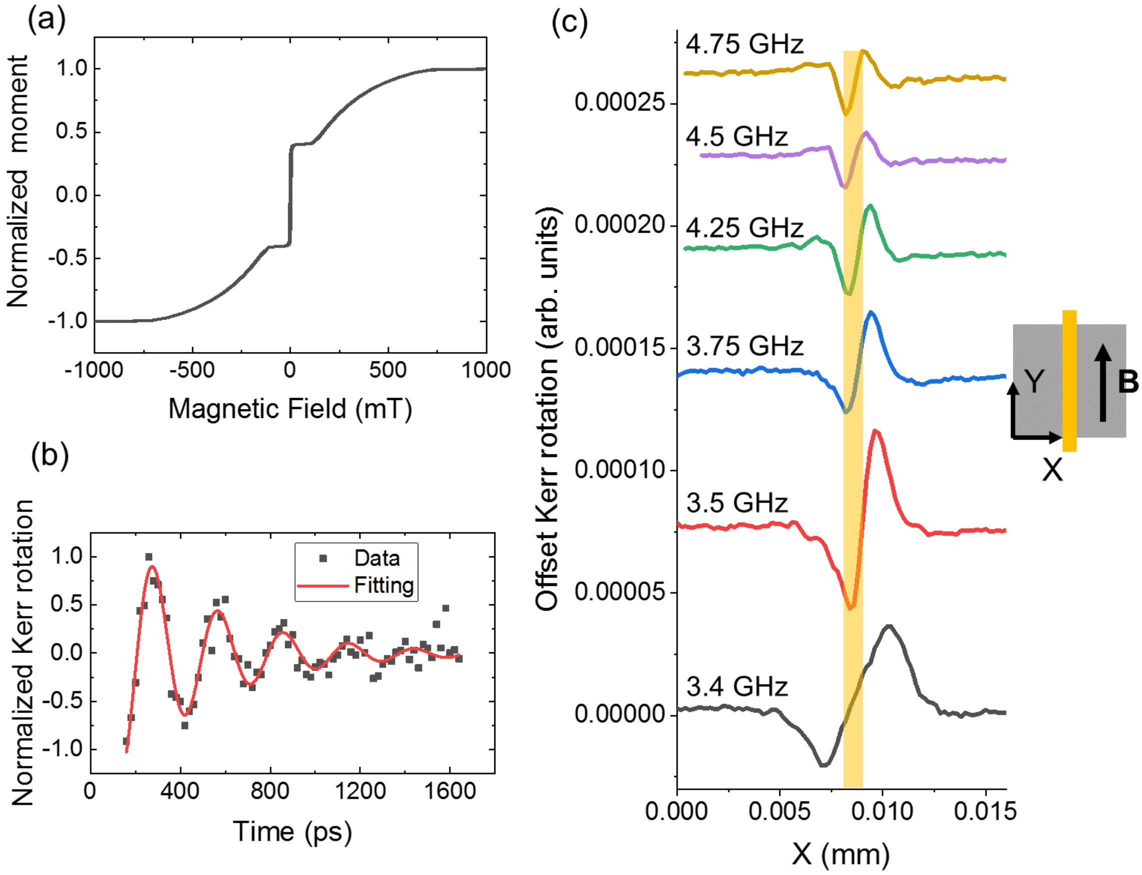

Figure 3.10. (a) Magnetic hysteresis loop of the sample CoFeB(5 nm)/Ru(0.4 nm)/CoFeB(10 nm). (b) Time-resolved Kerr rotations measured from the all-optical pump-probe experiment. (c) Scanning Kerr rotations along the X direction across the microstrip, with f_{RF} ranging from 3.4 to 4.75 GHz, and lines shifted for clarity. The positions correspond to the 1 μm microstrip are indicated by the shaded area. The magnetic field configuration and sample geometry are shown in the right schematic.

applying an external field up to 100 mT. Such properties of the hysteresis loop are specially chosen, since an antiparallel alignment is favored by the spin-wave nonreciprocity.

An all-optical pump-probe experiment is first performed for the SAF sample. The in-plane component of the magnetic field is along the direction of the microstrip transmission line [see Fig. 3.10(c)], which corresponds to a Damon-Eschbach mode when a propagating spin wave is excited. The applied field is tuned so that the precessional frequency extracted from the all-optical measurement is approximately 3.3 GHz, which is shown in Fig. 3.10(b). Based on this field, the frequency of the RF excitation is chosen to be above 3.3 GHz, so that the propagating spin waves can be excited. As shown in Fig. 3.10(c), f_{RF} is varied from 3.4 to 4.75 GHz. For each frequency, the scanning Kerr rotations along the X direction are measured. From the data, it can be seen that there is excited precession close to the microstrip, but the dynamics does not propagate away from the antenna, unlike the results in Fig. 2.7. Here, it should be noted that the shaded area in Fig. 3.10(c) is only an approximate indication for the position of the microstrip, since there is thermal drift during the measurement. Moreover, it can be seen that, as f_{RF} increases, the amplitude of the excited dynamics quickly decreases, and the excitation becomes more and more localized at the periphery of the transmission line. Other TRSKM measurements are also performed either for different SAF samples or with a backward volume mode geometry, which all exhibit similar results, i.e. no propagating spin waves can be measured.

One possible reason for this lack of propagating spin waves is the complex domain structures in SAF systems before saturation [145]. In this case, the complex spin texture limits the propagation of spin waves, since the magnitude of the spin waves will be strongly attenuated by the domain walls during the propagation [148]. Therefore, the spin waves excited by the transmission line cannot propagate over micrometers, which is the case for a uniformly magnetized film, and hence, from the measurement, seem to be localized close to the transmission. Another reason is the rather large damping value associated with the coupled precessional mode, compared to the precession in a single film. From the fitting in Fig. 3.10(b), the extracted damping is $\alpha = 0.112$. This value is much larger than the Gilbert damping for a single CoFeB film whose magnitude is on the order of 10^{-3}. Such a large damping value again indicates that the propagation of the spin waves in this system is restricted to a small region.

3.4. Conclusion

We have used TRMOKE to characterize the ultrafast-laser-induced precessional dynamics in antiferromagnetically coupled trilayer films with different IEC strength.

The precessional dynamics measured by TRMOKE depends on the relative thicknesses of the two FM layers. In asymmetric samples ($t_1 = 2t_2$), both the acoustic and optical modes are observed, whereas in the symmetric sample ($t_1 = t_2$) only the acoustic mode is observed. In addition to the two characteristic modes, a transient mode is also observed, which is due to the laser-induced decoupling of the two FM layers. Accordingly, the transient mode has the same precession frequency as the FMR mode in a single FM film, and is only present above a certain threshold of the laser excitation fluence.

We interpret the precessional dynamics in terms of a competition between the energy associated with the IEC and the Zeeman energy, and divide the precessional dynamics into three field regions depending on which energy term dominates. The first field region is for a saturated sample where the Zeeman energy dominates, and the frequency relationship between the modes is $f_\mathrm{o} < f_\mathrm{a} = f_\mathrm{K}$. The second field region is below the saturation field of the sample with $|\theta_1 - \theta_2| < \pi/2$, and the relationship between the frequencies of different modes is $f_\mathrm{o} < f_\mathrm{a} \approx f_\mathrm{K}$. The third field region is again below the saturation field of the sample but with $|\theta_1 - \theta_2| > \pi/2$, and the frequency relationship is $f_\mathrm{a} < f_\mathrm{K} < f_\mathrm{o}$. With this detailed understanding of how the IEC and Zeeman energy affect the precessional dynamics, we provide a foundation for further investigations of propagating spin waves in such systems and for using them to implement functional magnonic devices.

Finally, in Sec. 3.3, we present the data of the TRSKM measurements in antiferromagnetically coupled trilayer films. However, no propagating spin waves were observed experimentally. We think the possible reasons are the complex domain structures in such a system before it is fully saturated, and a relatively large damping value for the coupled precessional mode.

4. Spin-wave dynamics in artificial spin ice

The work of this chapter has been published in Saha et. al., Nano Letter, 21, 6, 2392-2389 (2021) [149].

Artificial spin ice, where interacting magnetic nanomagnets are arranged into periodic arrays, was originally introduced to mimic the behavior of rare earth pyrochlore materials [150, 151]. Over the past few years, the study of artificial spin ices has evolved from the creation of model systems that mimic different physical phenomena towards potential applications as functional materials [152–156]. In particular, research on the resonant behavior of artificial spin ices in the GHz range has shown rich spin-wave dynamics [152, 157, 158], which makes them suitable for use as magnonic crystals [22].

The great potential of artificial spin ices in terms of their magnonics applications comes from two aspects. The first is the variety of artificial spin ice geometries, where different building block elements, lattice symmetries and the related parameters can be used to tune the spin-wave dynamics [155, 159–162], and hence engineer different magnonic band structures [152, 163–165]. The second aspect is the programmability of magnonic crystals made of artificial spin ices. This comes from the fact that there are a large number of magnetic states, which are in principle reconfigurable for example by using external fields or through thermal relaxation [166–168]. Furthermore, it has been shown that different magnetic states can exhibit different spin-wave modes [157, 158, 169–173], as well as different magnonic band structures [152]. For example, different magnon band structures are predicted for the square ices with different magnetic configurations, as well as a dependence of the band structure on the inhomogeneous distribution of the magnetization, in particular at the edges of the nanomagnets [165]. All these properties have made artificial spin ices promising candidates for building reprogrammable functional magnonic crystals.

Here, we investigate the magnetization dynamics in ‘trident’ artificial spin ice, where the unit cell is composed of interacting horizontal and vertical nanomagnets, which has been shown to allow tuning of the frustration [36] and displays anisotropic magnetostatic interactions. Artificial spin ices built upon geometries with anisotropic interactions [174] such as chiral structures have displayed rich collective behavior during thermal relaxation [175] and field-induced dynamics [176,

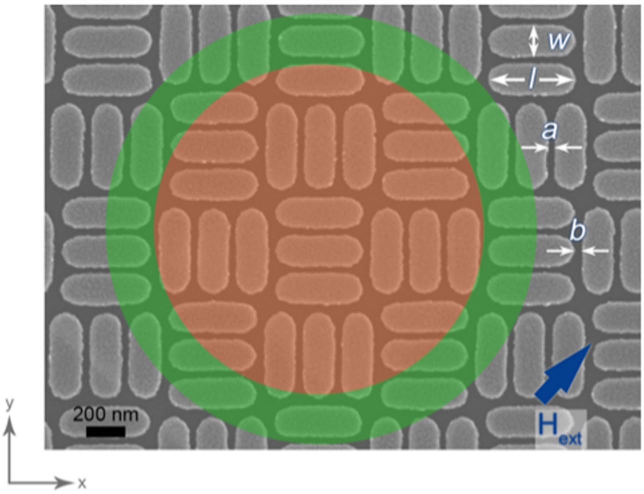

Figure 4.1. SEM image of the Py trident spin ice, with the orientation of the in-plane component of the applied magnetic field.

177], but their GHz dynamics have not been studied so far. Using the pump-probe technique with TRMOKE, described in Sec. 4.1, we show that the magnetization dynamics is characterized by a rich mode spectrum, and we determine its evolution in an external magnetic field. To explain the complex mode distribution in large arrays (Sec. 4.2), we first determine the modes for a single nanomagnet. Following this, as described in Sec. 4.3, we investigate the evolution of the mode spectrum with system size and geometry, starting with building blocks. We determine that the anisotropic magnetostatic interactions contribute to the formation of a large number of modes and that the geometry of the building blocks influences the symmetry of the spatial mode distribution. Surprisingly, while arrays larger than a unit cell exhibit mostly identical mode spectra, irrespective of their geometry, we identify specific modes, whose intensity and existence are correlated to the size of the array. The amplitude evolution of these modes reflects the long-range nature of the interactions in the studied system. Our results reveal different mechanisms for mode evolution, which can be useful for designing artificial spin ices for magnonics applications.

4.1. TRMOKE results

Finite arrays of 20 nm permalloy ($Ni_{83}Fe_{17}$) nanomagnets were prepared on a Si(110) substrate using electron-beam lithography combined with thermal evaporation at a base pressure of 2×10^{-7} mbar followed by lift-off. The ferromagnet layer was capped with a 3 nm Al layer to prevent oxidization.

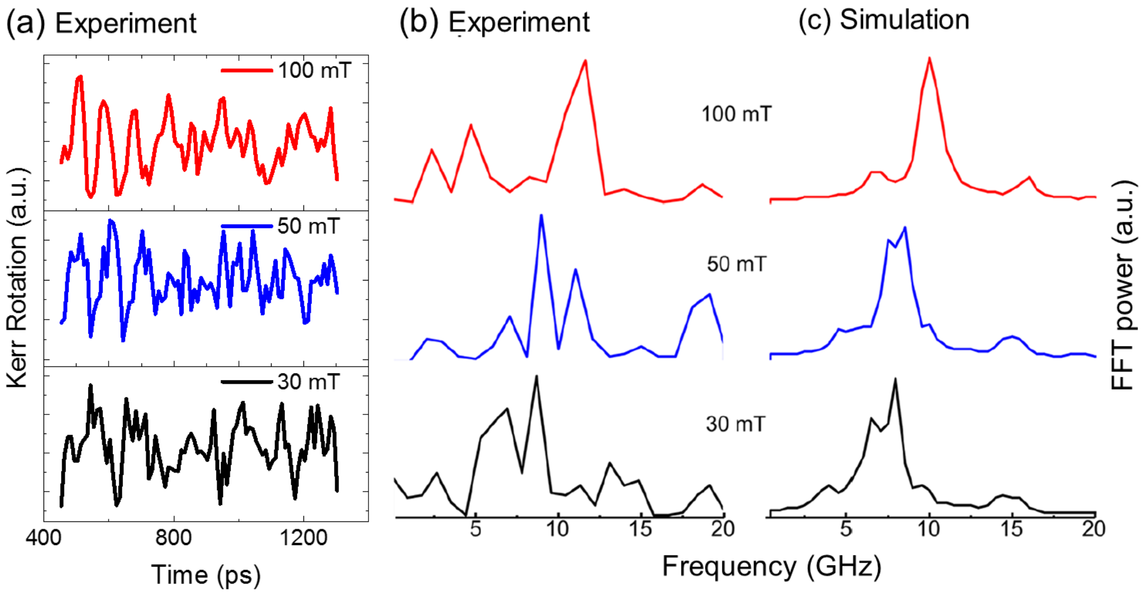

Figure 4.2. (a) Time-resolved Kerr rotation measured at the three applied magnetic fields of 100, 50 and 30 mT. (b) Frequency spectra of (a). (c) Simulated frequency spectra considering a limited excitation region [see Fig. 4.1], with a 1.5 ns relaxation time.

As depicted in Fig. 4.1, the trident ice consists of two basic groups of nanomagnets. One group consists of the three horizontally orientated nanomagnets, and the other of the three vertically orientated nanomagnets. Four geometrical parameters are defined in order to quantitatively describe the geometry of the trident lattice, which are

- w =150 nm, width of nanomagnets;
- l =450 nm, length of nanomagnets;
- a =50 nm, edge-to-edge separation between nanomagnets in each group ;
- b =50 nm, edge-to-edge separation between groups of three nanomagnets.

A distinctive feature of the trident ice is that it is more densely packed compared to the square and kagome ices, which allows for a large number of magnetostatic interactions. While in square and kagome ices, the interactions mainly occur at the ends of the nanomagnets, in trident ice, there are also interactions occurring at the long edges of the nanomagets. This leads to a rich spin-wave spectra.

The magnetization dynamics is investigated using an all-optical pump-probe setup with TRMOKE, as described in Sec. 2.2. The pump beam diameter on the sample is approximately 3 μm, with the probe beam being slightly smaller. The covered areas are indicated with green and red in Fig. 4.1, respectively. The applied magnetic field is tilted approximately 10° out of the sample plane in order to provide a demagnetization field, which is necessary for inducing coherent magnetization precession. The in-plane component of the applied magnetic field defines the state of the nanomagnets and hence determine the precessional dynamics, which is referred to as $\mathbf{H}_{\mathrm{ext}}$. The direction of $\mathbf{H}_{\mathrm{ext}}$ is at 45°, as shown in Fig. 4.2, which gives an equal contribution of the field to the two sublattices of the system (consisting of the vertical and horizontal nanomagnet groups).

The measured time-resolved precessional motion and the corresponding FFT power spectra at three different applied fields are shown in Figs. 4.2(a) and (b). For comparison, we plot the results of micromagnetic simulations in Fig. 4.2(c), where the simulated FFT spectrum is calculated considering a region of the array equivalent to the size of the probe laser spot. The micromagnetic simulations were performed using *mumax*^{3} [178]. The parameters used for the simulations were as follows: damping $\alpha = 0.006$, exchange constant $A = 1.3 \times 10^{-11}$ J/m, magnetocrystalline anisotropy constant $K = 0$, and saturation magnetization $\mu_0 M_{\mathrm{S}} = 1$ T.

From the experimental spin-wave spectra, a decrease of frequency for the main peak with the largest power can be observed when decreasing the applied field. Moreover, the main peak at 100 mT is split into two peaks when the applied field is reduced to 50 and 30 mT. These two trends present in the experimental spectra are in qualitative agreement with the simulated spectra. The relative differences in intensities and the precise frequencies of the peaks in the frequency spectra are not always reproduced, due to differences between the real sample and simulated sample. For example, the fabricated samples have edge roughness, fabrication defects, and a granular structure, which are not included in the simulations. There also is a possible difference in the saturation magnetization and gyromagnetic ratio value. The field-dependent spectra are the result of changes in the magnetic state of the nanomagnets. At 100 mT, the nanomagnets are almost uniformly magnetized, with the moments aligned towards the applied field direction. Whereas, at 30 and 50 mT, the magnetization is mostly aligned with the long axis of the nanomagnet. These two different magnetic structures subsequently result in different demagnetization field distributions. At 100 mT, the demagnetization field of nanomagnets is mainly mediated by the surface charges that are concentrated at the long edges of the nanomagnet, $\sigma \propto \mathbf{m} \cdot \mathbf{n}$, where $\mathbf{n}$ is the surface normal for the nanomagnet. At 30 and 50 mT, the demagnetization fields are mediated by surface charges as well as by volume charges, $\rho \propto \nabla \cdot \mathbf{m}$, which are located at the extremities of the nanomagnets. These different demagnetization fields therefore result in different frequency spectra.

4.2. Spin-wave dynamics in single nanomagnet

To facilitate the understanding of the spin-wave dynamics, we begin with the amplitude distributions of the modes in a single nanomagnet. As shown in Fig. 4.3(a), at 100 mT, multiple modes are present in the simulated frequency spectrum of a single nanomagnet. To illustrate the different types of modes, four modes are labeled, and their amplitude distributions are shown in Fig. 4.3(b).

For the lowest frequency mode at 5.92 GHz, it can be seen that the magnetization oscillates at the two edges of the nanomagnet, and this mode is referred to as the edge mode. The formation of the edge mode is related to the large demagnetizing field at the edges of the nanomagnet. As a result, it has a rather low frequency. For the mode at 10.84 GHz, the magnetization oscillates at the center of the nanomagnet, and we identify this mode as the closest mode to the bulk-like mode. For the other two modes at 9.72 and 15.76 GHz, it can be seen that their amplitude distributions are similar as those of the standing waves, and hence they are referred to as the higher order modes. The frequency differences between these two higher order modes are related to their node formation. It can bee seen that, for the mode at 9.72 GHz, the node formation is along the direction parallel to the magnetization, since the magnetization is aligned parallel with $\mathbf{H}_{\text{ext}}$ at 100 mT. Therefore, this mode is backward-volume like, and hence has a frequency smaller than the bulk-like mode (10.84 GHz). In contrast, the node formation for the mode at 15.76 GHz is perpendicular to the magnetization direction. As a result, it is a Damon-Eschbach like mode, and hence has a higher frequency. It should be noted that this argument only considers the magnetostatic contributions.

4.3. Evolution of dynamics from building blocks to arrays

Having identified the three types of modes in the single nanomagnet, we can now infer that, at 100 mT, the observed main peak close to 10.0 GHz [see Figs. 4.2(b) and (c)] should correspond to the bulk-like mode. Indeed, the other two types of

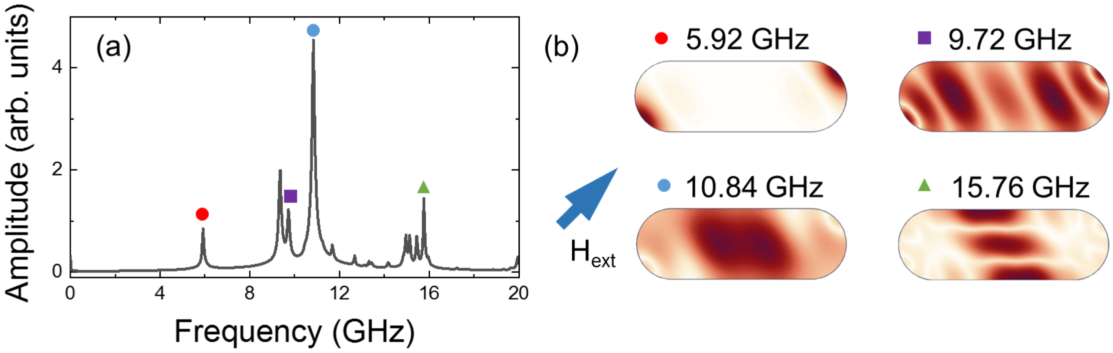

Figure 4.3. (a) Simulated frequency spectrum for a single nanomaget on applying a magnetic field of 100 mT along the direction indicated by the blue arrow. (b) Amplitude distributions of the four modes labeled in (a).

mode are difficult to measure in practice. From now on, we concentrate on the modes in the range 8-12 GHz, and examine their evolutions from the building block structures to larger arrays.

4.3.1. Spin-wave dynamics in building blocks

Three building block structures are defined for the trident lattice spin ice, as shown in Figs. 4.4(b)-(d). The first structure, the three magnet structure, consists of three horizontally or vertically orientated nanomagnets. The second structure is a 2×1 structure, which consists of 2 sets of three magnet structures, one horizontal and

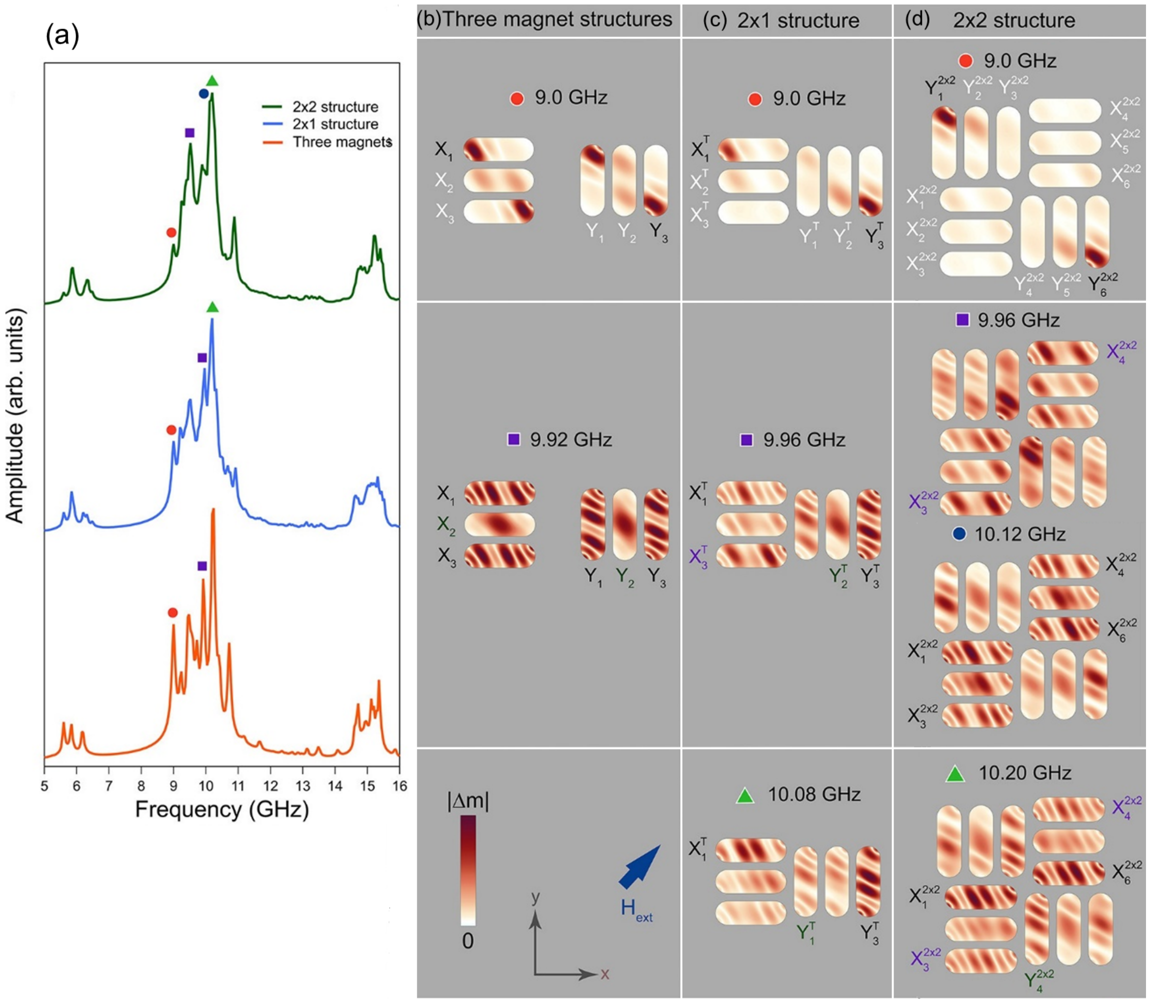

Figure 4.4. (a) Simulated spin-wave spectra of the three magnet structure, 2×1 structure and 2×2 structure with applying an external magnetic field of 100 mT along the direction indicated by the blue arrow. The spatial distributions of the labeled modes are plotted in (b), (c) and (d) for different building block geometries. The modes are marked on the spectra and in images in (b)-(d) with corresponding colored circles, squares and triangles.

one vertical, with an edge-to-edge separation of 50 nm. The third structure is the 2×2 structure that consists of 4 sets of three magnet structures. We trace evolutions of certain modes in these three structures, in order to investigate how the spin-wave modes evolve when adding building blocks. For these three geometries, micromagnetic simulations were performed using TetraMag [179]. The applied excitation field is along the out of plane direction and of the form $\sin(2\pi f t)$=$\sin(2\pi f t)/(2\pi f t)$, with the threshold frequency being 50 GHz and an integration time of 50 ns. Based on the obtained magnetization evolution, the FFT is performed to obtain the mode profiles.

We focus on the case with an applied magnetic field of 100 mT, and the frequency range of $8 - 12$ GHz [see Fig. 4.4(a)]. For the three-magnet horizontal and vertical structures, the mode at 9 GHz [see Figs. 4.4(a) and (b) with red dot] corresponds to modes mostly localized at the outermost elements, i.e. (X_1, X_3) and (Y_1, Y_3). When these two three magnet structures are arranged into the 2×1 structure, a similar mode at 9.0 GHz is observed. In this case, the modes are localized at the two outermost elements $(X_1^{\mathrm{T}}, Y_3^{\mathrm{T}})$. Interestingly, for the 2×2 structure, a similar mode at 9.0 GHz is again observed, where the intensity is concentrated at the two outermost elements $(Y_1^{2\times2}, Y_6^{2\times2})$. The spatial distribution of these modes reflects part of the symmetry of the three structures. In particular, the three magnet structures display inversion symmetry with respect to their center elements, X_2 and Y_2. For these two structures, the spin-wave modes at 9.0 GHz also display an inversion symmetry. When transferred to the 2×1 structure, such symmetry is broken, which is reflected in its spin-wave mode. When the global inversion symmetry is restored in the 2×2 structure, the mode distribution again exhibits inversion symmetry. The lack of oscillations in the other diagonal direction for the three structures is a result of the applied magnetic field $\mu_0 \mathbf{H}_{\mathrm{ext}}$=100 mT, which leads to further symmetry breaking.

Next, we discuss the second mode [see Fig. 4.4(a) with purple square markers], which is 9.92 GHz for the three magnet structures and 9.96 GHz for the 2×1 structure. For the 2×2 structure, it corresponds to two split modes, which are at 9.96 and 10.12 GHz. For the three magnet structure, this mode corresponds to higher-order oscillations in the outermost nanomagnets, and displays inversion symmetry while, for the central nanomagnet, the mode distribution is mostly bulk-like. For the 2×1 structure, a similar mode is located at the frequency value of 9.96 GHz. For this mode, the mode distribution in element Y_3^{T} is similar to that in Y_3, and the mode distribution in X_1^{T} is similar to that in X_1. Element Y_2^{T} exhibits a mode distribution very similar to that in Y_2 and X_2. The other elements display fundamentally different oscillations. For the 2×2 structure, similar modes are found at both 9.96 GHz and 10.12 GHz. At 9.96 GHz, the mode distributions in elements $X_3^{2\times2}$ and $X_4^{2\times2}$ are similar to those in X_3^{T}. At 10.12 GHz, the mode distributions in $X_1^{2\times2}$ and $X_6^{2\times2}$ are found to be the same as those in X_1 and X_3, respectively. The outer elements $X_3^{2\times2}$ and $X_4^{2\times2}$ also display similar modes.

Finally, we consider the mode at 10.08 GHz in the 2×1 structure [see Fig. 4.4(a) with green triangular markers], which has no equivalent in the three magnet structures. Features of this mode are present in the 2×2 structure, with the frequency shifted to 10.20 GHz. In particular, the mode distribution in $X_1^{2\times2}$ and $X_6^{2\times2}$ reflects that of X_1^{T} and Y_3^{T}, respectively. The mode distribution in $Y_4^{2\times2}$ is also similar to that of Y_1^{T}. Moreover, the oscillations of the magnetization in $X_3^{2\times2}$ and $X_4^{2\times2}$ are similar to those in X_1^{T} and Y_3^{T}.

Until now, we have analyzed mode profiles of the four modes in the three building-block structures. We find that the three modes at 9.0, 9.96 and 10.12 GHz can be traced back to certain modes that exhibit similar features in the three magnet structures. In contrast, for the mode at 10.20 GHz, the mode profile has no equivalent in the three magnet structures, but it is still related to the mode at 10.08 GHz in the 2×1 structure.

To further reveal the symmetry of the modes and their similarities, we discuss with the help of Fig. 4.5 the demagnetization field associated with each element ensemble. Going from the three magnet structures to the 2×1 structure [see Figs. 4.5(a) and (b)], the demagnetization field in element Y_3^{T} is almost unchanged, compared with Y_3. This leads to similar mode profiles as shown in Figs. 4.4(b) and (c). The demagnetization field in other elements of the 2×1 structure is, however, modified by the magnetostatic interactions between the two groups of nanomagnets. In particular, $X_{1,2,3}^{\mathrm{T}}$ and $Y_{1,2}^{\mathrm{T}}$ exhibit modified demagnetization fields, with the most substantial modification occurring in Y_1^{T}, which strongly interacts with the three horizontal nanomagnets. These differences in the demagnetization field are therefore responsible for the different mode profiles in Figs. 4.4(b) and (c). For the 2×2 structure, the complex and anisotropic interactions lead to a different distribution of the demagnetization field, as shown in Fig. 4.5(c). Nevertheless, some outer elements in the 2×2 structures still exhibit a similar demagnetization field distribution to that of the 2×1 structure. For example, the demagnetization field distributions in $X_3^{2\times2}$ and X_3^{T} are still similar, resulting in similar mode profiles at 9.96 GHz [see Figs. 4.4(b) and (c)].

4.3.2. Spin-wave dynamics in arrays

Having investigated the modes in the three building block structures, we now consider the dynamics in larger nanomagnet arrays. We define the array size as $i\times i$, with i being the number of groups of the three magnet structures. In Fig. 4.6(a), the spin-wave spectra are plotted for the array sizes from 2×2 to 5×5. For the 4 arrays, it can be seen that their spectra share similar features. The eigenmodes are also mostly similar, independent of the array size and edge configuration, which indicates that the dominant modes are contained within the 2×2 structure.

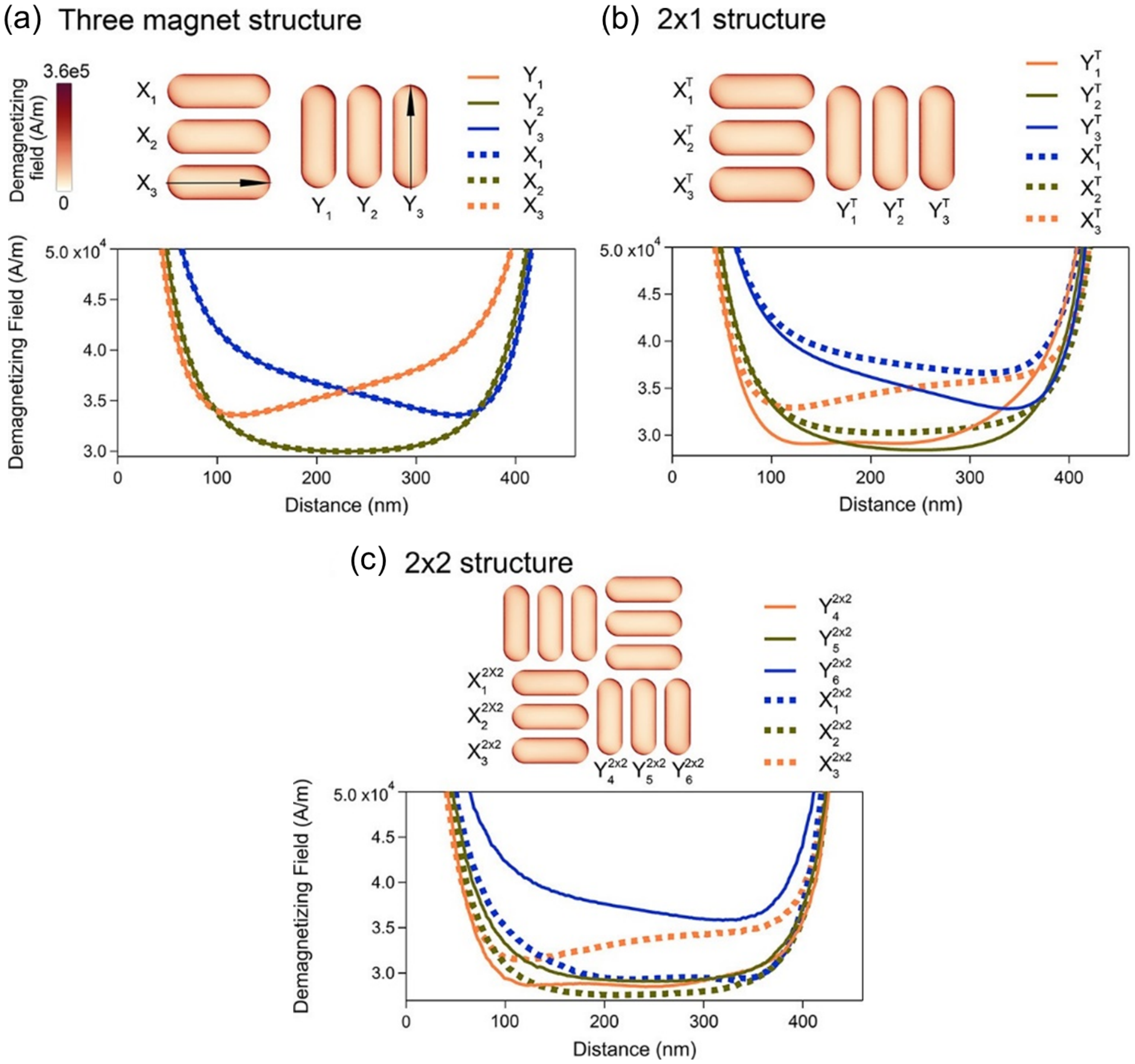

Figure 4.5. Simulated demagnetization fields for (a) three horizontal and vertical magnet structures, (b) the 2×1 structure and (c) the 2×2 structure. The demagnetization field is plotted along the arrow directions indicated in (a).

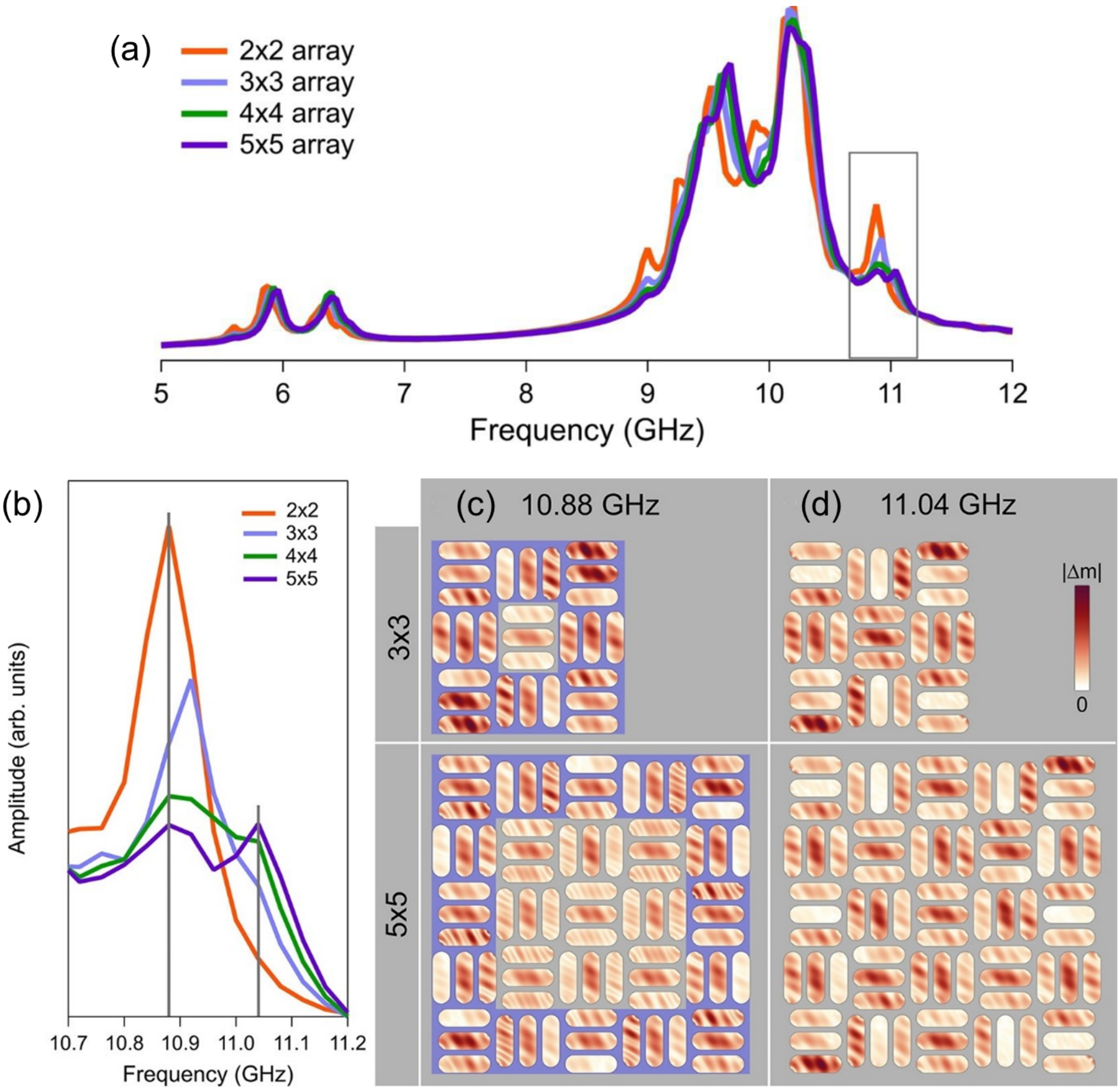

Figure 4.6. (a) Simulated spin-wave spectra for the 4 different array sizes, with a zoomed view in (b) of the part indicated by the box. (c)-(d) Spatial distributions of the two modes at 10.88 GHz and 11.04 GHz in 3×3 and 4×4 arrays.

Therefore, the 2×2 structure can be viewed as the magnetic unit cell for the trident spin ice.

In addition to the similar features, there are several modes whose behavior depends on the array size, as shown in Fig. 4.6(b) that corresponds to the part indicated by the box in Fig. 4.6(a). In particular, for the two modes at 10.88 GHz and 11.04 GHz, their amplitudes exhibit a dependence on the array size. For the mode at 10.88 GHz, its amplitude decreases as the array size increases. From the corresponding mode profiles in Fig. 4.6(c), it can be seen that the intensity is concentrated at the nanomagnets at the periphery of the array (see the highlighted blue regions). This feature of the mode distribution explains the amplitude dependence on the array size, which has a decreasing importance of the periphery nanomagnets as the array size increases. In parallel, the amplitude of the mode at 11.04 GHz increases with increasing the array size, because the mode profile displays significant amplitude within the bulk of the array [see Fig. 4.6(d)]. Following a similar mode definition as for a single nanomagnet, the two modes at 10.88 and 11.04 GHz can be defined as an array edge mode and as an array bulk-like mode, respectively.

4.4. Conclusion

To summarize, we have determined the magnetization dynamics in a trident ice geometry, which displays anisotropic magnetostatic interactions that give rise to a rich mode spectrum. Using a pump-probe technique with TRMOKE, we find that an external magnetic field can significantly modify the spin-wave spectrum. In addition, micromagnetic simulations reveal that the spatial distribution of the resulting modes strongly depends on the local symmetry and distribution of the demagnetizing field. The structural asymmetry of the system, in which groups of vertical nanomagnets interact with horizontal ones, leads to a proliferation of modes with complex spatial distributions. While most modes are present in the 2×2 unit cell of the array, we have found that the amplitude of certain well-defined modes varies as a function of the array size: depending on whether they occur at the periphery of the array or in the "bulk" of the array, their amplitude respectively decreases or increases, indicating the presence of long-range magnetostatic interactions within the system. These long-range interactions within the system are also reflected in the frequency spectra. This, in principle, allows the determination of the array size based on the mode spectra without the need to image the array.

5. Precessional dynamics in ferromagnetic fractal-like structures

In solid state physics, materials are often described in the context of crystals that consist of periodic arrays of atoms. However, there are many materials that do not belong to this category [180, 181]. Some materials have fractal structures [37, 38]. For example, for porous materials, the pores form a fractal structure and can be effectively described by the fractal theory [182, 183]. By definition, fractals are composed of self-similar structures across different length scales, which makes fractals look similar under different magnifications. This property is commonly referred to as dilation symmetry, which is the most distinctive feature of fractals [38]. In nature, there are many examples of fractals, such as snowflakes, Romanesco broccoli and coastlines. In addition, the geometry of fractals has been exploited in many artificial metamaterials for manipulating material properties [184–187]. For example, fractal cavities have been exploited to localize electromagnetic waves [184], and the microwave fractal antenna can exhibit a multiband behavior [185]. Additionally, many emergent phenomena in different physical systems exhibit fractal-like behaviors, such as the occurrence of Hofstadter butterfly [188], and fractals generated from optical and spin-wave solitons [189–192].

Following the idea of fractal metamaterials, the fractal geometry can be implemented in magnetic systems to create fractal-like ferromagnetic structures in order to modify the magnetic properties. In particular, the spin-wave properties are of great interest, since ferromagnetic structures with crystal and quasicrystal geometries have been successfully demonstrated to exhibit pronounced modifications in their spin-wave properties due to the different geometries [193–198]. For example, for a magnonic crystal, a spin-wave band structure can be artificially engineered by tuning its crystal structures [195–198]. Recently, there have been a few reports on magnonic quasicrystals, where both the localization of spin waves and self-similarity in their spin-wave spectra are found [199–202]. In a similar way, the fractal geometry should modify the corresponding spin-wave properties. Moreover, fractal structures exhibit a fractal dimension, which has a non-integer value and is commonly referred to as Hausdorff dimension [203]. This dimension defines the equivalent dimension for the magnetic interactions in between 1D and 2D, and hence can modify the spin-wave dispersion in a unique way. Early works on magnetic fractals were focused on diluted antiferromagnets, where the magnetic ions form a percolating structure that is a statistical fractal [204]. Recently, investigations of the spin-wave spectra in one deterministic fractal, Sierpinski carpets, are reported [205, 206]. In the work of Swoboda et al., the spin-wave spectra of mesoscopic ferromagnetic Sierpinski carpets are investigated using broadband ferromagnetic resonance [206].

Apart from investigating the dependence of the precessional dynamics on few relevant geometric parameters [205, 206], the relationship between the fractal geometry and the magnetostatic modes is still unknown. To address this question, we determine the evolution of magnetostatic modes, going from a simple geometric structure towards a fractal-like structure that follows the iteration process of generating fractals, with the iteration number for the structures varied from 0 to 3. For this purpose, we use a time-resolved scanning Kerr microscope (TRSKM) to characterize the precessional dynamics of two sets of samples. For square samples, where a simple square is developed towards a Sierpinski carpet [see Fig. 5.1(a)] [207, 208], we find a complex evolution of the magnetostatic modes. In contrast, for triangular samples, where a simple triangle is developed towards a Sierpinski triangle [see Fig. 5.1(a)] [209], we find a simple evolution of the modes. The experimentally obtained scanning Kerr images well represent certain features of the precessional dynamics of fractal-like ferromagnetic structures with iteration numbers up to 2, and show good agreement with the simulated results. The analysis of the mode profiles reveals that the mode formation is related to the different geometric structures. Moreover, micromagnetic simulations are performed for the square sample with iteration number of 3, whose results reveal how the scaling relation is related to the mode formation in the fractal samples. Such findings allow one to analyze the precessional modes in fractal-like structures with large iteration numbers using the mode profiles from the structure with one less iteration, thus providing an important method of analyzing such complex dynamics.

The rest of this chapter is organized as follows. In Sec. 5.1, the detailed information of sample fabrication, the geometric designs, and magnetic hysteresis loops of the two sample sets are first presented. Next, experimental details of the TRSKM measurements are explained. In Sec. 5.2.1, both experimental results of the triangular and square samples are presented. In Sec. 5.2.2, in order to confirm the experimental observations, the simulated results of the square sample with iteration number of 2 are first compared with the experimental results. Following this, the simulated mode profiles are analyzed in the context of the total static field distribution, which reveals the mode formation and the frequency relationship of the three first order local modes. In Sec. 5.2.3, simulated results of the square sample with iteration number of 3 are analyzed, which reveals the mode evolution related to the geometric scaling in fractals. Finally, in Sec. 5.3, we present our conclusions.

5.1. Experimental details

5.1.1. Sample information

Two sets of samples were prepared in order to characterize their mode evolution. One set with square shaped structures is referred to as SQ, and the other with triangle shaped structures is referred to as TRI. The ferromagnetic structures were fabricated from a 20 nm-thick Permalloy ($Ni_{83}Fe_{17}$) thin film on top of a microstrip transmission line, using electron-beam (e-beam) lithography combined with DC magnetron sputtering with a base pressure of $\sim 2 - 3 \times 10^{-8}$ mbar, followed by a lift-off process. To prevent oxidization, a 2-nm Al layer was coated on top of the ferromagnetic layer. The transmission line was fabricated on top of a high-resistivity Si substrate, using e-beam lithography in conjunction with e-beam evaporation, followed by a lift-off process. The composition of the transmission line is Cr(2 nm)/Cu(100 nm)/Cr(2 nm), and its width is 20 μm.

In order to determine the mode formation in magnetic fractals, both sample sets are developed starting from a simple geometric structure towards a fractal-like structure, as shown in Fig. 5.1(a). For square samples, the simplest one is SQ-0 that is only a square whose width is 9 μm. To generate the next sample SQ-1, a $3\mu m \times 3\mu m$ square is removed at the center of SQ-0. For the square samples, SQ-1 is defined as the base structure, with iteration number 1. This base structure can be divided into eight similar squares, each with 1/3 the width of SQ-0. For the next sample, SQ-1 is scaled by a factor of 1/3, and repeated 8 times following the pattern of SQ-1 to generate SQ-2, with iteration number 2. Following this iteration, SQ-3 is generated based on SQ-2. This iteration process can in principle go to infinity to create an ideal fractal, which is commonly referred to as a Sierpinski carpet. With such iterations, a scaling relation with a scaling factor 1/3 is developed for square samples from SQ-1 to SQ-3.

For triangular samples [see Fig. 5.1(a)], TRI-0 is an equilateral triangle with the side length of 10 μm. To generate TRI-1, an equilateral triangle is removed, whose vertices are at the centers of the three sides of TRI-0. Similar to the square samples, TRI-1 is defined as the base structure for the triangular sample set, and TRI-1 can also be divided into 4 triangles whose side length is 5 μm. To further generate TRI-2 and TRI-3, a similar iteration process can be used, but with a scaling factor of 1/2.

The magnetic properties of the two sets of samples are characterized by measuring the in-plane magnetic hysteresis loop using a Kerr microscope with the longitudinal MOKE geometry. From Figs. 5.1(b)-(e), it can be seen that all the square and triangular samples are saturated below 15 mT, which is the magnetic field applied in the TRSKM measurements.

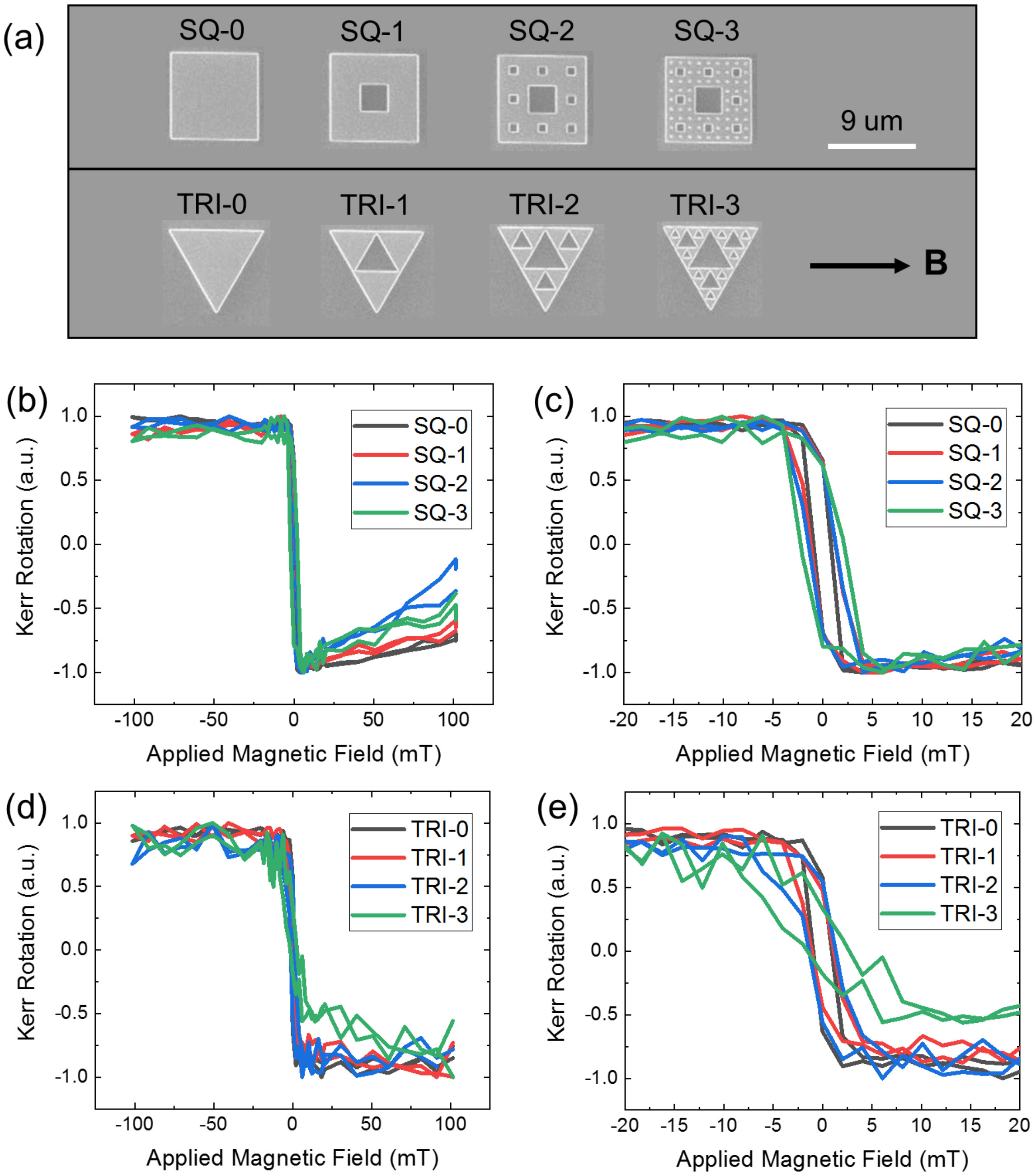

Figure 5.1. (a) SEM images of square samples SQ-0 to SQ-3, and triangular samples TRI-0 to TRI-3. (b)-(e) In-plane magnetic hysteresis loops of square and triangular samples, with the magnetic field direction shown in (a).

5.1.2. TRSKM measurement

To characterize the precessional dynamics, a TRSKM setup is used to obtain the time-resolved 2D scanning Kerr images, as described in Sec. 2.3. As shown in Fig. 5.2(a), the sample is on top of the microstrip transmission line. Hence, the in-plane component of the RF magnetic field is responsible for exciting the precessional dynamics in the sample. During the measurement, the out-of-plane component of the precessional magnetization is measured using the polar MOKE geometry. The external magnetic field is applied to the sample using a permanent magnet, with an in-plane component of 15 mT whose direction is shown in Fig. 5.2(a).

With our experimental setup, two types of measurements can be performed. The first one enables to determine the time-resolved precession of the magnetization. In this case, the probe laser is slightly defocused to cover to whole structure [see the red circle in Fig. 5.2(b)], and the Kerr rotation is measured as a function of time, in steps of 60 ps. From the measurement shown in Fig. 5.2(b), a sinusoidal oscillation at 3.7 GHz can be observed. By fitting the data with a sinusoidal function, the amplitude of the precession can be extracted.

The second type of measurement is the 2D scanning Kerr image, which represents the spatial distribution of m_z at a particular time. In this case, the probe laser is focused to the size $\sim 1.1\ \mu m$, using a microscope objective with a numerical aperture of 0.55. To perform the scanning Kerr measurement, the optical delay stage is fixed,

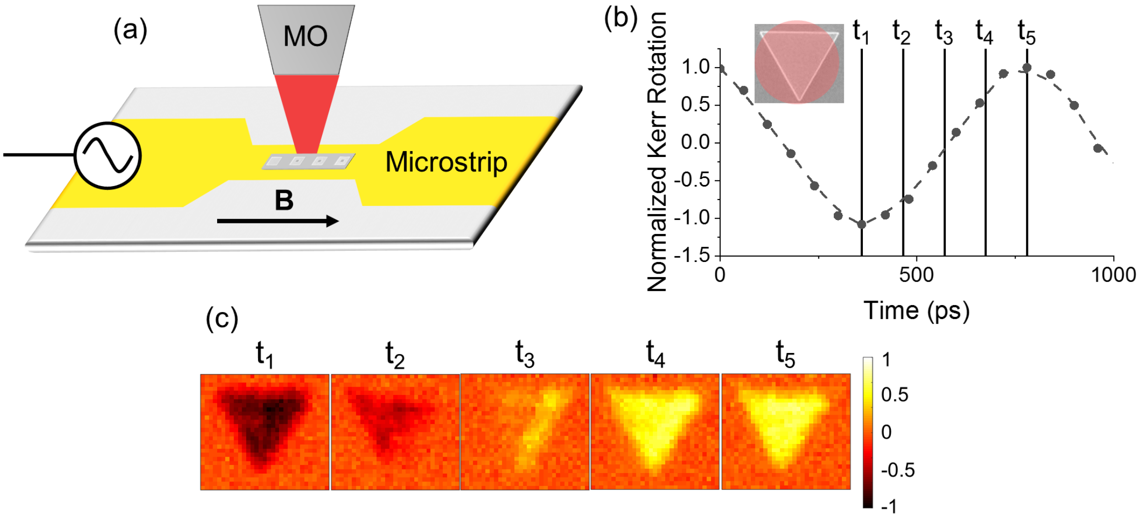

Figure 5.2. (a) Schematic of the experimental TRSKM setup at the sample. (b)-(c) TRSKM measurements of the sample TRI-0 at $B = 15$ mT and $f_{\mathrm{RF}} = 3.7$ GHz. (b) Normalized time-resolved Kerr rotation measured by a de-focused laser beam (beam size indicated by the red circle). (c) Five normalized scanning Kerr rotation images, in the range [-1,1], measured from t_1 to t_5 at 360, 465, 570, 675 and 780 ps, respectively, which are indicated by the solid lines in (b).

for example, to t_1 [see Fig. 5.2(c)]. The Kerr rotation is measured while the sample is moved by a piezo stage in the sample plane with a step size of 400 nm, which gives a 2D image. Moreover, by changing the optical delay stage, a series of scanning Kerr images over time can be obtained [see Fig. 5.2(c)], which corresponds to a half period of the precession from t_1 to t_5.

5.2. Result and discussion

5.2.1. Experimental results

The precessional dynamics for both sets of samples is measured by TRSKM with an applied magnetic field of 15 mT. For each sample, the time-resolved precession is measured in the frequency range of $f_{\mathrm{RF}} = 2.0 - 5.5$ GHz, with a step size of 0.1 GHz. The precessional amplitude for each excitation frequency is subsequently extracted in order to obtain a complete frequency spectrum [see Fig. 5.3(a)]. Next, frequency peaks in the frequency spectrum are chosen, at which the 2D scanning Kerr images are measured. For all scanning Kerr images, the optical delay is moved to a specific time, where the corresponding phase value of the sinusoidal oscillation is $\pi/2$. For example, for TRI-0 at 3.7 GHz, the optical delay stage is moved to t_5 [see Fig. 5.2(b)]. It should be noted that this time value is different for different frequencies.

We begin with the precessional dynamics observed for the triangular samples, as shown in Fig. 5.3. From the three frequency spectra of TRI-0 to TRI-2, it can be seen that one mode at 3.7 GHz is always present, as indicated by the red triangle. In addition, from the corresponding scanning Kerr images, we find that this mode corresponds to a uniform distribution of m_z at the center of the smallest triangle structure for each sample [The agreement between the experimental and simulation results of TRI-2 can be found in Fig. A.4]. The observed dynamics for the three triangular samples in Fig. 5.3 are relatively simple, since each smallest triangle structure only has point contacts with its neighbors at the vertices. As a result, only a uniform precession inside each isolated triangle structure can be observed. For TRI-3, the scanning Kerr image is not well resolved due to the limited spatial resolution [see Fig. A.3], and hence no conclusions can be obtained.

For square samples, the observed dynamics is more complex than that for triangular samples. For a better description, we first define several structures for square samples. From the schematic of SQ-2 in Fig. 5.4(d), two types of empty squares are present. We define the 3 μm × 3 μm central square as s1, and the eight 1 μm × 1 μm squares as s2. In addition, we define the 4 outermost edges for each square sample as L1 to L4. As shown in Fig. 5.4, the precessional dynamics becomes more complex when going from SQ-0 to SQ-2, in terms of both the frequency spectrum and scanning Kerr images. We begin with the precessional dynamics in SQ-0. Here, a

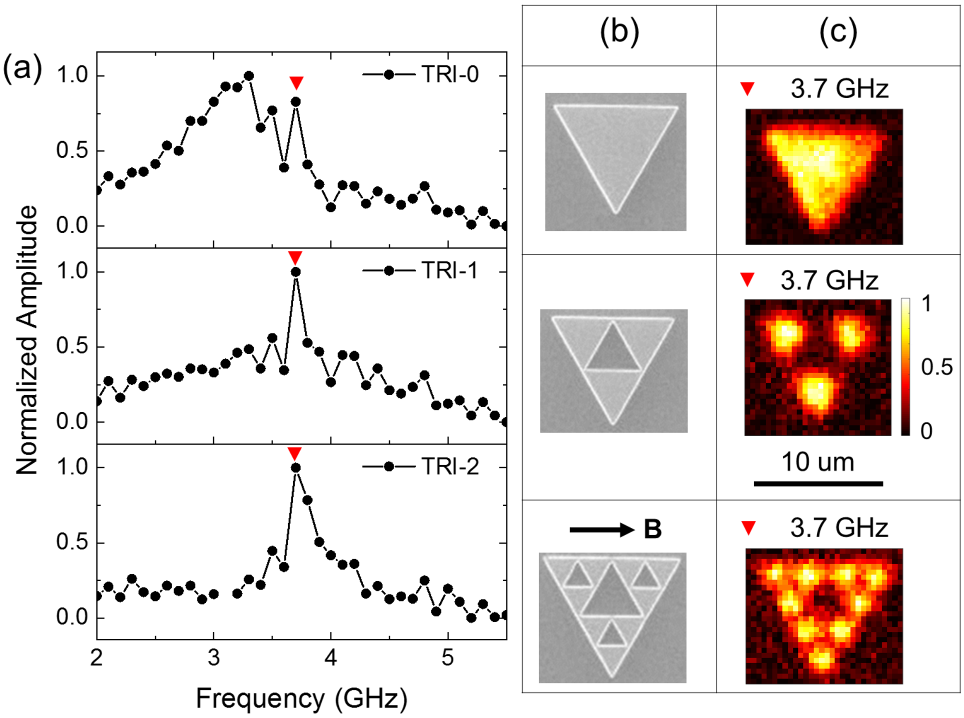

Figure 5.3. TRSKM measurements of triangular samples. (a) Frequency spectra of the triangular samples TRI-0 to TRI-2. (b) SEM images of samples TRI-0 to TRI-2, with the magnetic field direction indicated next to TRI-2. (c) Normalized scanning Kerr images at the 3.7 GHz mode for the three samples. The 3.7 GHz mode is indicated by red markers in (a).

broad peak is observed in the frequency spectrum. For the corresponding scanning Kerr images at 3.7 GHz, it can be seen that m_z is uniformly distributed across the whole square. When moving to SQ-1, the frequency peak has a small red shift, compared with that of SQ-0. For the mode at 3.1 GHz, the m_z distribution is more concentrated at the upper and lower parts of the structure.

Moving to SQ-2, the dynamics becomes complex. For the frequency spectra, multiple peaks are present, which are indicated by the three different colored markers in Fig. 5.4(a). For the mode at 3.4 GHz, the scanning Kerr image shows that the distribution of m_z is circulating along the peripheries of the eight s2 structures, forming several zigzag patterns. When the frequency is increased, a trend of localization of the dynamics occurs. For the mode at 3.7 GHz, it can be seen that the higher intensity parts of the m_z distribution form several patches next to the s2 structures. When the excitation frequency is further increased to 4.4 GHz, the patches start to merge together, forming four slightly curved worm-like structures that are oriented at the 45° and 135° directions with respect to the applied field. Moving to SQ-3, the dynamics should be in principle more complex than SQ-2, since it has further 64 smaller square structures with width ∼ 333 nm. However,

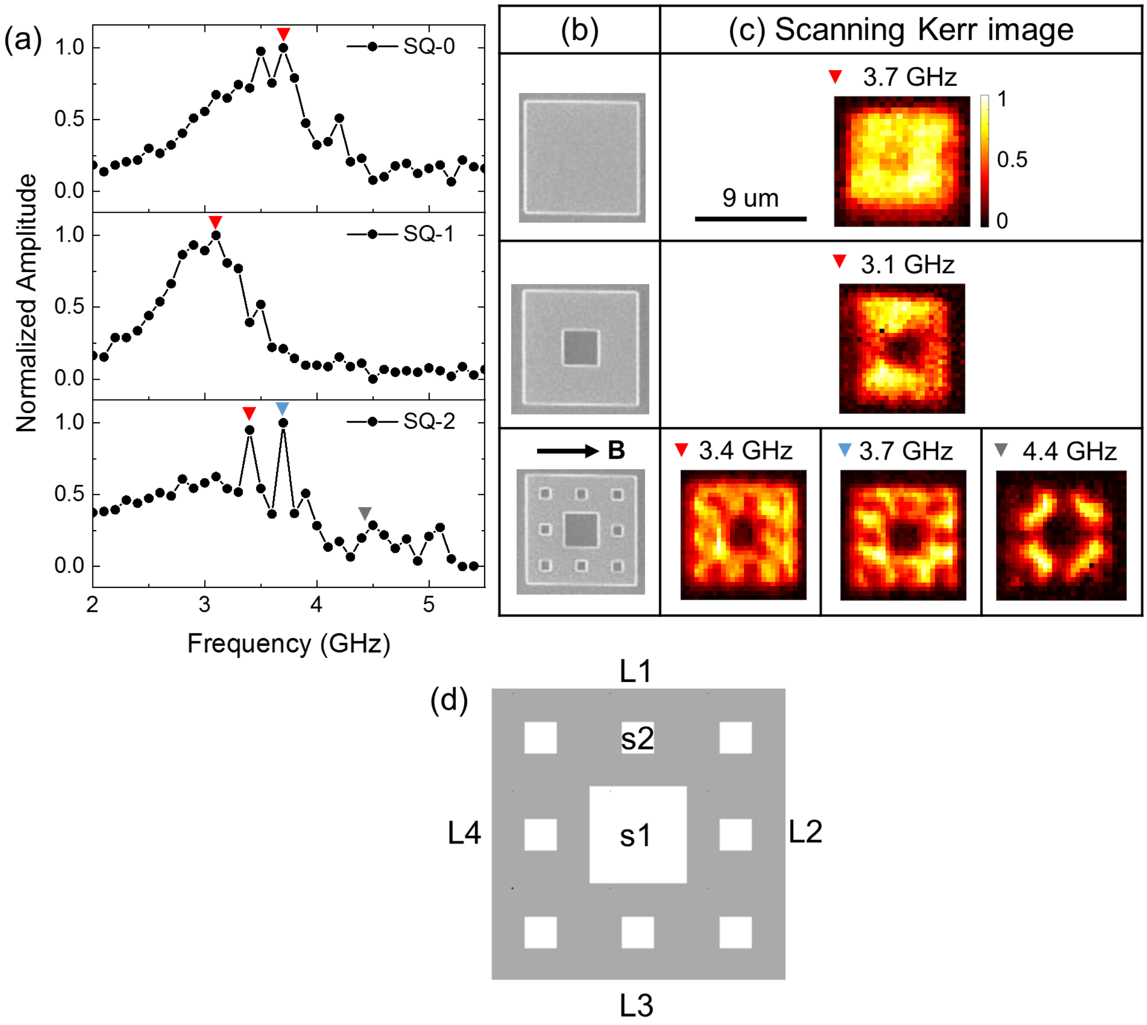

Figure 5.4. TRSKM measurements of square samples. (a) Frequency spectra of square samples SQ-0 to SQ-2. (b) SEM images of samples SQ-0 to SQ-2, with the magnetic field direction shown besides SQ-2. (c) Normalized scanning Kerr images of the different modes for the three samples. The modes corresponding to different frequencies are indicated by different colored markers in (a). (d) Schematic of the different defined structures in SQ-2. L1-L4 are the four edges with width of 9 μm, s1 is the central 3 $\mu m \times 3$ μm empty square, and s2 corresponds to the eight 1 $\mu m \times 1$ μm empty squares.

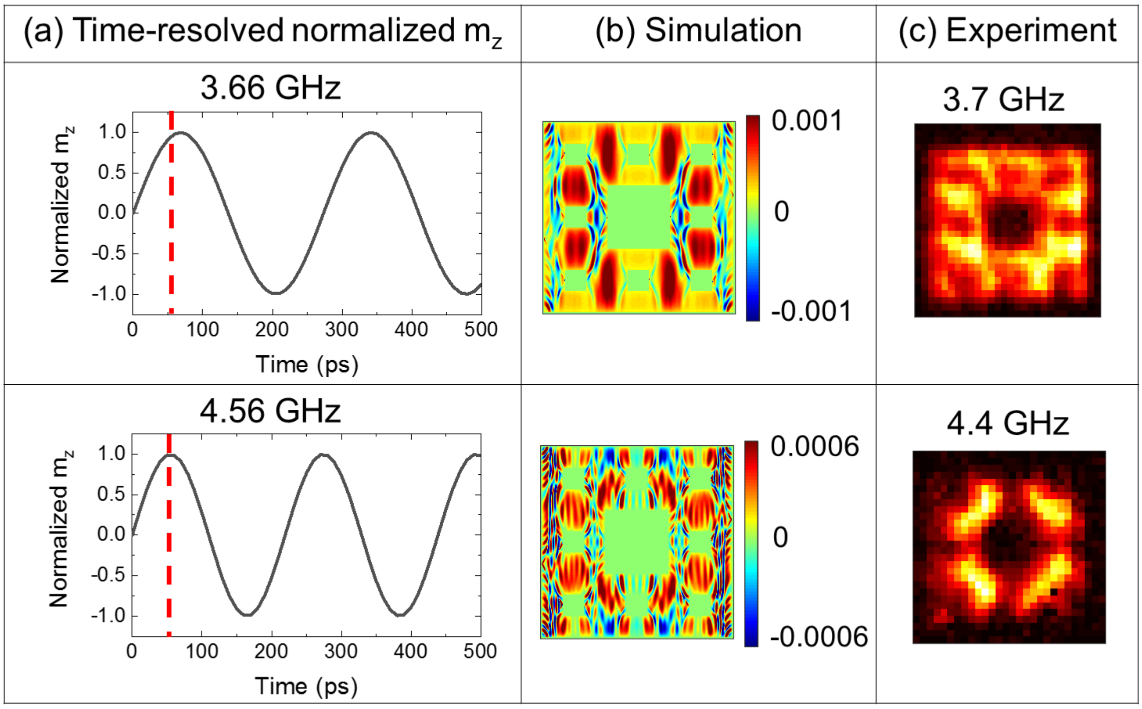

Figure 5.5. Comparison between the (c) experimental scanning Kerr images and (b) simulated m_z distribution with single frequency excitation. The simulated m_z distributions are taken at the time indicated by the red dashed lines in (a). The colormaps in (b) are set to optimize the image contrast for the spatial distribution.

since the size of the smallest structures is below the size of the laser spot, 1.1 μm, the distribution of the dynamics becomes difficult to resolve [see Fig. A.3].

5.2.2. Precessional dynamics in SQ-2

From the TRSKM measurements in Sec. 5.2.1, different dynamics are observed for the triangular and square samples, with the square sample SQ-2, in particular, exhibiting multiple modes and different spatial mode distributions. To understand the dynamics in SQ-2, micromagnetic simulations were first performed using *mumax*^{3} [178] with a single-frequency excitation field of the form $A \sin(2\pi f t)$. Here, f is the excitation frequency, and A is the amplitude of the excitation field. Such a form of single-frequency excitation corresponds precisely to the experimentally used RF magnetic field. In addition, parameters used in the simulations are as follows, damping $\alpha = 0.02$, exchange constant $A = 1.3 \times 10^{-12}$ J/m, magnetocrystalline anisotropy constant $K = 0$, and saturation magnetization $\mu_0 M_S = 0.956$ T.

As shown in Fig. 5.5, two simulation frequencies 3.66 and 4.56 GHz are chosen, which are close to the experimental ones. For both frequencies, in order to be consistent with the experimental conditions, the simulated spatial distributions of m_z are taken at the two times indicated by the red dashed lines in Fig. 5.5(a), which correspond to a phase value close to $\pi/2$ for each sinusoidal oscillation. From the two simulated spatial distributions in Fig. 5.5(b), it can be clearly seen that, for 3.66 GHz, there are eight lobe-like structures located in between the s2 structures and, for 4.56 GHz, there are four worm-like structures at the corners of the s1 structure, which match well with the experimental results in Fig. 5.5(c). The small discrepancies between the experimental and simulation frequency and phase values may be due to a variety of effects, such as edge roughness and a possible difference in the saturation magnetization values.

Apart from a good agreement between the experimental and simulation results, the results in Fig. 5.5(c) do not contain the complete information of the precessional dynamics, since the phase of the precession varies in space [see Fig. 5.6(b)]. Therefore, the m_z distribution at phase $\pi/2$ of the averaged m_z evolution is not the amplitude distribution of the mode. To obtain the complete information for each mode, another series of micromagnetic simulations are performed for SQ-2, using an excitation of the form $A\mathrm{sinc}(2\pi f t) = A\sin(2\pi f t)/(2\pi f t)$, with the threshold frequency at 10 GHz. The other simulation parameters are the same as those used for the single-frequency excitation.

The simulated frequency spectrum of SQ-2 in the range of $0-8$ GHz is shown in Fig. 5.6(a). As indicated by the different colored areas, the observed modes are classified into three categories, the edge mode (E), the first order local mode (M) and the higher order mode (HO). The three edge modes are at 1.71, 2.00 and 2.26 GHz. For mode E1 at 1.71 GHz, its mode profile is shown in Fig. 5.6(b). It can be seen that its amplitude is concentrated at the two edges L2 and L4, and the two vertical edges of s1.

The three first order local modes, M1 to M3, have frequency values of 3.66, 4.18 and 5.08 GHz, respectively, and their mode profiles are shown in Fig. 5.6(b). For these three modes, the higher intensity parts of their amplitude distribution form three characteristic patterns. For M1, the mode forms four vertically orientated lobe-like structures, each located in between the two vertical edges of s2. For M2, the mode forms four rounded structures, each located in between the two horizontal edges of s2. For M3, the mode forms a rather different pattern, which contains eight bar-like structures, four at the upper part, and four at the lower part of SQ-2. Since the amplitudes of these modes concentrate at positions near the s2 structures and each local precession is almost uniform with a phase variation smaller than 0.07π [see Fig. 5.6(b)], we refer these three modes as first order local modes.

For the two higher order modes at 5.34 and 6.27 GHz, the mode profiles are similar to that of a standing wave, since a phase change of π can be observed between the two neighboring intensity peaks [see Fig. 5.6(b)], indicating the node formation. Moreover, it can be seen that, for both modes, the π phase change is along the vertical direction, which is perpendicular to the magnetization direction. Therefore,

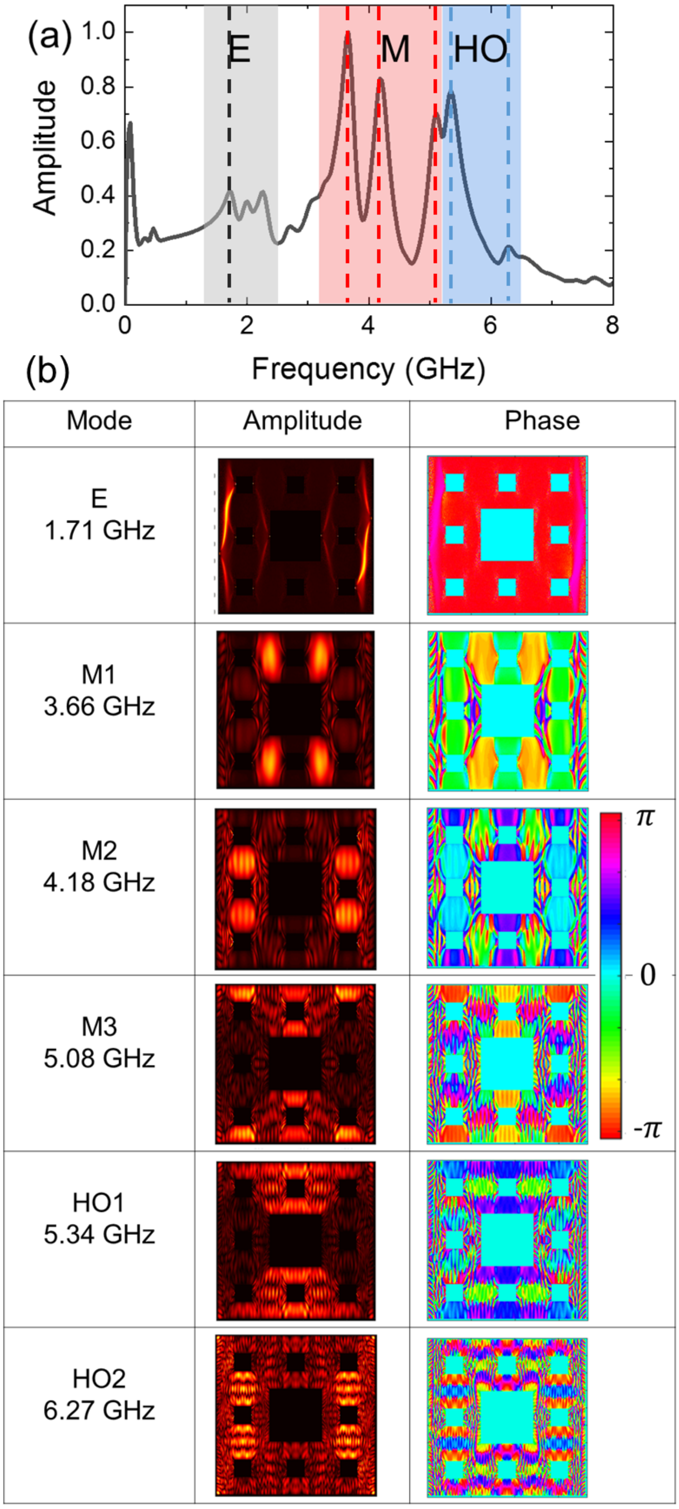

Figure 5.6. Simulated precessional dynamics of SQ-2. (a) Frequency spectrum of SQ-2 at 15 mT. The shaded areas with different colors indicate the three types of modes, edge mode (E), first order local mode (M) and higher order mode (HO). (b) Mode profiles of the six modes indicated by the dashed lines in (a). For the amplitude distribution, each colormap is set to optimize the image contrast.

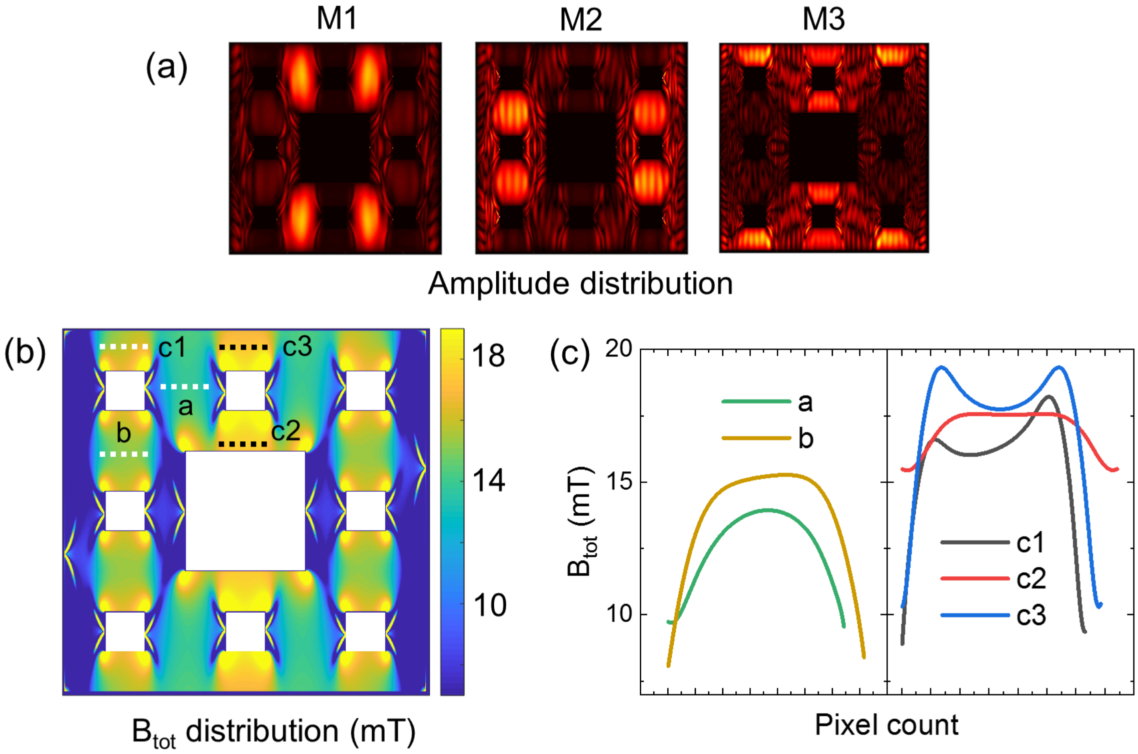

Figure 5.7. (a) Amplitude distribution of the three bulk-like modes M1 to M3 of SQ-2. The colormap is adapted to show the best contrast. (b) Total field distribution B_{tot} inside the magnetic structure of SQ-2. (d) Five line profiles of the total field distribution along the horizontal direction, with positions indicated by dashed lines in (c).

these two higher order modes are Damon-Eschbach-like, and hence have higher frequencies than the first order modes.

Having identified the three types of modes, we now analyze their formation. For this purpose, the total internal field distribution for the static magnetic system is used, which is shown in Fig. 5.7(b). The total field B_{tot} consists of three contributions, the applied magnetic field, demagnetizing field and exchange field. From the B_{tot} distribution in Fig. 5.7(b), it can be seen that there are approximately four regions [in dark blue color] with B_{tot} below 7 mT. Two of the regions are near the two edges L2 and L4 [see definitions in Fig. 5.4(d)], and the other two are near the two edges of s1. In these regions, the edge modes are formed whose low frequencies are consistent with the small values of B_{tot}. The reason for this is that the applied magnetic field is along the horizontal direction, which aligns the magnetization horizontally. As a result, the magnetic 'charge' is concentrated at the vertical edges of the structures, which produces a large demagnetizing field that compensates the external field.

To analyze the formation of the three first order local modes, we map their mode patterns [see Fig. 5.7(a)] onto the corresponding regions in the B_{tot} distribution.

As shown in Fig. 5.7(b), it can be seen that these modes occur at the regions whose B_{tot} value is around 15 mT, which is the value of the applied magnetic field. In these regions, the total internal field is still dominated by the applied magnetic field. As a result, the local precessional dynamics is similar to the uniform ferromagnetic resonance. However, due to structuring, the demagnetizing field is locally modified, and hence the uniform precession becomes localized and splits into different frequencies. To quantify the influence of such a variance in the demagnetizing field distribution, five line profiles of B_{tot} at five different regions are taken, which are indicated by the dotted lines in Fig. 5.7(b). According to the averaged B_{tot} value at the plateaus [see Fig. 5.7(c)], the fives regions are classified as three groups. For the three line profiles at c1 to c3, their values overlap with each other, and hence the three regions are classified as the same group. It can be clearly seen that for the three grouped regions, the relationship of their corresponding B_{tot} value is,

$$B_{\mathrm{tot}}^{\mathrm{c1,c2,c3}} > B_{\mathrm{tot}}^{\mathrm{b}} > B_{\mathrm{tot}}^{\mathrm{a}}. \tag{5.1}$$

This relationship is in exact agreement with the frequency relationship of the three modes M1 to M3, which is

$$f_{\mathrm{M3}} > f_{\mathrm{M2}} > f_{\mathrm{M1}}. \tag{5.2}$$

The agreement between the two relationships again confirms the first order nature of the three modes, and provides a semi-quantitative explanation for these modes.

Having analyzed all mode profiles for SQ-2, we look back at the experimental observations shown in Fig. 5.5. Now, the experimentally observed three modes should all be ascribed to the category of the first order local mode. At 3.7 and 4.4 GHz, the two scanning Kerr images indeed resemble some features of the simulated amplitude distributions for mode M1 and M2. However, due to the phase variation in space, the scanning Kerr images do not contain the complete information for the modes.

5.2.3. Precessional dynamics in SQ-3

So far, the precessional dynamics of SQ-2 can be explained in the context of B_{tot} distribution. We have seen that the three modes M1, M2 and M3 result from the different size structures in SQ-2. However, the fractal geometry of SQ-2 is not prominently present in its precessional dynamics. To further reveal the role of the fractal geometry, we performed micromagnetic simulations for SQ-3, using a sinc excitation similar to that used for SQ-2.

From the simulated results, the three first order local modes at 4.30 (M1′), 6.04 and 7.55 (M3′) GHz are picked, whose amplitude distributions are shown in Fig. 5.8(c). The complete mode profiles containing phase distributions are shown in Fig. A.5. To analyze these modes, we note that there is a scaling relation between samples

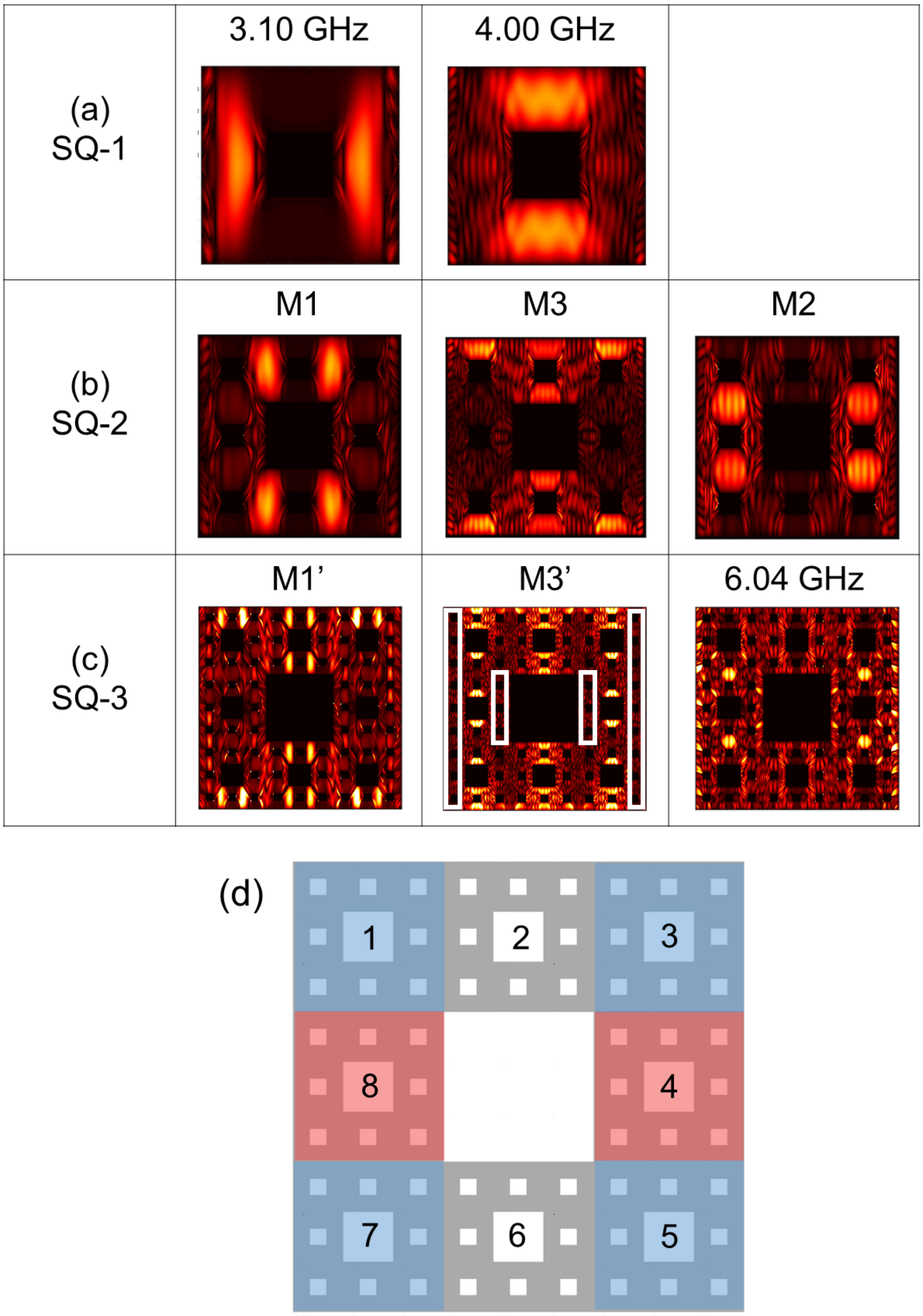
3.10 GHz
4.00 GHz
(a)
SQ-1
M1
M3
M2
(b)
SQ-2
M1'
M3'
6.04 GHz
(c)
SQ-3
(d)
1
2
3
8
4
7
6
5

Figure 5.8. Mode evolution from SQ-1 to SQ-3. (a) Amplitude distributions of the two modes at 3.10 and 4.00 GHz for SQ-1. (b) Amplitude distributions of the three modes M1 to M3 for SQ-2. (c) Amplitude distributions of the three modes for SQ-3 at 4.30 GHz (M1′), 7.55 GHz (M3′) and 6.04 GHz. The white boxes mark the regions where the edge modes occur. (d) Schematic of SQ-3, with different color shaded areas indicating the eight scaled SQ-2 structures $SQ-2(j)$, $j = 1-8$.

SQ-3 and SQ-2, namely that SQ-3 is composed of eight scaled $SQ-2(j)$ structures with a scaling factor of 1/3 [see Fig. 5.8(d)]. Following this connection, we will use the scaling relation to explain the formation of the three modes in SQ-3. For this purpose, the amplitude distributions of the three modes for SQ-2, M1 to M3, are plotted in Fig. 5.8(b) for comparison.

By comparing the six modes in Figs. 5.8(b) and (c), it can be identified that M1 and M1′, M3 and M3′ have some geometric similarities in the amplitude distribution with each other. More specifically, within the two structures $SQ-2(2,6)$ [see Fig. 5.8(d)], the amplitude distributions of M1′ and M3′ are exactly two scaled patterns of the amplitude distributions of M1 and M3, respectively. For the other six scaled $SQ-2(j)$ structures, they either exhibit part of the scaled patterns from M1 and M3, or exhibit no modes. From these observations, we infer that M1 and M3 evolve into modes M1′ and M3′, and exhibit scaled amplitude distributions in the corresponding scaled $SQ-2(j)$ structures but with certain modifications. In contrast, a different evolution of mode M2 is found when SQ-2 is scaled to generate SQ-3. It can be seen that, for the mode at 6.04 GHz, the mode distribution is not located within the eight scaled structures $SQ-2(j)$, but at the center locations where $SQ-2(4,8)$ connect with their neighboring structures.

In order to explain the observed different mode evolution, we need to find the necessary conditions for a scaled mode pattern from SQ-2 to occur in the $SQ-2(j)$ structures of SQ-3. We first identify the associated magnetic boundaries that define the three modes M1 to M3. As shown in Fig. 5.7(b), the formation of modes M1 to M3 are associated with the geometric edges of different structures in SQ-2. These geometric edges define the magnetic boundary conditions for magnetostatics, and hence determine the corresponding modes. Although all the magnetic boundaries contribute in defining the modes, it should be noted that, when SQ-2 is scaled into $SQ-2(j)$, only some of the edges from L1 to L4 disappear, and other edges are scaled accordingly. Therefore, we only need to identify the contributions from L1 to L4 for these three modes, which are L1 and L3 for both M1 and M3, and L2 and L4 for M2. Following this, we find the first necessary condition, which is that within one $SQ-2(j)$ structure, for one specific mode, only if the associated magnetic boundaries from L1 to L4 are present, a scaled pattern of the corresponding mode in SQ-2 can occur. Following this, we can explain the evolution of M1 to M1′. For $SQ-2(2,6)$, both L1 and L3 are present, and hence two scaled patterns of M1 are observed. For $SQ-2(1,3)$, since L3 is missing, only the upper part of the scaled pattern of M1 is present. For the rest $SQ-2(j)$ structures, it is a similar case.

Next, we explain the evolution of M3 to M3′. A similar analysis can be made by considering L1 and L3. However, a difference can be seen, namely part of the scaled patterns is missing at the regions marked by the white boxes in Fig. 5.8(b). For this difference, it should be noted that these regions indeed correspond to those where the edge modes occur. Therefore, at 7.55 GHz, no first order modes will be observed in these regions. Now, we find the second necessary condition for the occurrence of a scaled pattern in SQ-3, which is that the local modes must not coincide with the regions for the edge modes. After evaluating the two conditions for M2, it can be seen that none of the $\mathrm{SQ}-2(j)$ structures can fulfill these two conditions simultaneously. Therefore, M2 cannot evolve to a mode in SQ-3 with a self-similar amplitude distribution. As a result, although the mode at 6.04 GHz seems to be related to M2, it is not an evolution of M2 related to the geometric scaling.

By analyzing SQ-3, we find a trend for the mode evolution from SQ-2 to SQ-3, which is that the mode is inclined to form a scaled pattern within the corresponding scaled $\mathrm{SQ}-2(j)$ structures following the geometric scaling. In addition, two necessary conditions are required for this. To confirm our findings, we can examine the mode evolution from SQ-1 to SQ-2 [see Figs. 5.8(a) and (b)]. Here, SQ-2 can be viewed as 8 scaled $\mathrm{SQ}-1(j)$ structures. In this way, it can be seen that the mode at 4.00 GHz evolves into M3 in a similar fashion to the evolution of M1 into M1′, with the associated magnetic boundaries being L1 and L3. Therefore, the mode M3’ can actually be traced back to the mode at 4.00 GHz in SQ-1. In contrast, for the mode at 3.10 GHz in SQ-1, it is similar to the case of M2, and does not evolve to form scaled patterns in SQ-2.

Now, we extend our argument into a more general case, i.e. the mode evolution from SQ-i to SQ-$i+1$, with i being the iteration number. Indeed, our argument should remain valid, only if the dominating interaction in these structures is magnetostatics. Since in Maxwell's equations, there are no characteristic length scales, the distribution of the magnetostatic field can remain self-similar after scaling, if all the boundary conditions are scaled accordingly. Therefore, we can infer that, for any fractal-like structure with iteration number $i+1$, we can analyze its mode profiles using the mode profiles of the structure with iteration number i, along with considering the associated magnetic boundaries. This method provides a new perspective for analyzing the magnetostatic modes in fractal-like structures, which is effectively a “reversal” of the iteration process of the fractal generation. This perspective can be extremely important when analyzing a structure with a large iteration number, since it is possible to reduce the complexity of the analysis by just considering the mode profiles for the structure with one less iteration. This analysis process can also form an iteration, i.e. we can repeat this process and trace back to the structure whose mode profiles are simple, as demonstrated . In this way, we can use the simple dynamics in the base structures to explain the complex dynamics in fractal-like structures via the geometric scaling.

5.3. Conclusion

In summary, we have investigated the precessional dynamics in ferromagnetic fractal-like structures. Using the TRSKM setup, we obtain the scanning Kerr images that represent the m_z distribution at a particular time for the different modes. Based on the experimental observations, we find a simple evolution of the mode at 3.7 GHz from TRI-0 to TRI-2. Whereas, the observed dynamics from SQ-0 to SQ-2 evolve from a single-frequency spectrum into a multiple-frequency spectrum with different spatial distributions.

Despite the fact that we have found a good agreement between the experimental and simulated results, we find that the experimental results cannot give the complete information about the modes, since the precession phase varies across the sample. Therefore, further micromagnetic simulations were performed for SQ-2 and SQ-3 to obtain their complete mode profiles. For SQ-2, the precessional dynamics is analyzed in the context of the total field distribution. Using this method, the formation of the three different types of modes in SQ-2, as well as the frequency relationship for the three first order local modes are explained. For SQ-3, the simulated dynamics is found to be related to SQ-2 with the scaling relation defined in the fractal structures. Following this, we argue that the mode profiles for SQ-3 can be analyzed by relating certain modes to the ones of SQ-2, if the associated boundaries for these modes are also scaled accordingly. Using this method, the mode M1′ and M3′ are found to originate from SQ-2, i.e. within some scaled structures of SQ-3, the mode distributions of M1′ and M3′ are simply the scaled patterns of M1 and M3 in SQ-2. These findings reveal a general trend of the mode formation in magnetic fractal-like structures that is related to the geometric scaling in the fractal generation process, and provide a new perspective in the understanding of the corresponding precessional dynamics.

6. Conclusions and outlook

Two research directions are presented in this thesis, both aiming at tuning the precessional dynamics by manipulating the different magnetic interactions. More specifically, the precessional dynamics of the magnetization in both magnetic trilayers and magnetic 2D structures are characterized, in order to determine how the interlayer coupling and different geometries modify the precessional dynamics.

6.1. Magnetic trilayers

We have determined the precessional dynamics in magnetic trilayers, in which two ferromagnetic layers are coupled antiferromagnetically via a nonmagnetic interlayer. Such interlayer coupling results in a coupled precession that has two characteristic modes, the acoustic mode and the optical mode. Using an all-optical pump-probe setup with TRMOKE, both the acoustic and optical modes are observed. In addition, we observe a transient mode whose occurrence depends on the pump laser excitation energy density, and we find that this mode can be explained by a laser-induced decoupling between the two ferromagnetic layers.

Although the observed coupled precession seems to depend on many physical quantities and experimental parameters, the two most important ones are the interlayer exchange coupling and the applied magnetic field. Following this, we exploit the competition between the Zeeman energy and the energy associated with the interlayer coupling to provide a comprehensive understanding of the different modes. We find that the precessional dynamics behaves qualitatively different in three magnetic field regions, which are related to the static magnetization configuration. The first field region is where the sample is saturated, with the two layer magnetizations being parallel. In this field region, the frequency relationship between the acoustic mode (f_a), optical mode (f_o), and the transient mode (f_K) is $f_\mathrm{o} < f_\mathrm{a} = f_\mathrm{K}$. The second field region is below the saturation field of the sample where the angle between the two layer magnetizations smaller than $\pi/2$, with the frequency relationship being $f_\mathrm{o} < f_\mathrm{a} \approx f_\mathrm{K}$. The third field region is again below the saturation field of the sample but with the angle between the two layer magnetizations larger than $\pi/2$, and the frequency relationship is $f_\mathrm{a} < f_\mathrm{K} < f_\mathrm{o}$.

This perspective of analyzing the precession provides a universal description for magnetic trilayers with different ferromagnetic layer thicknesses and different interlayer coupling strengths, since the definitions of the three field regions are related to the specific values of these parameters. One more point can be considered regarding the demagnetizing field, which strengthens the validity of this method. In particular, the demagnetizing field contributes to the precessional dynamics significantly. However, in such thin film systems, the form of the demagnetization field is always $-m_z$. Here, m_z is the out-of-plane component of the magnetization. Therefore, this contribution can be treated as an additional modification to the precessional dynamics, and it is independent of the Zeeman energy and the interlayer coupling. This means that, when describing the precessional dynamics, by only considering the competition between the Zeeman energy and the energy associated with the interlayer coupling, we can nevertheless reveal the general trend of such a coupled precession.

6.2. Magnetic 2D structures

In this thesis, another route of tuning the precessional dynamics based on magnetic 2D structures is illustrated. From a general perspective, this approach is motivated by the fact that the geometric boundaries of the 2D structures define the boundary conditions for the magnetostatic modes, and hence determine their frequencies. Equivalently, the demagnetizing field is modified by the 2D structures and hence drives the precession differently. Based on these principles, the features of the geometric structure, as well as the associated symmetries can be inherited in the precessional dynamics. In this thesis, we investigate both the crystal geometry of a trident lattice, and the fractal geometry of both the Sierpinski carpet and the Sierpinski triangle.

In the trident spin ice, horizontally and vertically orientated nanomagnets interact via the magnetostatic interaction. From the experimental results, we find that the applied magnetic field can significantly modify the spin-wave spectra. From the simulated results, we find that the spin-wave dynamics can be analyzed on three levels, namely on the levels of a single nanomagnet, magnetic unit cell, and large arrays. On the level of nanomagnet, the finite size of the nanomagnet is reflected in the spin-wave spectra by exhibiting three different modes, i.e., the edge modes, the bulk-like modes, and the higher order modes. When combining these building blocks in a magnetic unit cell, we find that the mode evolution is related to the symmetry of the system. Next, when examining the mode evolution from the magnetic unit cell to large arrays, we find several dominating modes that are always present, and they correspond to the eigenmodes in the magnetic unit cell. Such behavior well represents the feature of the crystal geometry. In addition, we find two modes whose behaviors depend on the array size, and we identify them as the array edge mode and the array bulk-like modes.

To continue our investigations on magnetic 2D structures, we then examine the fractal geometry. To reveal the special features of the mode formation in magnetic fractals, we characterize the precessional dynamics in two sample sets that are developed from a simple geometric structure towards a fractal-like structure. For triangle samples, where a triangle is developed towards a Sierpinski triangle, a uniform mode in each triangle is always present. For square samples, where a square is developed towards a Sierpinski carpet, a splitting of the frequency peaks and different mode distributions are observed. However, for the experimental observations of the fractal-like structures of iteration number up to 2, the role of the fractal geometry is not prominent. The unique feature of the fractal geometry is revealed by the simulated results for the structure with one further iteration. In particular, we find that the amplitude distribution of the magnetostatic mode is inclined to follow the geometric scaling to form scaled mode patterns in fractal-like structures with one more iteration. However, for this to occur, two conditions must be satisfied. The first is that the associated magnetic boundaries are scaled accordingly, and the second is that the local modes do not coincide with the regions for the edge modes. Here, it should be noted that all the arguments can only be applied to the magnetostatic modes. As a result, the magnetic fractals often exhibit a complex mode distribution. Nevertheless, with the method provided, one can reduce the complexity of the analysis by analyzing the modes in structures with one less iteration.

By comparing the precessional dynamics in magnetic crystal structures and magnetic fractal-like structures, we find the two types of mode formation regarding the spatial distribution of the modes, which are related to their distinctive symmetries. Here, we do not place emphasis on the mode frequency, since the scaling of the structure and adding unit cells can in general result in a frequency shift. For the crystal structure, the system possesses translation symmetry. The geometric equivalence of all unit cells means that the dominating modes for the whole array exhibit a similar amplitude distribution as that of the eigenmodes in the unit cell. In contrast, fractals do not have translation symmetry, but have dilation symmetry that defines the scaling relation of the different self-similar structures. Due to the lack of translation symmetry, the precessional dynamics in fractals cannot be effectively described using the eigenmodes in the base structures. Indeed, we find that the complexity of the precessional dynamics in fractals is related to the iteration process for fractal generation. For every iteration step, when the structure is scaled and repeated, the mode distribution is inclined to follow the geometric scaling to form a scaled pattern, but with certain modifications. Therefore, the precessional dynamics in fractal structures are the result of the combined contribution of all the structures on different length scales, and thus becomes very complex.

6.3. Outlook

6.3.1. Magnetic trilayers

In this thesis, we present a systematic characterization of the precessional dynamics in magnetic trilayers. To facilitate the understanding, we present the perspective of analyzing the dynamics by considering a competition between the Zeeman energy and the energy associated with the interlayer coupling.

Following the precessional dynamics in magnetic trilayers, it would be interesting to characterize the propagating spin waves in these systems. As introduced in Chapter 3, such a trilayer film with an antiferromagnetic coupling is particularly interesting because of the nonreciprocal dispersion relation for the Damon-Eschbach mode. In order to achieve the nonreciprocity, many challenging problems need to be solved. In Chapter 3, we presented our TRSKM measurements for such magnetic trilayers, where we did not observe propagating spin waves. We pointed out two possible problems, which are the complex domain structure and the large damping. An easy solution would be to increase the applied magnetic field to obtain a single domain in each layer. However, the large magnetic field can compensate the antiparallel alignment of the two magnetizations, which can subsequently result in a reciprocal dispersion. Therefore, one must achieve a balance between the exchange coupling and the applied magnetic field. Another factor that determines the spin-wave nonreciprocity is the amplitude localization of the Damon-Eschbach mode. As introduced in Chapter 1, the decay factor of the potential function is proportional to e^{-kd}, where k is the wavevector and d is the film thickness. Therefore, increasing both the film thickness and the wavevector of the spin wave can enhance the nonreciprocity. However, there are again limitations. The first concerns the wavevector, because the increase of the wavevector requires both a higher imaging resolution and higher frequencies for the RF electronics, neither of which are trivial in terms of performing experiments. The second concerns the film thickness. Because the interlayer coupling is an interface effect, increasing the film thickness is equivalent to reducing the average coupling strength. Therefore, to achieve a pronounced nonreciprocal effect, one needs to consider all the factors mentioned above, and keep in mind that they are dependent on each other.

Finally, it should be noted that the magnetic trilayer with RKKY interaction is only one of the many methods for tuning the magnetic interactions via the interface. Other interfacial effects can also be used to tune the interactions, such as the interfacial Dzyaloshinskii-Moriya interaction [210, 211] and the tunable magnetic anisotropy at a ferromagnetic/ferroelectric interface [212].

6.3.2. Magnetic 2D structures

In this thesis, we present two studies of the precessional dynamics in magnetic 2D structures with crystal and fractal geometries. We find the associated translation symmetry and dilation symmetry determine two different mechanisms for the mode formation. For the crystal geometry, the dynamics is dominated by the eigenmodes in the unit cell, whereas for the fractal geometry, the dynamics resemble features of all the structures in the fractal hierarchy.

Following the measurement of the precessional dynamics, it would be interesting to study the spin-wave dispersion relation in these 2D structures. For the trident ice, it is expected that a spin-wave band structure will be formed. Nevertheless, one can focus on the anisotropic magnetostatic interactions, and determine how this will influence the band structure. Moreover, it would be interesting to investigate the dependence of the spin-wave behavior in trident ice on the geometric parameters that are used to tune the frustration such as the intermagnet distances and distances between unit cells. In this way, one can investigate how the magnetic frustration can modify the spin-wave bands. In addition, one should not be limited to the crystal structure generated from nanomagnet arrays, and can think of other types of magnonic crystals, such as antidot arrays and bicomponent magnonic crystals, which can form more collective dynamics [112, 213–215].

For magnetic fractals, it is not so straightforward to understand how the corresponding dispersion relations will form due to the lack of translation symmetry. Nevertheless, the order of the structures and the related symmetries should be reflected in the dispersion relations. For example, an interesting point would be to study the spin waves whose wavelengths correspond to the different length scales of the fractals. In this way, one can examine whether these spin waves can exhibit self-similar behaviors or not, following the self-similarity of the fractals. Moreover, the fractal dimension can be an interesting point for investigations. More specifically, the coverage area for the fractals scales proportionally to L^{D}, where L is the length of the fractal pattern, and D is the fractal dimension. If one can find some relevant quantities of spin waves that have such a dependence, this could be a unique feature for spin waves in magnetic fractals. Finally, one should note that all the arguments regarding magnetic fractals are discussed in the context of magnetostatic modes. Following this, an interesting research perspective would be to study the evolution of the dynamics from a magnetostatic dominated regime into an exchange dominated regime by decreasing the size of the patterns, and determine the differences of the dynamics in these two regimes.

A. Appendix

A.1. Characterization of TRSKM setup

We present here two supplementary characterizations for the TRSKM setup. The first one is the characterization of the synchronization between the laser pulse and the RF current. The second is the characterization of the laser beam spot size.

The synchronization for the TRSKM setup is a prerequisite for any types of TRSKM measurements. To verify the synchronization, the laser pulse is first detected by a fast response photodiode. Subsequently, both signals of the photodiode and RF current are measured simultaneously via two channels of an oscilloscope. For real-time measurement, both signals are continuously monitored over time. When a synchronization is achieved, the relative position between the two signals in time domain should be fixed as the result shown in Fig. A.1.

Another important characterization of the TRSKM setup is the size of the laser spot. This is important for determining the spatial resolution for the setup. This characterization is performed by scanning the laser along a SiN membrane edge, where the reflectivity is measured as a function of the X piezo stage movement.

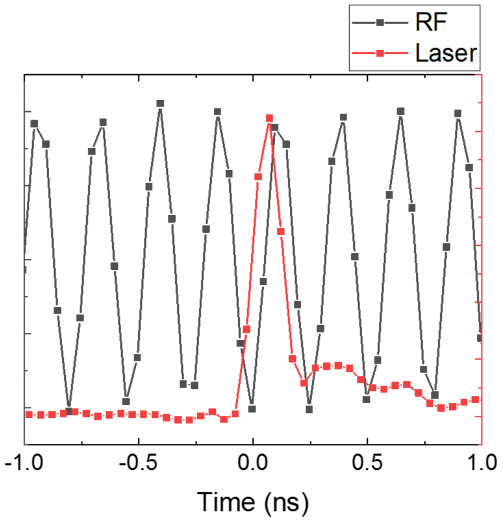

Figure A.1. Synchronization verification using two signals from the laser and RF current.

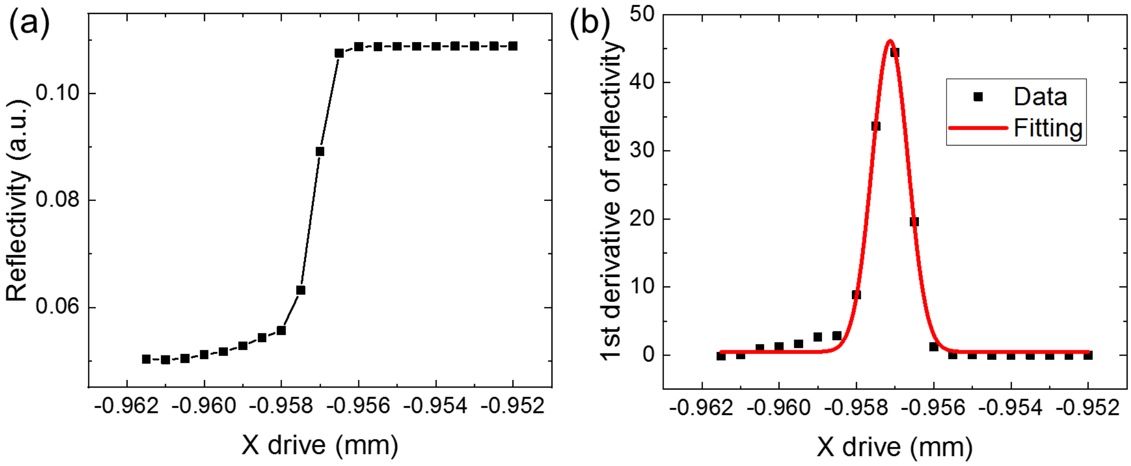

Figure A.2. Characterization of the laser spot size.

From Fig. A.2 (a), it can be seen that there is a sharp change in the reflectivity signal, which corresponds the position of the edge of the membrane. To extract the size of the laser spot, the first derivative of the reflectivity signal with respect to X is determined. The result [see Fig. A.2(b)] is subsequently fitted with a Gaussian peak, whose full width at half maximum is taken as the approximate size of the laser. In this case, the laser spot size is $\sim 1.1\ \mu$m.

A.2. Calculation of precessional dynamics

We present here the detailed formalism to determine the precessional dynamics based on the coupled LLG equations. We solve the dynamics for the asymmetric sample with $t_1 = 2t_2 = 2t$, where the solutions are presented in Sec. 3.2.2.

First, the precession part of the LLG equation is rearranged to give:

$$\frac{\mathrm{d}\mathbf{M}_j}{\mathrm{d}t} + \gamma\mu_0\mathbf{M}_j \times \mathbf{H}_j^{\mathrm{eff}} = 0. \tag{A.1}$$

To solve this, we need to find the expressions for $\mathbf{M}_j$ and $\mathbf{H}_j^{\mathrm{eff}}$. The three vector components of $\mathbf{M}_j$ in terms of θ_j are expressed as follows

$$\begin{aligned}\mathbf{M}_j(t) &= \mathbf{M}_j^{\mathrm{S}} + \mathbf{m}_j(t)\\ &= (M\cos\theta_j, M\sin\theta_j, 0) + e^{i\omega t}(m_{jx}, m_{jy}, m_{jz}).\end{aligned} \tag{A.2}$$

Here, the magnetization is divided to the static and dynamic parts, with the dynamic part having a time dependence of $e^{i\omega t}$. For the total effective field, we consider the contribution from the applied magnetic field, the demagnetization field, and the effective field from the IEC as follows

$$
\begin{aligned}
\mathbf{H}_j^{\mathrm{eff}} &= \mathbf{H}_j^{\mathrm{Z}} + \mathbf{H}_j^{\mathrm{D}} + \mathbf{H}_j^{\mathrm{IEC}}, \text{where} \\
\mathbf{H}_j^{\mathrm{Z}} &= (H, 0, 0), \\
\mathbf{H}_j^{\mathrm{D}} &= (0, 0, -m_{jz}), \\
\mathbf{H}_1^{\mathrm{IEC}} &= (-\frac{A}{2}m_{2x} - \frac{A}{2}M\cos\theta_2, -\frac{A}{2}m_{2y} - \frac{A}{2}M\sin\theta_2, \\
&\quad -\frac{A}{2}m_{2z}), \\
\mathbf{H}_2^{\mathrm{IEC}} &= (-Am_{1x} - AM\cos\theta_1, -Am_{1y} - AM\sin\theta_1, \\
&\quad - Am_{1z}),
\end{aligned}
\tag{A.3}
$$

Here, $A = J/(\mu_0 t M^2)$, and $\mathbf{H}_j^{\mathrm{IEC}}$ corresponds to the effective field of the IEC for two FM layers of different thicknesses.

By linearizing Eq. (A.1) with the expressions from Eqs. (A.2) and (A.3), we obtain a system of linear equations with the following form

$$
\begin{aligned}
\gamma\mu_0 L\mathbf{m}^{\mathrm{T}} &= \mathbf{c}, \\
\mathbf{m} &= (m_{1x}, m_{1y}, m_{1z}, m_{2x}, m_{2y}, m_{2z}).
\end{aligned}
\tag{A.4}
$$

where $\mathbf{c}$ is a constant vector and L is a 6×6 matrix expressed as follows

$$
\begin{bmatrix}
i\omega/\gamma\mu_0 & 0 & -M\sin\theta_1 + \frac{A}{2}M\sin\theta_2 & 0 & 0 & -\frac{A}{2}M\sin\theta_1 \\
0 & i\omega/\gamma\mu_0 & H + M\cos\theta_1 - \frac{A}{2}M\cos\theta_2 & 0 & 0 & \frac{A}{2}M\cos\theta_1 \\
-\frac{A}{2}M\sin\theta_2 & -H + \frac{A}{2}M\cos\theta_2 & i\omega/\gamma\mu_0 & \frac{A}{2}M\sin\theta_1 & -\frac{A}{2}M\cos\theta_1 & 0 \\
0 & 0 & -AM\sin\theta_2 & i\omega/\gamma\mu_0 & AM\sin\theta_1 - M\sin\theta_2 & 0 \\
0 & 0 & AM\cos\theta_2 & 0 & i\omega/\gamma\mu_0 & H - AM\cos\theta_1 + M\cos\theta_2 \\
AM\sin\theta_2 & -AM\cos\theta_2 & 0 & -AM\sin\theta_1 & -H + AM\cos\theta_1 & i\omega/\gamma\mu_0
\end{bmatrix}
\tag{A.5}
$$

For Eq. (A.4), in order to have a nonzero solution of $\mathbf{m}$, we set the determinant of L to zero and solve for ω. For the case where ω can be solved analytically, solutions of ω are inserted back into matrix L to obtain the solution of $\mathbf{m}$. From the expression of $\mathbf{m}$, the phase information of the two m_z components can be obtained. For the case where ω has to be solved numerically, the general solution for $\mathbf{m}$ cannot be obtained. This is because any numerical values of ω are not the exact solutions for $det|L| = 0$. Therefore, if the numerical values of ω are inserted back into the matrix, $det|L|$ will become non-zero, which cannot provide a non-zero solution of $\mathbf{m}$.

A.3. Supplementary figures for Chapter 5

In this section, we present the supplementary figures for Chapter 5.

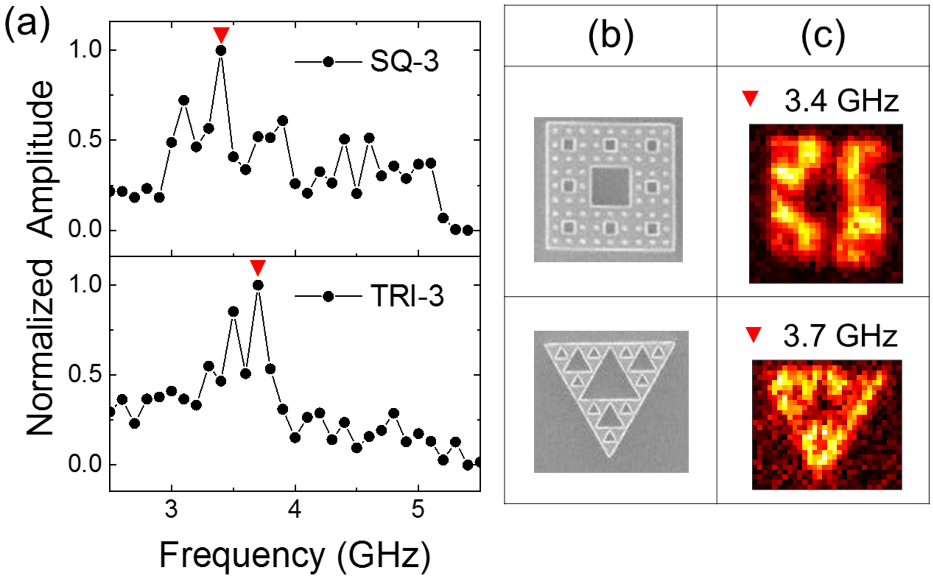

Figure A.3. TRSKM measurements of samples SQ-3 and TRI-3. (a) Frequency spectra of samples SQ-3 and TRI-3. (b) SEM images of the two samples. (c) Normalized scanning Kerr images of the different modes for the two samples. The modes are indicated by the red markers in (a).

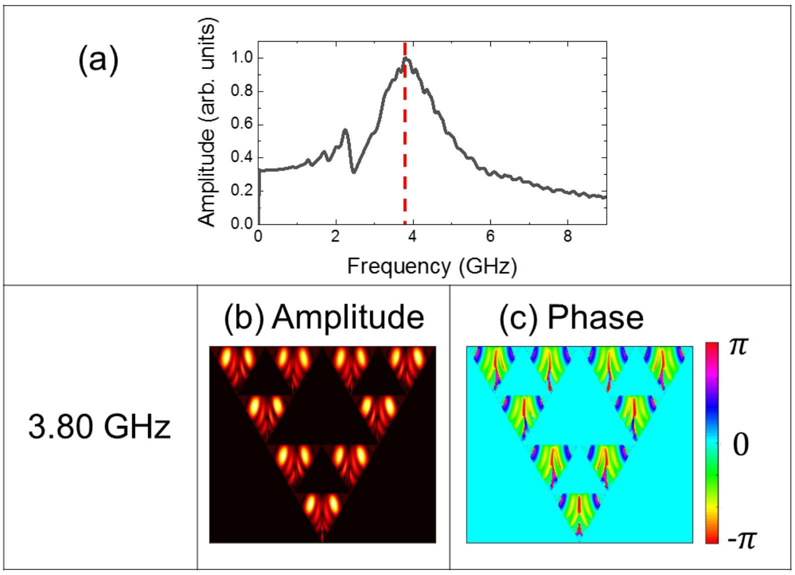

Figure A.4. Simulated (a) frequency spectrum, (b) amplitude distribution and (c) phase distribution of the main mode in TRI-2, which is indicated by the dashed line in (a).

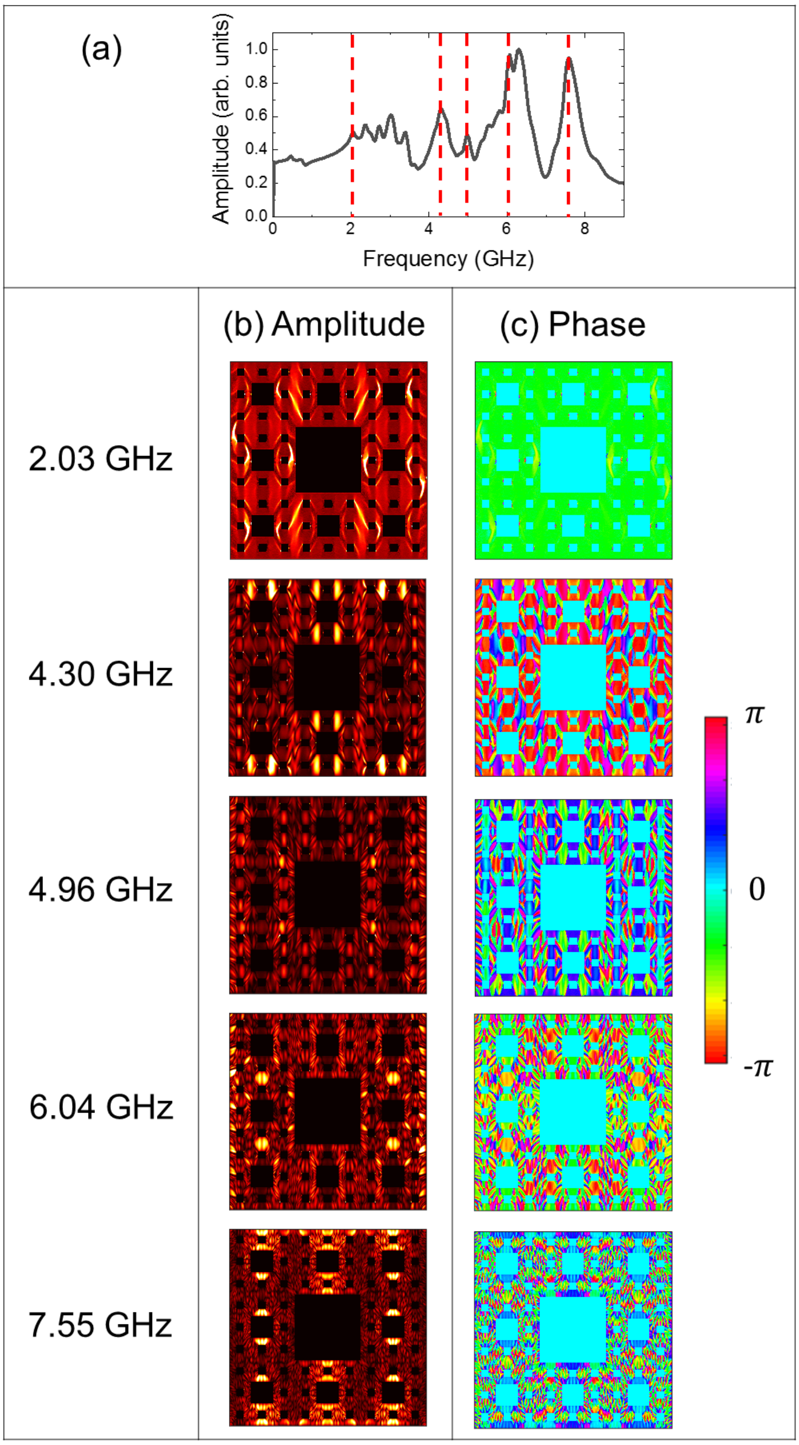

Figure A.5. Simulated (a) frequency spectrum, (b) amplitude distribution and (c) Phase distribution of the five modes in SQ-3, which are indicated by the dashed lines in (a).

Acknowledgements

Here, I would like to take the opportunity to express my thanks and gratitude to all the people who have helped me during my four years of PhD study and research.

To Professor Laura Heyderman, thank you for giving me the opportunity to come to PSI to conduct my PhD research. I am very grateful that you have taught me the importance of planning experiments and time management, which helped me establish a good research habit for the long term. Thank you for all the discussions and suggestions on my research projects during the coffee catch ups, from which I benefited a lot. With your help, I have also made some progress in scientific writing, which, of course, I am still working on. Thank you very much for everything.

To Susmita Saha, thank you very much for your daily supervision and advice. I am truly impressed by your passion into science, in particular, magnonics, which strongly motivates me when I am working with you. I want to thank you for all the discussions that we had on the scientific topics almost every week, from which I benefited a lot.

To Valerio Scagnoli, thank you for always being there to discuss with me on some “random” questions. Especially your emphasis on the error bars, which had me noticed many problems regarding our experimental setup and my measurement results. Thank you very much.

To Professor Pietro Gambardella, thank you for your supervision on my final year of my PhD, and your recommendations of the textbooks related to magnetism.

A big thanks to PSI, which made me feel like I am in a big research group where I can ask for help and exchange ideas from different people. I want to thank Jörg Raabe and Simone Finizio for guiding me developed our experimental setup. To Alexander Dietrich and Stefan Mair, thank you very much for helping me with the technical problems on microwaves. To Sebastian Wintz, thank you very much for the discussions on spin waves, which I have learned a lot. To Sebastian Gliga, thank you very much for the discussion on artificial spin ices and the proofreading, which I have learned a lot. To everyone in LMN, thank you for helping me with the work in the cleanroom and process labs. I would like to thank Vitaliy Guzenko for the helps on electron-beam lithography, Thomas Neiger for helping me with the cooling system for our laser, Dario Marty for your introductions to many of the equipments in the cleanroom, and Christopher Wild and Jana Lehmann for many practical problems. To everyone in LMX, it is a great pleasure to listen to the talks where we can exchange ideas on different research topics every month.

To Mesosys group, thanks for being there for me whenever I need some help related either to research or daily life. I would like to thank Eugenie Kirk, Laura Maurel, Naëmi Leo, Aleš Hrabec, and Anja Weber for introducing me the different experimental equipments both in our labs and in the cleanroom. To Zhaochu Luo, thank you very much for helping me prepare the samples with the e-beam. Without your help, my samples would not have been ready so fast. To Sergii Parchenko and Michael Grimes, thank you very much for helping me solve the different problems with our laser system. To Peter Derlet, thank you for your help with the analytic calculations, and many discussions on my research results. To Namrata Gurung, Kevin Hofhuis, Sina Mayr, Phuong Dao, Testa Paolo, Zhentao Liu, Petai Pip, Aleksandra Pac and Samuel Treves, it is my great pleasure to work with you and thanks for all the scientific discussions, as well as the daily conservations on our PhD life. To Jizhai Cui, thanks for constantly reminding me to think about the meaning of life, and your helps on broadening my view on magnetism related applications. To Michael Grimes, Rhea Stewart, and Sina Mayr, thank you for the proofreading for my thesis. To Margit Braun-Shea, thanks to your help with all the administrative works. Finally, to all the group members, thank you all for the time at the group lunches, BBQs and the group retreats that we enjoyed together, as well as all the virtual meetings that we had during the pandemic, which have supported all of us to overcome this difficult time.

To our external collaborators, Mateusz Zelent and Professor Maciej Krawczyk, thank you for helping me with the micromagnetic simulations, and the fruitful discussion on magnetic fractals.

I would like to thank my friends and my family for always being there and giving me support. Thank you very much. Finally, I would like to acknowledge the funding agency for my PhD project, the Swiss National Science Foundation (Project Number: 200020_172774).

References

[1] J. Cui et al., “Nanomagnetic encoding of shape-morphing micromachines”, Nature **575**, 164–168 (2019).

[2] C. Pawashe, S. Floyd, and M. Sitti, “Modeling and experimental characterization of an untethered magnetic micro-robot”, The International Journal of Robotics Research **28**, 1077–1094 (2009).

[3] F. Tâche, W. Fischer, G. Caprari, R. Siegwart, R. Moser, and F. Mondada, “Magnebike: A magnetic wheeled robot with high mobility for inspecting complex-shaped structures”, Journal of Field Robotics **26**, 453–476 (2009).

[4] L. Landau and E. Lifshitz, “On the theory of the dispersion of magnetic permeability in ferromagnetic bodies”, in *Perspectives in Theoretical Physics* (Elsevier, 1992), pp. 51–65.

[5] J. Raabe, C. Quitmann, C. H. Back, F. Nolting, S. Johnson, and C. Buehler, “Quantitative analysis of magnetic excitations in Landau flux-closure structures using synchrotron-radiation microscopy”, Physical Review Letters **94**, 217204 (2005).

[6] T. Shinjo, T. Okuno, R. Hassdorf, K. Shigeto, and T. Ono, “Magnetic vortex core observation in circular dots of permalloy”, Science **289**, 930–932 (2000).

[7] Y. Acremann, C. H. Back, M. Buess, O. Portmann, A. Vaterlaus, D. Pescia, and H. Melchior, “Imaging precessional motion of the magnetization vector”, Science **290**, 492–495 (2000).

[8] B. Kalinikos, “Excitation of propagating spin waves in ferromagnetic films”, in IEE Proceedings H (Microwaves, Optics and Antennas), Vol. 127, 1 (IET, 1980), pp. 4–10.

[9] M. Covington, T. Crawford, and G. Parker, “Time-resolved measurement of propagating spin waves in ferromagnetic thin films”, Physical Review Letters **89**, 237202 (2002).

[10] G. Beach, M. Tsoi, and J. Erskine, “Current-induced domain wall motion”, Journal of magnetism and magnetic materials **320**, 1272–1281 (2008).

[11] G. Tatara and H. Kohno, “Theory of current-driven domain wall motion: Spin transfer versus momentum transfer”, Physical review letters **92**, 086601 (2004).

[12] S. Zhang, P. Levy, and A. Fert, “Mechanisms of spin-polarized current-driven magnetization switching”, Physical review letters **88**, 236601 (2002).

[13] K. Garello et al., “Ultrafast magnetization switching by spin-orbit torques”, Applied Physics Letters **105**, 212402 (2014).

[14] S. Fukami, C. Zhang, S. DuttaGupta, A. Kurenkov, and H. Ohno, “Magnetization switching by spin–orbit torque in an antiferromagnet–ferromagnet bilayer system”, Nature materials **15**, 535–541 (2016).

[15] M. Kostylev, A. Serga, T. Schneider, B. Leven, and B. Hillebrands, “Spin-wave logical gates”, Applied Physics Letters **87**, 153501 (2005).

[16] T. Schneider, A. A. Serga, B. Leven, B. Hillebrands, R. L. Stamps, and M. P. Kostylev, “Realization of spin-wave logic gates”, Applied Physics Letters **92**, 022505 (2008).

[17] S. S. Parkin, M. Hayashi, and L. Thomas, “Magnetic domain-wall racetrack memory”, Science **320**, 190–194 (2008).

[18] M. Hosomi et al., “A novel nonvolatile memory with spin torque transfer magnetization switching: Spin-RAM”, in IEEE InternationalElectron Devices Meeting, 2005. IEDM Technical Digest. (IEEE, 2005), pp. 459–462.

[19] F. A. Bovey, P. A. Mirau, and H. Gutowsky, *Nuclear magnetic resonance spectroscopy* (Elsevier, 1988).

[20] J. A. Weil and J. R. Bolton, *Electron paramagnetic resonance: elementary theory and practical applications* (John Wiley & Sons, 2007).

[21] S. A. Huettel, A. W. Song, G. McCarthy, et al., *Functional magnetic resonance imaging*, Vol. 1 (Sinauer Associates Sunderland, MA, 2004).

[22] V. Kruglyak, S. Demokritov, and D. Grundler, “Magnonics”, Journal of Physics D: Applied Physics **43**, 264001 (2010).

[23] O. Semenov, A. Vassighi, and M. Sachdev, “Impact of self-heating effect on long-term reliability and performance degradation in CMOS circuits”, IEEE Transactions on Device and Materials Reliability **6**, 17–27 (2006).

[24] C. Prasad, S. Ramey, and L. Jiang, “Self-heating in advanced CMOS technologies”, in 2017 IEEE International Reliability Physics Symposium (IRPS) (IEEE, 2017), 6A–4.

[25] D. M. Pozar, *Microwave engineering* (John wiley & sons, 2011).

[26] B. E. Saleh and M. C. Teich, *Fundamentals of photonics* (john Wiley & sons, 2019).

[27] M. Maldovan, “Sound and heat revolutions in phononics”, Nature **503**, 209–217 (2013).

[28] M. Krawczyk and D. Grundler, "Review and prospects of magnonic crystals and devices with reprogrammable band structure", Journal of Physics: Condensed Matter **26**, 123202 (2014).

[29] P. Bruno and C. Chappert, "Oscillatory coupling between ferromagnetic layers separated by a nonmagnetic metal spacer", Physical review letters **67**, 1602 (1991).

[30] S. Parkin, N. More, and K. Roche, "Oscillations in exchange coupling and magnetoresistance in metallic superlattice structures: Co/Ru, Co/Cr, and Fe/Cr", Physical review letters **64**, 2304 (1990).

[31] D. Mosca, F. Petroff, A. Fert, P. Schroeder, W. Pratt Jr, and R. Laloee, "Oscillatory interlayer coupling and giant magnetoresistance in Co/Cu multilayers", Journal of magnetism and magnetic materials **94**, L1–L5 (1991).

[32] X. Liu, H. T. Nguyen, J. Ding, M. Cottam, and A. Adeyeye, "Interlayer coupling in Ni 80 Fe 20/Ru/Ni 80 Fe 20 multilayer films: Ferromagnetic resonance experiments and theory", Physical Review B **90**, 064428 (2014).

[33] R. W. Damon and J. Eshbach, "Magnetostatic modes of a ferromagnet slab", Journal of Physics and Chemistry of Solids **19**, 308–320 (1961).

[34] R. Gallardo et al., "Reconfigurable spin-wave nonreciprocity induced by dipolar interaction in a coupled ferromagnetic bilayer", Physical Review Applied **12**, 034012 (2019).

[35] K. Di, S. Feng, S. Piramanayagam, V. Zhang, H. S. Lim, S. C. Ng, and M. H. Kuok, "Enhancement of spin-wave nonreciprocity in magnonic crystals via synthetic antiferromagnetic coupling", Scientific reports **5**, 1–6 (2015).

[36] A. Farhan et al., "Nanoscale control of competing interactions and geometrical frustration in a dipolar trident lattice", Nature communications **8**, 1–7 (2017).

[37] J. Feder, *Fractals* (Springer Science & Business Media, 2013).

[38] T. Nakayama and K. Yakubo, *Fractal concepts in condensed matter physics*, Vol. 140 (Springer Science & Business Media, 2003).

[39] J. D. Jackson, *Classical electrodynamics*, 1999.

[40] M. Bezerra, W. Kort-Kamp, M. Cougo-Pinto, and C. Farina, "How to introduce the magnetic dipole moment", European journal of physics **33**, 1313 (2012).

[41] J. S. Townsend, *A modern approach to quantum mechanics* (University Science Books, 2000).

[42] P. W. Anderson, "New approach to the theory of superexchange interactions", Physical Review **115**, 2 (1959).

[43] P. W. Anderson, "Antiferromagnetism. Theory of superexchange interaction", Physical Review **79**, 350 (1950).

[44] M. A. Ruderman and C. Kittel, "Indirect exchange coupling of nuclear magnetic moments by conduction electrons", Physical Review **96**, 99 (1954).

[45] T. Kasuya, "A theory of metallic ferro-and antiferromagnetism on Zener's model", Progress of theoretical physics **16**, 45–57 (1956).

[46] K. Yosida, "Magnetic properties of Cu-Mn alloys", Physical Review **106**, 893 (1957).

[47] T. Moriya, "Anisotropic superexchange interaction and weak ferromagnetism", Physical review **120**, 91 (1960).

[48] I. Dzyaloshinsky, "A thermodynamic theory of "weak" ferromagnetism of antiferromagnetics", Journal of Physics and Chemistry of Solids **4**, 241–255 (1958).

[49] P. Ferriani et al., "Atomic-scale spin spiral with a unique rotational sense: Mn monolayer on W (001)", Physical review letters **101**, 027201 (2008).

[50] S. Meckler, N. Mikuszeit, A. Preßler, E. Vedmedenko, O. Pietzsch, and R. Wiesendanger, "Real-space observation of a right-rotating inhomogeneous cycloidal spin spiral by spin-polarized scanning tunneling microscopy in a triple axes vector magnet", Physical review letters **103**, 157201 (2009).

[51] S. Rohart and A. Thiaville, "Skyrmion confinement in ultrathin film nanostructures in the presence of Dzyaloshinskii-Moriya interaction", Physical Review B **88**, 184422 (2013).

[52] G. Daalderop, P. Kelly, and M. Schuurmans, "Magnetocrystalline anisotropy and orbital moments in transition-metal compounds", Physical Review B **44**, 12054 (1991).

[53] G. van der Laan, "Microscopic origin of magnetocrystalline anisotropy in transition metal thin films", Journal of Physics: Condensed Matter **10**, 3239 (1998).

[54] J. M. Coey, *Magnetism and magnetic materials* (Cambridge university press, 2010).

[55] E. Beaurepaire, J.-C. Merle, A. Daunois, and J.-Y. Bigot, "Ultrafast spin dynamics in ferromagnetic nickel", Physical review letters **76**, 4250 (1996).

[56] A. Scholl, L. Baumgarten, R. Jacquemin, and W. Eberhardt, "Ultrafast spin dynamics of ferromagnetic thin films observed by fs spin-resolved two-photon photoemission", Physical review letters **79**, 5146 (1997).

[57] H.-S. Rhie, H. Dürr, and W. Eberhardt, "Femtosecond Electron and Spin Dynamics in N i/W (110) Films", Physical review letters **90**, 247201 (2003).

[58] C. Stamm et al., “Femtosecond modification of electron localization and transfer of angular momentum in nickel”, Nature materials **6**, 740–743 (2007).

[59] G. Zhang and W. Hübner, “Laser-induced ultrafast demagnetization in ferromagnetic metals”, Physical Review Letters **85**, 3025 (2000).

[60] B. Koopmans, J. Ruigrok, F. Dalla Longa, and W. De Jonge, “Unifying ultrafast magnetization dynamics”, Physical review letters **95**, 267207 (2005).

[61] M. Battiato, K. Carva, and P. M. Oppeneer, “Superdiffusive spin transport as a mechanism of ultrafast demagnetization”, Physical review letters **105**, 027203 (2010).

[62] A. Eschenlohr et al., “Ultrafast spin transport as key to femtosecond demagnetization”, Nature materials **12**, 332–336 (2013).

[63] J. H. Griffiths, “Anomalous high-frequency resistance of ferromagnetic metals”, Nature **158**, 670–671 (1946).

[64] J. Gouzerh, A. Stashkevich, N. Kovshikov, V. Matyushev, and J. Desvignes, “Reflection of magnetostatic waves from a laser-annealed grating in a garnet film”, Journal of magnetism and magnetic materials **101**, 189–190 (1991).

[65] A. V. Vashkovskii and E. H. Lokk, “Negative refractive index for a surface magnetostatic wave propagating through the boundary between a ferrite and ferrite-insulator-metal media”, Physics-Uspekhi **47**, 601 (2004).

[66] J. Stigloher et al., “Snell’s law for spin waves”, Physical review letters **117**, 037204 (2016).

[67] J. Podbielski, F. Giesen, and D. Grundler, “Spin-wave interference in microscopic rings”, Physical review letters **96**, 167207 (2006).

[68] K. Perzlmaier, G. Woltersdorf, and C. H. Back, “Observation of the propagation and interference of spin waves in ferromagnetic thin films”, Physical Review B **77**, 054425 (2008).

[69] S. Mansfeld, J. Topp, K. Martens, J. Toedt, W. Hansen, D. Heitmann, and S. Mendach, “Spin wave diffraction and perfect imaging of a grating”, Physical Review Letters **108**, 047204 (2012).

[70] O. Büttner et al., “Linear and nonlinear diffraction of dipolar spin waves in yttrium iron garnet films observed by space-and time-resolved Brillouin light scattering”, Physical Review B **61**, 11576 (2000).

[71] D. A. Allwood, G. Xiong, C. Faulkner, D. Atkinson, D. Petit, and R. Cowburn, “Magnetic domain-wall logic”, Science **309**, 1688–1692 (2005).

[72] Z. Luo et al., “Current-driven magnetic domain-wall logic”, Nature **579**, 214–218 (2020).

[73] T. Gilbert, “Equation of motion of magnetization”, Armour Research Foundation Rep. **11** (1955).

[74] M. C. Hickey and J. S. Moodera, “Origin of intrinsic Gilbert damping”, Physical review letters **102**, 137601 (2009).

[75] R. Urban, G. Woltersdorf, and B. Heinrich, “Gilbert damping in single and multilayer ultrathin films: Role of interfaces in nonlocal spin dynamics”, Physical review letters **87**, 217204 (2001).

[76] C. Tang et al., “Dirac surface state–modulated spin dynamics in a ferrimagnetic insulator at room temperature”, Science advances **4**, eaas8660 (2018).

[77] Y. Tserkovnyak, A. Brataas, G. E. Bauer, and B. I. Halperin, “Nonlocal magnetization dynamics in ferromagnetic heterostructures”, Reviews of Modern Physics **77**, 1375 (2005).

[78] G. Eilers, M. Luettich, and M. Münzenberg, “Giant nonlocal damping by spin-wave emission: Micromagnetic simulations”, Physical Review B **74**, 054411 (2006).

[79] K. Zakeri et al., “Spin dynamics in ferromagnets: Gilbert damping and two-magnon scattering”, Physical Review B **76**, 104416 (2007).

[80] A. Prabhakar and D. D. Stancil, *Spin waves: Theory and applications*, Vol. 5 (Springer, 2009).

[81] S. Vasiliev, V. Kruglyak, M. Sokolovskii, and A. Kuchko, “Spin wave interferometer employing a local nonuniformity of the effective magnetic field”, Journal of Applied Physics **101**, 113919 (2007).

[82] E. Samuelsen, R. Silberglitt, G. Shirane, and J. Remeika, “Spin Waves in Ferromagnetic Cr Br 3 Studied by Inelastic Neutron Scattering”, Physical Review B **3**, 157 (1971).

[83] H. Bohn, W. Zinn, B. Dorner, and A. Kollmar, “Neutron scattering study of spin waves and exchange interactions in ferromagnetic EuS”, Physical Review B **22**, 5447 (1980).

[84] M. Van Kampen, C. Jozsa, J. Kohlhepp, P. LeClair, L. Lagae, W. De Jonge, and B. Koopmans, “All-optical probe of coherent spin waves”, Physical review letters **88**, 227201 (2002).

[85] J. Slonczewski, “Excitation of spin waves by an electric current”, Journal of Magnetism and Magnetic Materials **195**, L261–L268 (1999).

[86] S. O. Demokritov, B. Hillebrands, and A. N. Slavin, “Brillouin light scattering studies of confined spin waves: linear and nonlinear confinement”, Physics Reports **348**, 441–489 (2001).

[87] H. Qin, S. J. Hämäläinen, K. Arjas, J. Witteveen, and S. Van Dijken, “Propagating spin waves in nanometer-thick yttrium iron garnet films: Dependence on wave vector, magnetic field strength, and angle”, Physical Review B **98**, 224422 (2018).

[88] H. Yu, G. Duerr, R. Huber, M. Bahr, T. Schwarze, F. Brandl, and D. Grundler, “Omnidirectional spin-wave nanograting coupler”, Nature communications **4**, 1–9 (2013).

[89] T. Satoh et al., “Directional control of spin-wave emission by spatially shaped light”, Nature Photonics **6**, 662–666 (2012).

[90] A. Kimel, A. Kirilyuk, P. Usachev, R. Pisarev, A. Balbashov, and T. Rasing, “Ultrafast non-thermal control of magnetization by instantaneous photomagnetic pulses”, Nature **435**, 655–657 (2005).

[91] M. Mansuripur, *The physical principles of magneto-optical recording* (Cambridge University Press, 1998).

[92] A. Stashkevich et al., “Experimental study of spin-wave dispersion in Py/Pt film structures in the presence of an interface Dzyaloshinskii-Moriya interaction”, Physical Review B **91**, 214409 (2015).

[93] T. Sebastian, K. Schultheiss, B. Obry, B. Hillebrands, and H. Schultheiss, “Micro-focused Brillouin light scattering: imaging spin waves at the nanoscale”, Frontiers in Physics **3**, 35 (2015).

[94] V. E. Demidov, S. Urazhdin, and S. O. Demokritov, “Direct observation and mapping of spin waves emitted by spin-torque nano-oscillators”, Nature materials **9**, 984–988 (2010).

[95] F. Fohr, A. Serga, T. Schneider, J. Hamrle, and B. Hillebrands, “Phase sensitive Brillouin scattering measurements with a novel magneto-optic modulator”, Review of Scientific Instruments **80**, 043903 (2009).

[96] C. Bayer et al., “Spin-wave excitations in finite rectangular elements of Ni 80 Fe 20”, Physical Review B **72**, 064427 (2005).

[97] C. Bayer et al., “Spin-wave excitations in finite rectangular elements”, Spin dynamics in confined magnetic structures III, 57–103 (2006).

[98] K. Y. Guslienko and A. N. Slavin, “Magnetostatic Green’s functions for the description of spin waves in finite rectangular magnetic dots and stripes”, Journal of magnetism and magnetic materials **323**, 2418–2424 (2011).

[99] S. O. Demokritov, V. E. Demidov, O. Dzyapko, G. A. Melkov, A. A. Serga, B. Hillebrands, and A. N. Slavin, “Bose–Einstein condensation of quasi-equilibrium magnons at room temperature under pumping”, Nature **443**, 430–433 (2006).

[100] S. M. Rezende, "Theory of coherence in Bose-Einstein condensation phenomena in a microwave-driven interacting magnon gas", Physical Review B **79**, 174411 (2009).

[101] V. Demidov, O. Dzyapko, S. Demokritov, G. Melkov, and A. Slavin, "Thermalization of a parametrically driven magnon gas leading to Bose-Einstein condensation", Physical review letters **99**, 037205 (2007).

[102] T. Giamarchi, C. Rüegg, and O. Tchernyshyov, "Bose–Einstein condensation in magnetic insulators", Nature Physics **4**, 198–204 (2008).

[103] C. Hauser et al., "Yttrium iron garnet thin films with very low damping obtained by recrystallization of amorphous material", Scientific reports **6**, 1–8 (2016).

[104] A. Serga, A. Chumak, and B. Hillebrands, "YIG magnonics", Journal of Physics D: Applied Physics **43**, 264002 (2010).

[105] S. Mizukami, D. Watanabe, M. Oogane, Y. Ando, Y. Miura, M. Shirai, and T. Miyazaki, "Low damping constant for Co 2 FeAl Heusler alloy films and its correlation with density of states", Journal of Applied Physics **105**, 07D306 (2009).

[106] Z. Zhang et al., "Ultralow Gilbert damping in CrO 2 epitaxial films", Physical Review B **102**, 014454 (2020).

[107] R. Weber, D.-S. Han, I. Boventer, S. Jaiswal, R. Lebrun, G. Jakob, and M. Kläui, "Gilbert damping of CoFe-alloys", Journal of Physics D: Applied Physics **52**, 325001 (2019).

[108] D.-S. Wang et al., "High thermal stability and low Gilbert damping constant of CoFeB/MgO bilayer with perpendicular magnetic anisotropy by Al capping and rapid thermal annealing", Applied Physics Letters **104**, 142402 (2014).

[109] S. Saha et al., "Control of damping in perpendicularly magnetized thin films using spin-orbit torques", Physical Review B **101**, 224401 (2020).

[110] Z. Wang, V. Zhang, H. Lim, S. Ng, M. Kuok, S. Jain, and A. Adeyeye, "Observation of frequency band gaps in a one-dimensional nanostructured magnonic crystal", Applied Physics Letters **94**, 083112 (2009).

[111] A. Chumak, A. Serga, B. Hillebrands, and M. Kostylev, "Scattering of backward spin waves in a one-dimensional magnonic crystal", Applied Physics Letters **93**, 022508 (2008).

[112] H. Ulrichs, B. Lenk, and M. Münzenberg, "Magnonic spin-wave modes in CoFeB antidot lattices", Applied Physics Letters **97**, 092506 (2010).

[113] A. Serga, T. Neumann, A. Chumak, and B. Hillebrands, “Generation of spin-wave pulse trains by current-controlled magnetic mirrors”, Applied Physics Letters **94**, 112501 (2009).

[114] A. Chumak, A. Serga, and B. Hillebrands, “Magnonic crystals for data processing”, Journal of Physics D: Applied Physics **50**, 244001 (2017).

[115] S.-K. Kim, K.-S. Lee, and D.-S. Han, “A gigahertz-range spin-wave filter composed of width-modulated nanostrip magnonic-crystal waveguides”, Applied Physics Letters **95**, 082507 (2009).

[116] Y. Au, M. Dvornik, O. Dmytriiev, and V. Kruglyak, “Nanoscale spin wave valve and phase shifter”, Applied Physics Letters **100**, 172408 (2012).

[117] A. Serga, A. Chumak, A. André, G. Melkov, A. Slavin, S. Demokritov, and B. Hillebrands, “Parametrically stimulated recovery of a microwave signal stored in standing spin-wave modes of a magnetic film”, Physical review letters **99**, 227202 (2007).

[118] A. Khitun, M. Bao, and K. L. Wang, “Magnonic logic circuits”, Journal of Physics D: Applied Physics **43**, 264005 (2010).

[119] A. Khitun and K. L. Wang, “Nano scale computational architectures with spin wave bus”, Superlattices and Microstructures **38**, 184–200 (2005).

[120] M. Jamali, J. H. Kwon, S.-M. Seo, K.-J. Lee, and H. Yang, “Spin wave nonreciprocity for logic device applications”, Scientific reports **3**, 1–5 (2013).

[121] J. Zhou, S. Saha, Z. Luo, E. Kirk, V. Scagnoli, and L. J. Heyderman, “Ultrafast laser induced precessional dynamics in antiferromagnetically coupled ferromagnetic thin films”, Physical Review B **101**, 214434 (2020).

[122] M. N. Baibich et al., “Giant magnetoresistance of (001) Fe/(001) Cr magnetic superlattices”, Physical review letters **61**, 2472 (1988).

[123] P. Grünberg, R. Schreiber, Y. Pang, M. Brodsky, and H. Sowers, “Layered magnetic structures: Evidence for antiferromagnetic coupling of Fe layers across Cr interlayers”, Physical review letters **57**, 2442 (1986).

[124] J. Daughton, J. Brown, E. Chen, R. Beech, A. Pohm, and W. Kude, “Magnetic field sensors using GMR multilayer”, IEEE Transactions on magnetics **30**, 4608–4610 (1994).

[125] J. Daughton, “GMR applications”, Journal of Magnetism and Magnetic Materials **192**, 334–342 (1999).

[126] S. Tehrani, J. Slaughter, E. Chen, M. Durlam, J. Shi, and M. DeHerren, “Progress and outlook for MRAM technology”, IEEE Transactions on Magnetics **35**, 2814–2819 (1999).

[127] R. Duine, K.-J. Lee, S. S. Parkin, and M. D. Stiles, “Synthetic antiferromagnetic spintronics”, Nature physics **14**, 217–219 (2018).

[128] H. Saarikoski, H. Kohno, C. H. Marrows, and G. Tatara, "Current-driven dynamics of coupled domain walls in a synthetic antiferromagnet", Physical Review B **90**, 094411 (2014).

[129] R. Lavrijsen, J.-H. Lee, A. Fernández-Pacheco, D. C. Petit, R. Mansell, and R. P. Cowburn, "Magnetic ratchet for three-dimensional spintronic memory and logic", Nature **493**, 647–650 (2013).

[130] T. Dohi, S. DuttaGupta, S. Fukami, and H. Ohno, "Formation and current-induced motion of synthetic antiferromagnetic skyrmion bubbles", Nature communications **10**, 1–6 (2019).

[131] T. Vemulkar, R. Mansell, A. Fernández-Pacheco, and R. Cowburn, "Toward flexible spintronics: Perpendicularly magnetized synthetic antiferromagnetic thin films and nanowires on polyimide substrates", Advanced Functional Materials **26**, 4704–4711 (2016).

[132] T. Vemulkar, R. Mansell, D. Petit, R. Cowburn, and M. Lesniak, "Highly tunable perpendicularly magnetized synthetic antiferromagnets for biotechnology applications", Applied Physics Letters **107**, 012403 (2015).

[133] Y. Yafet, "Ruderman-Kittel-Kasuya-Yosida range function of a one-dimensional free-electron gas", Physical Review B **36**, 3948 (1987).

[134] Z. Zhang, L. Zhou, P. Wigen, and K. Ounadjela, "Using ferromagnetic resonance as a sensitive method to study temperature dependence of interlayer exchange coupling", Physical review letters **73**, 336 (1994).

[135] M. Vohl, J. Barnaś, and P. Grünberg, "Effect of interlayer exchange coupling on spin-wave spectra in magnetic double layers: Theory and experiment", Physical Review B **39**, 12003 (1989).

[136] P. Grünberg, "Magnetostatic spin-wave modes of a heterogeneous ferromagnetic double layer", Journal of Applied Physics **52**, 6824–6829 (1981).

[137] R. Camley, "Nonreciprocal surface waves", Surface Science Reports **7**, 103–187 (1987).

[138] M. S. Kang, A. Butsch, and P. S. J. Russell, "Reconfigurable light-driven opto-acoustic isolators in photonic crystal fibre", Nature Photonics **5**, 549–553 (2011).

[139] Z. Wang and S. Fan, "Optical circulators in two-dimensional magneto-optical photonic crystals", Optics letters **30**, 1989–1991 (2005).

[140] Z. Zhang, L. Zhou, P. Wigen, and K. Ounadjela, "Angular dependence of ferromagnetic resonance in exchange-coupled Co/Ru/Co trilayer structures", Physical Review B **50**, 6094 (1994).

[141] P. Wigen, Z. Zhang, L. Zhou, M. Ye, and J. Cowen, "The dispersion relation in antiparallel coupled ferromagnetic films", Journal of applied physics **73**, 6338–6340 (1993).

[142] V. Denysenkov and A. M. Grishin, "Broadband ferromagnetic resonance spectrometer", Review of scientific instruments **74**, 3400–3405 (2003).

[143] B. Khodadadi, J. B. Mohammadi, J. M. Jones, A. Srivastava, C. Mewes, T. Mewes, and C. Kaiser, "Interlayer exchange coupling in asymmetric Co-Fe/Ru/Co- Fe trilayers investigated with broadband temperature-dependent ferromagnetic resonance", Physical Review Applied **8**, 014024 (2017).

[144] J. Hamrle, J. Pištora, B. Hillebrands, B. Lenk, and M. Münzenberg, "Analytical expression of the magneto-optical Kerr effect and Brillouin light scattering intensity arising from dynamic magnetization", Journal of Physics D: Applied Physics **43**, 325004 (2010).

[145] Z. Li, R. Skomski, S.-H. Liou, S. Michalski, M. Chipara, and R. D. Kirby, "Magnetization precession and domain-wall structure in cobalt-ruthenium-cobalt trilayers", Journal of Applied Physics **109**, 07C113 (2011).

[146] G. Wu, S. Chen, Y. Ren, Q. Jin, and Z. Zhang, "Laser-Induced Magnetization Dynamics in Interlayer-Coupled [Ni/Co] 4/Ru/[Co/Ni] 3 Perpendicular Magnetic Films for Information Storage", ACS Applied Nano Materials **2**, 5140–5148 (2019).

[147] A. Kamimaki, S. Iihama, T. Taniguchi, and S. Mizukami, "All-optical detection and evaluation of magnetic damping in synthetic antiferromagnet", Applied Physics Letters **115**, 132402 (2019).

[148] J. Han, P. Zhang, J. T. Hou, S. A. Siddiqui, and L. Liu, "Mutual control of coherent spin waves and magnetic domain walls in a magnonic device", Science **366**, 1121–1125 (2019).

[149] S. Saha, J. Zhou, K. Hofhuis, A. Kákay, V. Scagnoli, L. J. Heyderman, and S. Gliga, "Spin-wave dynamics and symmetry breaking in an artificial spin ice", Nano Letters **21**, 2382–2389 (2021).

[150] R. Wang et al., "Artificial 'spin ice'in a geometrically frustrated lattice of nanoscale ferromagnetic islands", Nature **439**, 303–306 (2006).

[151] C. Castelnovo, R. Moessner, and S. L. Sondhi, "Magnetic monopoles in spin ice", Nature **451**, 42–45 (2008).

[152] S. Gliga, E. Iacocca, and O. G. Heinonen, "Dynamics of reconfigurable artificial spin ice: Toward magnonic functional materials", APL Materials **8**, 040911 (2020).

[153] S. Lendinez and M. Jungfleisch, "Magnetization dynamics in artificial spin ice", Journal of Physics: Condensed Matter **32**, 013001 (2019).

[154] L. J. Heyderman and R. L. Stamps, "Artificial ferroic systems: novel functionality from structure, interactions and dynamics", Journal of Physics: Condensed Matter **25**, 363201 (2013).

[155] S. H. Skjærvø, C. H. Marrows, R. L. Stamps, and L. J. Heyderman, "Advances in artificial spin ice", Nature Reviews Physics **2**, 13–28 (2020).

[156] H. Arava, P. M. Derlet, J. Vijayakumar, J. Cui, N. S. Bingham, A. Kleibert, and L. J. Heyderman, "Computational logic with square rings of nanomagnets", Nanotechnology **29**, 265205 (2018).

[157] S. Gliga, A. Kákay, R. Hertel, and O. G. Heinonen, "Spectral analysis of topological defects in an artificial spin-ice lattice", Physical review letters **110**, 117205 (2013).

[158] M. Jungfleisch et al., "Dynamic response of an artificial square spin ice", Physical Review B **93**, 100401 (2016).

[159] X. Zhou, G.-L. Chua, N. Singh, and A. O. Adeyeye, "Large area artificial spin ice and anti-spin ice Ni80Fe20 structures: Static and dynamic behavior", Advanced Functional Materials **26**, 1437–1444 (2016).

[160] M. T. Kaffash, W. Bang, S. Lendinez, A. Hoffmann, J. B. Ketterson, and M. B. Jungfleisch, "Control of spin dynamics in artificial honeycomb spin-ice-based nanodisks", Physical Review B **101**, 174424 (2020).

[161] S. Lendinez, M. T. Kaffash, and M. B. Jungfleisch, "Emergent spin dynamics enabled by lattice interactions in a bicomponent artificial spin ice", Nano Letters **21**, 1921–1927 (2021).

[162] T. Dion et al., "Tunable magnetization dynamics in artificial spin ice via shape anisotropy modification", Physical Review B **100**, 054433 (2019).

[163] Y. Li et al., "Brillouin light scattering study of magnetic-element normal modes in a square artificial spin ice geometry", Journal of Physics D: Applied Physics **50**, 015003 (2016).

[164] S. Mamica, X. Zhou, A. Adeyeye, M. Krawczyk, and G. Gubbiotti, "Spin-wave dynamics in artificial anti-spin-ice systems: Experimental and theoretical investigations", Physical Review B **98**, 054405 (2018).

[165] E. Iacocca, S. Gliga, R. L. Stamps, and O. Heinonen, "Reconfigurable wave band structure of an artificial square ice", Physical Review B **93**, 134420 (2016).

[166] A. Farhan et al., "Direct observation of thermal relaxation in artificial spin ice", Physical review letters **111**, 057204 (2013).

[167] C. Nisoli, R. Wang, J. Li, W. F. McConville, P. E. Lammert, P. Schiffer, and V. H. Crespi, "Ground state lost but degeneracy found: The effective thermodynamics of artificial spin ice", Physical review letters **98**, 217203 (2007).

[168] J. P. Morgan, A. Stein, S. Langridge, and C. H. Marrows, "Thermal ground-state ordering and elementary excitations in artificial magnetic square ice", Nature Physics **7**, 75–79 (2011).

[169] N. Arora and P. Das, "Spin wave spectral probing of degenerate microstates in building-block of square artificial spin ice", AIP Advances **11**, 035030 (2021).

[170] D. M. Arroo, J. C. Gartside, and W. R. Branford, "Sculpting the spin-wave response of artificial spin ice via microstate selection", Physical Review B **100**, 214425 (2019).

[171] V. Bhat, F. Heimbach, I. Stasinopoulos, and D. Grundler, "Magnetization dynamics of topological defects and the spin solid in a kagome artificial spin ice", Physical Review B **93**, 140401 (2016).

[172] J. C. Gartside, A. Vanstone, T. Dion, K. D. Stenning, D. M. Arroo, H. Kurebayashi, and W. R. Branford, "Reconfigurable magnonic mode-hybridisation and spectral control in a bicomponent artificial spin ice", Nature Communications **12**, 1–9 (2021).

[173] E. Iacocca, S. Gliga, and O. G. Heinonen, "Tailoring spin-wave channels in a reconfigurable artificial spin ice", Physical Review Applied **13**, 044047 (2020).

[174] R. Macêdo, G. Macauley, F. Nascimento, and R. Stamps, "Apparent ferromagnetism in the pinwheel artificial spin ice", Physical Review B **98**, 014437 (2018).

[175] S. Gliga et al., "Emergent dynamic chirality in a thermally driven artificial spin ratchet", Nature materials **16**, 1106–1111 (2017).

[176] Y. Li et al., "Superferromagnetism and domain-wall topologies in artificial "pinwheel" spin ice", ACS nano **13**, 2213–2222 (2018).

[177] M. Wyss et al., "Stray-field imaging of a chiral artificial spin ice during magnetization reversal", ACS nano **13**, 13910–13916 (2019).

[178] A. Vansteenkiste, J. Leliaert, M. Dvornik, M. Helsen, F. Garcia-Sanchez, and B. Van Waeyenberge, "The design and verification of MuMax3", AIP advances **4**, 107133 (2014).

[179] A. Kakay, E. Westphal, and R. Hertel, "Speedup of FEM micromagnetic simulations with graphical processing units", IEEE transactions on magnetics **46**, 2303–2306 (2010).

[180] D. Shechtman, I. Blech, D. Gratias, and J. W. Cahn, "Metallic Phase with Long-Range Orientational Order and No Translational Symmetry", Phys. Rev. Lett. **53**, 1951–1953 (1984).

[181] L. Berthier and G. Biroli, "Theoretical perspective on the glass transition and amorphous materials", Rev. Mod. Phys. **83**, 587–645 (2011).

[182] X. Shen, L. Li, W. Cui, and Y. Feng, "Improvement of fractal model for porosity and permeability in porous materials", International Journal of Heat and Mass Transfer **121**, 1307–1315 (2018).

[183] Q. Zeng, M. Luo, X. Pang, L. Li, and K. Li, "Surface fractal dimension: an indicator to characterize the microstructure of cement-based porous materials", Applied Surface Science **282**, 302–307 (2013).

[184] M. W. Takeda, S. Kirihara, Y. Miyamoto, K. Sakoda, and K. Honda, "Localization of Electromagnetic Waves in Three-Dimensional Fractal Cavities", Phys. Rev. Lett. **92**, 093902 (2004).

[185] C. Puente-Baliarda, J. Romeu, R. Pous, and A. Cardama, "On the behavior of the Sierpinski multiband fractal antenna", IEEE Transactions on Antennas and Propagation **46**, 517–524 (1998).

[186] S. N. Kempkes, M. R. Slot, S. E. Freeney, S. J. Zevenhuizen, D. Vanmaekelbergh, I. Swart, and C. M. Smith, "Design and characterization of electrons in a fractal geometry", Nature physics **15**, 127–131 (2019).

[187] S. Sederberg and A. Elezzabi, "Sierpiński fractal plasmonic antenna: a fractal abstraction of the plasmonic bowtie antenna", Opt. Express **19**, 10456–10461 (2011).

[188] D. R. Hofstadter, "Energy levels and wave functions of Bloch electrons in rational and irrational magnetic fields", Phys. Rev. B **14**, 2239–2249 (1976).

[189] M. Soljacic, M. Segev, and C. R. Menyuk, "Self-similarity and fractals in soliton-supporting systems", Phys. Rev. E **61**, R1048–R1051 (2000).

[190] S. Sears, M. Soljacic, M. Segev, D. Krylov, and K. Bergman, "Cantor Set Fractals from Solitons", Phys. Rev. Lett. **84**, 1902–1905 (2000).

[191] M. Segev, M. Soljačić, and J. M. Dudley, "Fractal optics and beyond", Nature Photonics **6**, 209–210 (2012).

[192] M. Wu, B. A. Kalinikos, L. D. Carr, and C. E. Patton, "Observation of Spin-Wave Soliton Fractals in Magnetic Film Active Feedback Rings", Phys. Rev. Lett. **96**, 187202 (2006).

[193] T. Sebastian et al., "Low-damping spin-wave propagation in a microstructured Co2Mn0. 6Fe0. 4Si Heusler waveguide", Applied Physics Letters **100**, 112402 (2012).

[194] A. Conca, J. Greser, T. Sebastian, S. Klingler, B. Obry, B. Leven, and B. Hillebrands, “Low spin-wave damping in amorphous Co40Fe40B20 thin films”, Journal of Applied Physics **113**, 213909 (2013).

[195] Z. Wang, V. Zhang, H. Lim, S. Ng, M. Kuok, S. Jain, and A. Adeyeye, “Observation of frequency band gaps in a one-dimensional nanostructured magnonic crystal”, Applied Physics Letters **94**, 083112 (2009).

[196] Z. K. Wang, V. L. Zhang, H. S. Lim, S. C. Ng, M. H. Kuok, S. Jain, and A. O. Adeyeye, “Nanostructured magnonic crystals with size-tunable bandgaps”, ACS nano **4**, 643–648 (2010).

[197] S. Tacchi et al., “Band diagram of spin waves in a two-dimensional magnonic crystal”, Physical review letters **107**, 127204 (2011).

[198] M. Krawczyk and D. Grundler, “Review and prospects of magnonic crystals and devices with reprogrammable band structure”, Journal of Physics: Condensed Matter **26**, 123202 (2014).

[199] F. Lisiecki et al., “Magnons in a quasicrystal: Propagation, extinction, and localization of spin waves in fibonacci structures”, Physical Review Applied **11**, 054061 (2019).

[200] F. Lisiecki et al., “Reprogrammability and Scalability of Magnonic Fibonacci Quasicrystals”, Phys. Rev. Applied **11**, 054003 (2019).

[201] V. S. Bhat and D. Grundler, “Angle-dependent magnetization dynamics with mirror-symmetric excitations in artificial quasicrystalline nanomagnet lattices”, Phys. Rev. B **98**, 174408 (2018).

[202] S. Watanabe, V. S. Bhat, K. Baumgaertl, and D. Grundler, “Direct Observation of Worm-Like Nanochannels and Emergent Magnon Motifs in Artificial Ferromagnetic Quasicrystals”, Advanced Functional Materials **30**, 2001388 (2020).

[203] C. McMullen, “The Hausdorff dimension of general Sierpiński carpets”, Nagoya Mathematical Journal **96**, 1–9 (1984).

[204] U. Nowak and K.-D. Usadel, “Diluted antiferromagnets in a magnetic field: A fractal-domain state with spin-glass behavior”, Physical Review B **44**, 7426 (1991).

[205] P. Monceau and J.-C. S. Lévy, “Spin waves in deterministic fractals”, Physics Letters A **374**, 1872–1879 (2010).

[206] C. Swoboda, M. Martens, and G. Meier, “Control of spin-wave excitations in deterministic fractals”, Physical Review B **91**, 064416 (2015).

[207] M. T. Barlow, “Analysis on the Sierpinski carpet”, Analysis and geometry of metric measure spaces **56**, 27–53 (2013).

[208] Z. Zhou and M. Wu, "The Hausdorff measure of a Sierpinski carpet", Science in China Series A: Mathematics **42**, 673–680 (1999).

[209] K. J. Falconer and B. Lammering, "Fractal properties of generalized Sierpiński triangles", Fractals **6**, 31–41 (1998).

[210] F. Garcia-Sanchez, P. Borys, A. Vansteenkiste, J.-V. Kim, and R. L. Stamps, "Nonreciprocal spin-wave channeling along textures driven by the Dzyaloshinskii-Moriya interaction", Physical Review B **89**, 224408 (2014).

[211] M. Belmeguenai et al., "Interface Dzyaloshinskii-Moriya interaction in the interlayer antiferromagnetic-exchange coupled Pt/CoFeB/Ru/CoFeB systems", Physical Review B **96**, 144402 (2017).

[212] C.-G. Duan, J. P. Velev, R. F. Sabirianov, W.-N. Mei, S. S. Jaswal, and E. Y. Tsymbal, "Tailoring magnetic anisotropy at the ferromagnetic/ferroelectric interface", Applied Physics Letters **92**, 122905 (2008).

[213] F. Ma, H. Lim, Z. Wang, S. Piramanayagam, S. Ng, and M. Kuok, "Micromagnetic study of spin wave propagation in bicomponent magnonic crystal waveguides", Applied Physics Letters **98**, 153107 (2011).

[214] S. Tacchi et al., "Forbidden band gaps in the spin-wave spectrum of a two-dimensional bicomponent magnonic crystal", Physical review letters **109**, 137202 (2012).

[215] G. Gubbiotti, S. Tacchi, M. Madami, G. Carlotti, S. Jain, A. Adeyeye, and M. Kostylev, "Collective spin waves in a bicomponent two-dimensional magnonic crystal", Applied Physics Letters **100**, 162407 (2012).

Curriculum Vitae

Name	Jingyuan Zhou
Birth	February 24, 1993
Nationality	Chinese
Languages	Chinese and English

Education

2017-2021	PhD studies, ETH Zürich and Paul Scherrer Institute
2015-2017	Master of Science ETH in Physik, ETH Zürich
2011-2015	Bachelor of Science, Applied Physics, Beijing Institute of Technology
2013	Exchange Student, The Hong Kong University of Science and Technology

Publications

Published in peer-reviewed journals

- Spin-Wave Dynamics and Symmetry Breaking in an Artificial Spin Ice
  Susmita Saha, **Jingyuan Zhou**, Kevin Hofhuis, Attila Kákay, Valerio Scagnoli, Laura J. Heyderman, and Sebastian Gliga
  Nano Letters **21**, 2382-2389 (2021).
- Ultrafast laser induced precessional dynamics in antiferromagnetically coupled ferromagnetic thin films
  Jingyuan Zhou, Susmita Saha, Zhaochu Luo, Eugenie Kirk, Valerio Scagnoli and Laura J. Heyderman
  Physical Review B **101**, 214434 (2020).
- Control of damping in perpendicularly magnetized thin films using spin-orbit torques
  Susmita Saha, Peter Flauger, Claas Abert, Aleš Hrabec, Zhaochu Luo, **Jingyuan Zhou**, Valerio Scagnoli, Dieter Suess, and Laura J. Heyderman
  Physical Review B **101**, 224401 (2020).

In preparation

- Precessional dynamics in ferromagnetic fractal-like structures
  Jingyuan Zhou, Susmita Saha, Mateusz Zelent, Zhaochu Luo, Valerio Scagnoli, Maciej Krawczyk, and Laura J. Heyderman

Conference contributions

- Magnetism and Magnetic Materials Conference (MMM) 2020
  Oral presentation: Ultrafast laser induced precessional dynamics in antiferromagnetically coupled ferromagnetic films
- Joint European Magnetic Symposia (JEMS) 2019
  Poster presentation: Magnetization dynamics in antiferromagnetically coupled ferromagnetic trilayers
- Swiss Physical Society (SPS) Annual Meeting 2018
  Poster Presentation: Spin-wave nonreciprocity in bi-component magnonic crystals

Teaching experience

Teaching assistant

FS 2019, 2018 “Introduction to Materials Science”